Hollow Carbon Nanospheres: A Structural Integrity Investigation

by
Jessica du Toit

Thesis presented in partial fulfilment of the requirements for the degree of Master of Engineering (Mechanical) in the Faculty of Engineering at Stellenbosch University

UNIVERSITEIT
iYUNIVESITHI
STELLENBOSCH
UNIVERSITY

Supervisor: Prof Deborah Blaine
Co-supervisor: Prof Neil Coville

March 2018

Declaration

By submitting this thesis electronically, I declare that the entirety of the work contained therein is my own, original work, that I am the sole author thereof (save to the extent explicitly otherwise stated), that reproduction and publication thereof by Stellenbosch University will not infringe any third-party rights and that I have not previously in its entirety or in part submitted it for obtaining any qualification.

March 2018

Abstract

Hollow carbon nanospheres (HCNSs) have high strength, thermal and electrical conductivities which allow for applications in electrochemical capacitors, lithium ion battery anodes and catalyst supports. When used as a catalyst support, a HCNS encapsulates a nanoparticle, preventing sintering and increasing the catalyst lifespan. The structural integrity of the HCNS is of importance since failure of the HCNS shell will result in the sphere no longer fulfilling its purpose.

The aim of this investigation was to evaluate the structural integrity and to link synthesis conditions to the structural integrity of HCNSs.

HCNSs were synthesised using two different coating methods: chemical vapour deposition (CVD) and resorcinol formaldehyde (RF) treatment. The synthesis variables significantly affected the spherical shell. At best, the CVD synthesis method produced only partial spheres. Unlike the CVD method, the RF method successfully produced HCNSs with whole, unbroken shells.

A bulk powder compaction testing method was developed for the nanospheres where the Heckel yield pressure, a qualitative powder parameter, was extracted from fitting the Heckel equation to the experimental data. The Heckel yield pressures for the silica nanospheres showed a clear decrease with increasing sphere diameter. An inverse relationship between Young's modulus and nanosphere diameter is reported in literature for both polystyrene nanospheres and amorphous HCNSs. Additionally, a proportional correlation between Young's modulus and Heckel yield pressure is reported in literature. This relationship extended to include a similar relationship between nanosphere diameter and failure stress. Therefore, the size dependency of Heckel yield pressure for the silica nanospheres studied here is supported.

In this investigation, the Heckel yield pressure was used as a qualitative parameter to determine the structural integrity of the nanospheres.

Uittreksel

Koolstof holnanosfere (HCNS) besit eienskappe van hoë strukturele sterkte, hitte- en elektriese geleidingsvermoë, wat maak dat hulle geskik is vir toepassing in elektrochemiese kapasitors, litium ioon sel-anodes en ondersteuning vir katalisators. Indien dit gebruik word as ondersteuning vir ’n katalisator, word die nanopartikel deur die HCNS inkapsel; daardeur word die sinterproses verhoed en die katalisator-lewensduur bevorder. Die strukturele betroubaarheid van die HCNS is belangrik aangesien dat die faling van die HCNS-dop die gevolgtrek sal hê dat die sfeer nie meer aan sy doel sal voldoen nie.

Die uitkoms van hierdie navorsing is om 'n beter begrip van die HCNS strukturele eienskappe te vorm en om die sinteseparameters aan die HCNS strukturele betroubaarheid te koppel.

HCNS’e word deur twee verskillende bedekkingsmetodes gesintetiseer: chemiese-dampneerslag (CVD) en resorsinol formaldehied (RF) metodes. Die sintesisveranderlikes het ’n waarnemende effek op die sferiesedop. Op sy beste, word slegs gedeeltelikesfere met die CVD proses vervaardig. In teenstelling met die CVD proses, het die RF metpde heel HCNS’e gelewer wat nie stukkend is nie.

'n Massa poeiersamedrukkingtoetsmetode is vir die HCNS ontwikkel, waar die Heckel-swigdruk, ‘n kwalitatiewe poeierparameter, bepaal word deur die data by die Heckel-vergelyking te pas. Die Heckel-swigdruk vir die silika-nanosfere toon 'n duidelike afname met toenemende sfeerdiameter. ’n Omgekeerde verwantskap tussen Young se modulus en nanosfeerdiameter word vie beide polistreen nanosfere en amorfiese HCNS’e in die literatuur gevind. Verder, word daar ’n proposioneleverwantskap tussen Young se modulus en Heckel-swigdruk in die literatuur gevind. Hierdie verwantskap word uitgebrei om ’n soortgelyke verwantskap tussen nanosfeerdiameter en falingsspanning in te sluit. Daarom word die afhanklikheid van Heckel-swigdruk op grootte vir die silikananosfere wat hier bestudeer word, ondersteun. In hierdie ondersoek, word die Heckel-swigdruk as ’n kwalitatiewe parameter gebruik om die strukturele betroubaarheid van die nanosfere te bepaal.

Die massa poeiersamedrukkingtoets, gevolg deur die Heckel-swigdruk berekening, verskaf ‘n goeie kwalitatiewe parameter wat gebruik kan word om die verskillende nanosfeer monsters te vergelyk. Die Heckel-swigdruk resultate toon 'n duidelike afname met laer sfeerdop strukturele betroubaarheid.

Acknowledgements

I would like to acknowledge the following people and organisations:

- My supervisor for her constant guidance and support.
- My co-supervisor for his assistance in synthesis training and access to equipment and materials at the University of the Witwatersrand.
- The Stellenbosch University Central Analytical Facility for the use of the FE-SEM and elemental analysis, as well as training and assistance.
- The Department of Process Engineering at Stellenbosch University for the use of TGA equipment.
- The Centre of Materials Engineering, at the University of Cape Town for the use of TGA equipment.
- The Department of Chemical Sciences at the University of the Western Cape for the use of the HF laboratory.
- The Microscopy and Microanalysis Unit at the University of the Witwatersrand for the use of TEM equipment.
- The Electron Microscopy Unit at the University of the Western Cape for the TEM use
- Kansai Plascon, Department of Polymer Sciences at Stellenbosch University for the use of a Zetasizer.
- The support of the DST-NRF Centre of Excellence in Strong Materials (CoE-SM) towards this research. Opinions expressed, and conclusions arrived at, are those of the author and are not necessarily to be attributed to the CoE-SM.

Table of Contents

List of Figures

List of Tables

List of Abbreviations

Abbreviation	Description
AFM	Atomic force microscopy
CAF	Central analytical facility
CoE-SM	Centre of excellence of strong materials
CTAB	Cetyl trimethylammonium bromide
CVD	Chemical vapour deposition
D	Deformation compaction stage
DLS	Dynamic light scattering
DST	Department of science and technology
DTG	Differential temperature gradient
EDS	Energy dispersive spectroscopy
FEA	Finite element analysis
HCNS	Hollow carbon nanosphere
HCNSs	Hollow carbon nanospheres
NRF	National Research Foundation
PI	Polydispersity index
PSD	Particle size distribution
R&D	Rearrangement and deformation compaction stage
RF	Resorcinol formaldehyde
S&R	Static forces and rearrangement compaction stage
SEM	Scanning electron microscopy
TEM	Transmission electron microscopy
TEOS	Tetraethyl orthosilicate
TGA	Thermogravimetric analysis

Nomenclature

Symbol	Description	Unit
A_c	Punch cross-sectional area	m^2
D	Diameter	m
E	Young's modulus	Pa
E^*	Effective Young's modulus	Pa
F	Force	N
K	Heckel parameter	Pa^{-1}
m	Linear fitting parameter	-
N	Number of test repetitions	-
P	Pressure	Pa
P_c	Compaction pressure	Pa
P_y	Heckel yield pressure	Pa
v	Powder compact volume	m^3
X	Linear fitting parameter	-
Y	Linear fitting parameter	-
ϵ	Residual (fractional) porosity	-
ϵ_0	Initial residual porosity	-
$\epsilon_{0_{Heckel}}$	Initial Heckel porosity	-
ϵ_{Heckel}	Residual Heckel porosity	-
$\Delta\overline{\rho_c}$	Average fractional density deviation	-
$\overline{\rho_c}$	Average fractional density	-
ρ_c	Fractional (apparent) density of the powder	-
$\rho_{theoretical}$	Density of theoretical solid material	kg/m^3
σ_0	Heckel yield stress	Pa

1. Introduction

1.1. Background and Motivation

General interest in carbon nanostructures has increased, in various industries, due to their high surface area, lightweight strong structure and chemical inertness. Graphitic hollow carbon nanospheres (HCNSs) have high strength, thermal and electrical conductivities which allow for applications in electrochemical capacitors (Yuan, *et al*., 2008), lithium ion battery anodes (Huang, *et al*., 2016) and catalyst supports (Nongwe, *et al*., 2014).

HCNSs have both an internal and shell structure that can be manipulated during synthesis, allowing for the wide range of applications. The structural integrity of the HCNSs is of importance since failure of the HCNS shell will result in the sphere no longer fulfilling its application.

Various methods exist to test the material properties and mechanical behaviour of individual nanospheres. However, these methods rely on expensive equipment to separate and analyse a single nanosphere. An alternative method would be to test the nanospheres in their bulk powder form and extract qualitative information about their properties and structural integrity.

1.2. Objectives and Scope

The aim of this investigation was to develop a better understanding of the structural integrity of HCNSs. Various synthesis factors were investigated, and the samples were characterised and tested in their bulk powder form. The aim was achieved through meeting two objectives.

1.2.1. Objective 1: To Synthesise HCNSs under Different Conditions and Characterise the Products

Existing methods were reviewed, HCNSs were synthesised, and relationships were concluded between the synthesis factors and structural characteristics.

1.2.2. Objective 2: To Develop a Bulk Powder Testing Method Capable of Evaluating the Structural Integrity of Nanospheres.

Existing individual testing methods of HCNSs were reviewed, as well as bulk powder compression testing methods for solid particle powders. A bulk powder compaction testing method was developed for the nanospheres where qualitative parameters regarding the powder's structural integrity were extracted. These qualitative relationships were then used to compare the structural integrity of HCNSs synthesised under different conditions.

1.2.3. Scope

The scope of this investigation was limited to two HCNS synthesis methods and a finite number of synthesis factor variables.

HCNSs were synthesised via the chemical vapour deposition (CVD) method with various synthesis factors at the Mechanical Engineering Department of Stellenbosch University. The HCNSs synthesised via the resorcinol formaldehyde (RF) method were produces and provided by the CoE-SM at the Department of Chemistry at the University of the Witwatersrand.

Solid silica nanospheres, used as templates for the synthesis of HCNSs, as well as HCNSs synthesised by both the CVD and RF methods were evaluated. The structural integrity testing of the nanospheres was limited to microscopy characterisation, thermogravimetric analysis and qualitative parameter determination from the bulk powder compaction testing. Individual nanosphere testing to determine the material properties and mechanical behaviour of the nanospheres was recommended for future research.

In this thesis, the prefix *nano-* refers to all particles with diameters less than 1 µm. This convention is typical in the field of nanosphere research (Zhang et al., 2014).

2. Literature Review: Hollow Carbon Nanospheres

This section presents a critical literature review on the synthesis and characterisation methods of HCNSs used for this investigation.

2.1. Carbon Allotropes

The structure and properties of carbon materials depend on the bonds between the carbon atoms. Carbon atoms can form bonds with other carbon atoms with sp, sp^2 and sp^3 hybridisation, as illustrated in Figure 2.1.

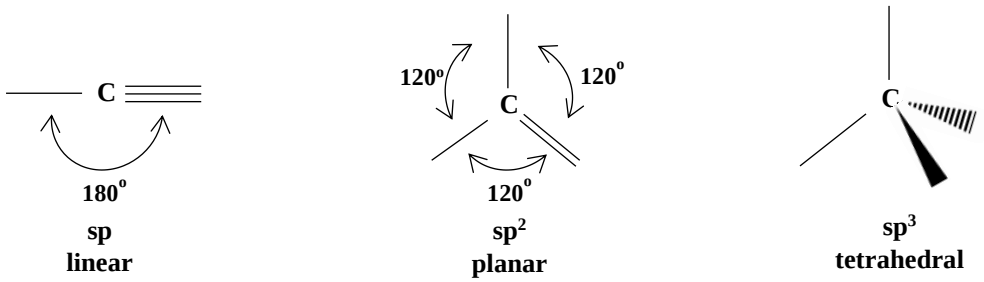

Figure 2.1: Carbon hybridisation states

Allotropes of carbon include graphene, carbon nanotubes, fullerenes, diamond and graphite. The crystal structures of these allotropes are presented in Figure 2.2.

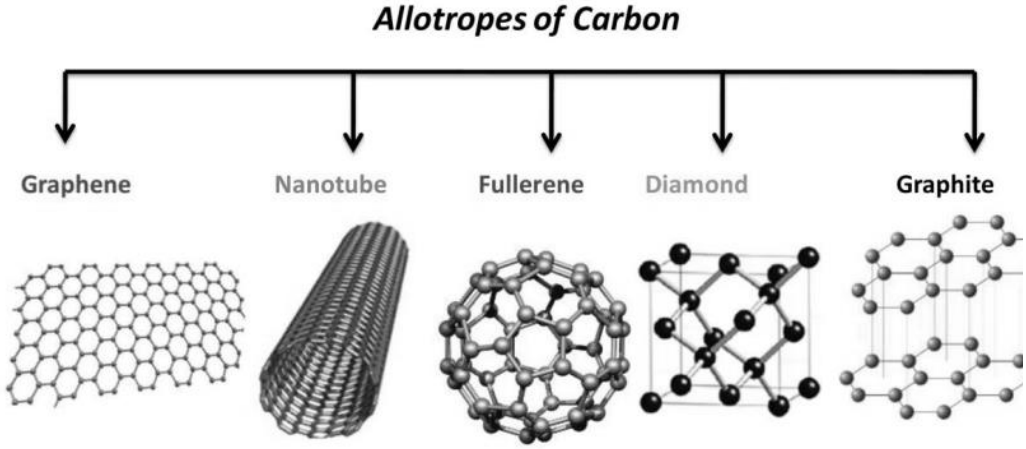

Figure 2.2: Carbon allotrope crystal structures taken from (Tiwari, *et al*., 2016)

Graphene consists of a plane of sp^2 hybridised carbon atoms that form hexagonal rings. Nanotubes and fullerenes consist of shaped planes of graphene. Diamond consists of sp^3 hybridised carbon atoms that form an infinite tetrahedral crystal structure. Graphite consists of sheets of graphene bonded together with Van der Waals forces. Amorphous carbon consists of a combination of sp^2 and sp^3 hybridised carbon with no specific crystal structure or grain boundaries (Yang, et al., 2016).

This investigation focused on hollow carbon nanospheres (HCNSs) consisting of graphitic carbon; layered graphene flakes with defects in the crystal structure. Figure 2.3 presents SEM images of HCNSs.

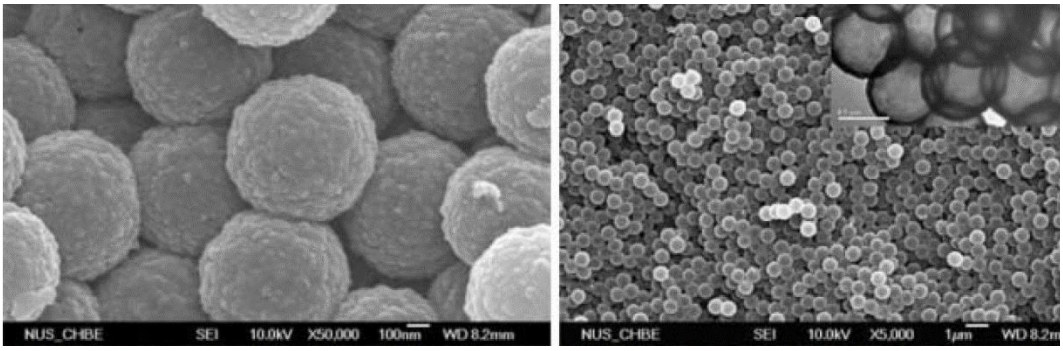

Figure 2.3: SEM and TEM (top right corner) images of HCNSs taken from (Su, *et al*., 2006)

The in-plane strength, thermal and electrical conductivity of graphite is higher than these parameters perpendicular to the graphite plane. However, due to the random orientations of graphitic carbon flakes that layer to make the hollow sphere structure, HCNSs have comparatively higher strength, thermal and electrical conductivities combined with relative chemical inertness. This allows for applications in electrochemical capacitors (Yuan, *et al*., 2008) and the encapsulation of lithium nanoparticles in lithium ion battery anodes to increase battery lifespan (Huang, *et al*., 2016).

In catalysis, HCNSs are used as catalyst supports as well as protective shells. At nanoparticle size, catalyst particles tend to sinter together during use, reducing the surface area and reusability of the catalyst. The permeable HCNS shell acts as a physical barrier preventing sintering while increasing the reusability of the supported catalyst (Nongwe, *et al*., 2014).

2.2. Synthesis

2.2.1. Overview

Synthesising HCNSs usually involves a soft or hard template which acts as the sacrificial core for the sphere. Hard-templating procedures involve the synthesis of a rigid core template. A carbon shell of graphitic flakes is formed on the hard template surface and then the template is removed afterwards. Soft-templating procedures involve the direct generation of the hollow sphere through chemical reactions. The template in this case is usually an organic compound or surfactant (Li, *et al*., 2016). Other synthesis methods of HCNSs include spray pyrolysis (Xu, *et al*., 2012) and other soft-templating techniques (Li, *et al*., 2016).

The HCNSs used in this investigation were synthesised using two hard templating methods. A hard silica template was chosen as the sacrificial core and the carbon shell coating was obtained through chemical vapour deposition (CVD) and a resorcinol formaldehyde (RF) method.

These methods have been used by the Carbon Nanotubes and Strong Composites research group within the DST/NRF Centre of Excellence of Strong Materials (Deshmukh, *et al*., 2010; Phaahlamohlaka, *et al*., 2017; Dlamini, 2016 and Phaahlamohlaka, *et al*., 2016).

2.2.2. Template Synthesis: Stöber Process

In this investigation, solid silica nanospheres were used as the hard templates. These silica nanospheres were synthesised via a Stöber process (Green, *et al.*, 2003).

Tetraethyl orthosilicate (TEOS) undergoes hydrolysis in an ethanol solution with ammonium hydroxide as the catalyst. When the solution is supersaturated, colloidal silica nanoparticles nucleate and condense out of the solution to form a xerogel. The hydrolysis reaction, in an ethanol suspension with a pH of 11 - 12, is presented by

$$Si(OC_2\,H_5)_4(aq) + 4\,H_2O(l) \rightarrow Si(OH)_4(aq) + 44C_2H_5OH(l)\,. \quad (1)$$

The condensation reaction, in an ethanol suspension with a pH of 11 - 12, is presented by

$$Si(OH)_4(aq) \rightarrow SiO_2(s) + 2\,H_2O\,(l)\,. \quad (2)$$

The liquid part of the silica xerogel is removed after centrifugation and the solid part washed with ethanol before being dried in an oven to form a silica nanosphere powder. The size of the silica nanospheres is dependent on the ammonium hydroxide and TEOS concentrations, as well as other factors such as temperature and stirring rate of the suspension (Ibrahim, *et al*., 2010).

2.2.3. Chemical Vapour Deposition (CVD)

CVD can be used to coat hard silica templates with a shell of bonded graphitic carbon flakes. During the process, silica nanospheres are placed in a quartz boat in a quartz tube in a tube furnace. Argon is bubbled through a liquid carbon precursor to carry the carbon precursor vapour into the heated furnace in an inert atmosphere. The furnace temperature is held constant for a pre-set residence time. At temperatures $\geq 600\ ^0$C the carbon precursor decomposes and deposits flakes of graphitic carbon on the templates (Li, *et al*., 2016). After the residence time has elapsed, the furnace is cooled. Figure 2.3 and Figure 2.4 shows a schematic diagram of a CVD furnace and the carbon shell growth mechanism, respectively.

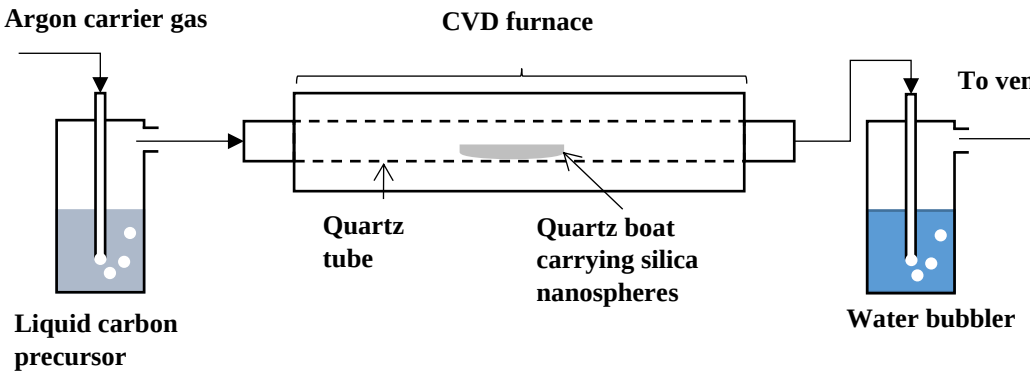

Figure 2.4: Chemical vapour deposition furnace schematic

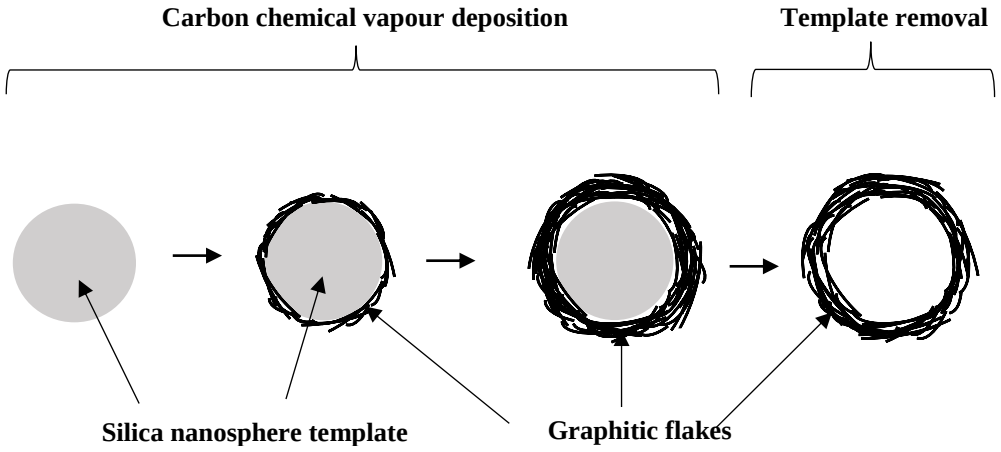

Figure 2.5: Cross section through HCNSs showing the CVD deposition growth mechanism

Various carbon precursors can be used in CVD such as toluene, benzene, acetylene and hexane (Deshmukh, *et al.*, 2010).

Results from literature showed that increased residence time increased the coating thickness which resulted in hollow spheres with a thicker shell (Su, *et al.*, 2006) (Li, *et al.*, 2016). However, the thickness of the carbon coating depended on the amount of carbon precursor that decomposes around the template. The flow rate of the argon gas which carriers the carbon precursor vapour also affects the coating; the flow rate must be fast enough to carry enough carbon precursor into the furnace but slow enough so that the carbon precursor spends sufficient time at the decomposition temperature inside the furnace. CVD furnace dimensions and specifications such as hot zone length as well as the quartz tube shape also affect the final product.

The CVD method allows for a customisable synthesis. The template determines the internal diameter as well as internal surface porosity of the HCNSs. Encapsulated particles can be integrated into the template or applied as a coating before the

carbon coat (Nongwe, *et al.*, 2014). The carbon coated silica spheres can also be coated with silica and then coated in carbon again to make double shelled HCNSs (Liu, *et al.*, 2015).

The CVD method does have disadvantages. Since the carbon coating mechanism is via deposition, an uneven coat is a possible outcome. This could result in weak spots in the carbon shell causing the hollow spheres to break during the template removal process. Parameters that determine the outcome of the carbon coating include the carbon precursor gas flow rate, furnace residence time and synthesis temperature (Su, *et al.*, 2006).

2.2.4. Resorcinol Formaldehyde (RF) Method

The RF synthesis method can be used to coat silica templates in carbon through three main steps:

- First, the silica nanospheres are dispersed and stirred in a solution of ammonia, ethanol, resorcinol formaldehyde, TEOS and cetyl trimethylammonium bromide (CTAB). This process coats the silica in a RF polymer.
- The RF coated silica spheres are then heat treated in an autoclave. Afterwards, the coated silica spheres are then separated via centrifugation, washed with acetone and dried.
- Secondly, the coated spheres are then placed in a furnace at 900 ^{o}C for a set residence time under inert conditions. The heat carbonises the polymer, turning it into a graphitised carbon coating on the silica templates.

The silica templates are then removed to yield hollow carbon nanospheres. This method has been used to synthesise hollow carbon nanospheres for various applications (Phaahlamohlaka, *et al*., 2016; Fuertes, *et al*., 2012; Zhang, *et al*., 2014 and Dlamini, 2016).

The RF method involves the polymerisation of the RF monomer in the presence of ammonia as a catalyst. The negative hydroxide functional groups on the RF polymer are attracted to the positive ammonium ions on the surface of the silica nanospheres, coating the sphere in the polymer (Liu, *et al*., 2011). A schematic of the RF coating mechanism is presented in Figure 2.6.

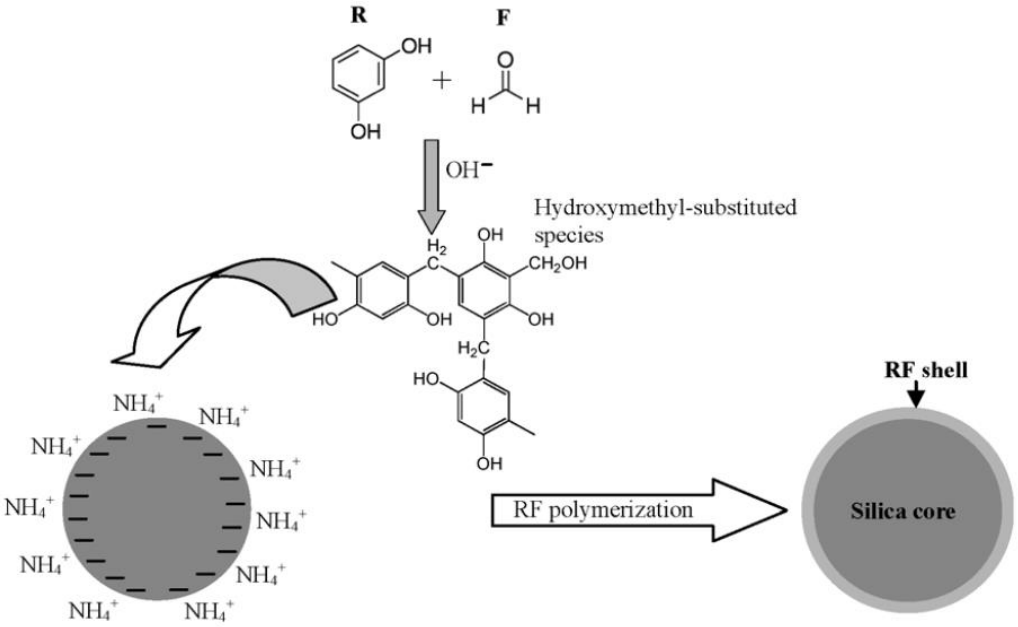

Figure 2.6: RF polymer coating mechanism taken from (Liu, *et al*., 2011)

Like the CVD method, the RF method also proves to be customisable with regards to the hard template, shell thickness and encapsulated particles. Advantages of this method over CVD include a more uniform coating of the silica nanosphere template. This occurs because the silica nanospheres are suspended in solution when coated with the RF polymer, unlike the dried silica nanosphere powder in CVD which lies in a quartz boat. In the ammonium solution, the positive ammonium ions on the surface of the silica nanospheres prevent the spheres from agglomerating, thus increasing the available surface area for RF coating (Liu, *et al*., 2011).

2.2.5. Silica Template Removal

After the sacrificial template has been coated with carbon, it can be removed. The carbon coated silica templates are treated with aqueous hydrofluoric acid until all the solid silica reacts to form aqueous hexafluorosilicic acid. The chemical reaction is presented by

$$SiO_2(s) + 6HF(aq) \rightarrow H_2SiF_6(aq) + 2H_2O(l)\ . \qquad (3)$$

The HCNSs are removed from the acid solution by centrifugation, followed by drying to evaporate the remaining liquid.

2.2.6. Nitrogen-Doping

HCNSs can be used as catalyst supports in aqueous environments. However, the HCNSs are sometimes hydrophobic and will not be miscible in these reagents without additional surface modification.

Nitrogen-doping of carbon nanomaterials has been successfully conducted (Xiong, *et al.*, 2014) (Nongwe, *et al.*, 2013). HCNSs are placed in a quartz tube heated to 800 ^{o}C while acetonitrile vapour is passed over the sample in an inert atmosphere. Once doped, the carbon structures have increased hydrophilicity. Doping carbon nanotubes with nitrogen has also been seen to increase the electrical conductivity (Xiong, *et al*., 2014).

However, little is known about how nitrogen-doping affects the structural integrity of the HCNSs.

2.3. Characterisation

Once synthesised, the HCNSs must be characterised to determine their properties and structure. Explanations for the following analytical techniques were adapted from (Kaufmann, 2003).

2.3.1. Scanning Electron Microscopy

Scanning electron microscopy (SEM) provides information about the surface structure, while energy dispersive spectroscopy (EDS) is used to analyse the chemical composition of a specimen. A SEM unit is typically used to perform EDS as both techniques use a focused electron beam.

The focused beam of primary electrons scans the surface in a raster pattern where the electrons interact with the specimen in the interaction volume. Secondary electrons are emitted from the surface due to this interaction. The emitted electrons are detected and converted into electrical output signals to create the grayscale image.

EDS detects higher energy electrons that are emitted from deeper in the interaction volume. Elements with higher atomic mass scatter more electrons, therefore these electrons can be used to detect areas of varying chemical composition.

SEM images can provide surface information of the nanospheres. This method can be used to determine particle diameters, particle shapes and surface imperfections. It is important that the specimen is electrically conductive so that a charge of electrons does not build up on the specimen which will appear as bright areas on the image.

If the specimen is not conductive, it must be coated with a conductive material such as carbon or gold. It is important that the coating is thick enough so that the specimen is conductive but not too thick that the coating becomes blotchy and can interfere with the image. Carbon sputter coating is usually used for compositional analysis where gold is used for high magnification SEM images (CAF Stellenbosch Univeristy, 2017).

2.3.2. Transmission Electron Microscopy

Transmission electron microscopy (TEM) provides information about the entire volume of the specimen. Like SEM, a focused electron beam is used. However, the beam does not scan the specimen but rather a wide static beam of electrons passes

through the entirety of the specimen. The electrons interact with the volume, are focused again and then detected to form a digital greyscale image.

TEM provides information about the internal structure of the specimen which is critical for hollow nanostructures. This characterisation technique can be used to determine the HCNS diameter, shell thickness and the presence of encapsulated particles.

2.3.3. Thermogravimetric Analysis

Thermogravimetric analysis (TGA) is a method where a specimen is heated with a known heating program while the mass of the specimen is measured over time. Mass change of the specimen will be recorded and the mass change versus temperature as well as the differential temperature gradient (DTG) can be calculated and analysed. This method can be used to characterise a sample of HCNSs before and after silica removal.

Silica and non-combustible impurities will not burn away in oxygen, whereas carbon will. The presence of silica in a sample will show as a residual mass after the TGA is complete. Different allotropes of carbon will also burn at different temperatures; amorphous carbon oxidises at lower temperatures than graphitic carbon. Therefore, TGA can be used to determine the degree of graphitisation of the carbon sample.

Figure 2.7 shows the mass loss versus temperature superimposed on the differential mass loss curve of the TGA results on a sample of graphitic hollow carbon nanospheres from (Mutuma, *et al.*, 2017)

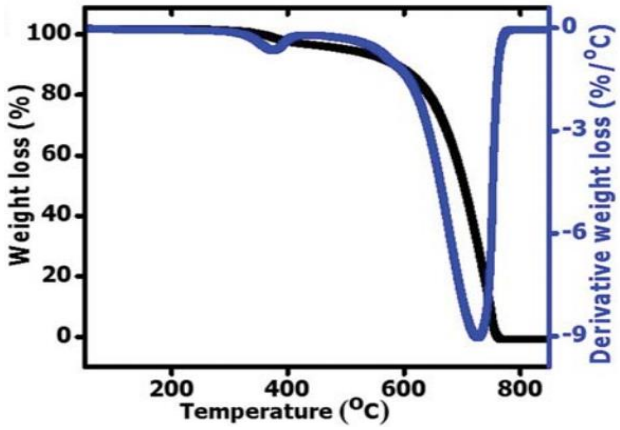

Figure 2.7: TGA results of a sample of HCNSs from (Mutuma, *et al*., 2017). The black curve is the mass loss vs temperature and the blue curve is the differential temperature gradient.

The differential temperature gradient in Figure 2.7 gives an indication of the composition of different carbon allotropes in the sample. The first dip or trough in the curve, at approximately 380 °C, corresponds to the oxidation of the amorphous carbon or surface functional groups. The second trough, at approximately 720 °C, corresponds to the graphitic carbon. A qualitative comparison of these two troughs shows the intensity of defects or amorphous carbon present in the graphitic HCNSs.

The mass loss vs temperature curve ended at 0 mass %, this indicated that the entire sample was oxidised and therefore no silica was present in the HCNS sample.

2.3.4. Zetasizing

A Zetasizer instrument uses dynamic light scattering (DLS) to characterise the particle size distribution (PSD) of nanoparticles suspended in a clear liquid.

The movement of nanoparticles in a suspension is not dominated by gravitational forces, but rather by the inter-particle Van der Waals forces. As such, nanoparticles in a suspension tend to remain suspended and move due to Brownian motion rather than experiencing gravitational settling. Smaller particles move or diffuse faster than larger particles in the suspension. This speed is measured by focussing a laser on the suspension sample and detecting the fluctuations with time (Malvern, 2011). The accuracy of the PSD measured by the Zetasizer depends on the sample preparation. It is important that the particles are suspended as a homogenous suspension. Sonication and surfactant addition can be used to ensure that there are no suspended agglomerates.

DLS has been found to yield different results when compared to TEM and SEM analysis of the same nanoparticles (Khlebtsov & Khlebtsov, 2011). Often these techniques are used in combination in order to fully understand the characteristics of the PSD.

3. Literature Review: Structural Integrity Evaluation

This section presents a critical literature review on existing methods relating to testing the structural integrity of nanospheres and powders.

3.1. Motivation for Structural Integrity Testing

HCNSs have been used and tested in various applications such as catalyst supports (Nongwe, *et al.*, 2014), electrochemical capacitors (Yuan, *et al.*, 2008) and encapsulation of lithium nanoparticles in lithium battery anodes (Huang, *et al.*, 2016). In these applications, the shell structure of the HCNSs needs to stay intact in order for the spheres to carry out their function.

As a catalyst support, HCNSs act as physical barriers preventing sintering of the encapsulated catalyst nanoparticles. Millions of these HCNSs can be used in a reactor to carry out certain reactions where the fluid reagents will flow over and through the supported catalysts.

The pressure of reagents flowing though the HCNSs can compress the spheres together, stressing the carbon shells. If this compressive stress exceeds the failure stress of the HCNS then the shell will break, no longer preventing the catalyst nanoparticles from sintering together. Since catalytic activity is proportional to catalyst surface area, sintering is very detrimental and reduces the reusability of the catalyst (Nongwe, *et al.*, 2014).

Therefore, it is important to know the structural integrity of the HCNSs as function of their synthesis parameters and properties.

3.2. Current Nanosphere Structural Integrity Testing Methods

Current methods that have been used to test the structural integrity and properties of nanospheres include in-situ TEM nanoindentation (Yang, et al., 2016) and atomic force microscopy (AFM) compression (Guo, *et al.*, 2014). These methods isolate one sphere, perform a compressive test and calculate the material properties from the force-vs-deformation behaviour.

3.2.1. TEM Nanoindentation

Nanoindentation has been used to determine the mechanical properties of amorphous HCNSs synthesised via spray pyrolysis in an in-situ TEM compression experiment (Yang, et al., 2016).

Single HCNSs were isolated using TEM and then compressed in-situ while the force-vs-displacement data was recorded. The spheres display a significant degree of elastic deformation as the shell bends and buckles until final failure.

The study also tested HCNSs with varying diameter and shell thicknesses. Results indicated that the spheres with smaller diameters and thicker shells failed at higher forces, as presented in Figure 3.1.

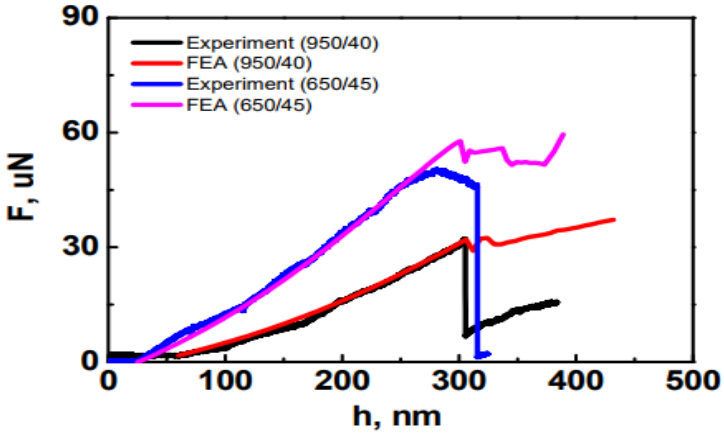

Figure 3.1: Experimental and FEA results of compressing single HCNSs with varying diameter and shell thickness (diameter [nm]/shell thickness[nm]) taken from supplementary data of (Yang, *et al*., 2016). F denotes the uniaxial compressive force and h denotes the sphere deformation.

Since two parameters, diameter and shell thickness, were varied, it was difficult to isolate the effect of one parameter.

A finite element analysis (FEA) was performed as a comparison to the experimental results. The intrinsic Young's modulus of the bulk amorphous carbon was determined in an additional experiment with Hertz contact theory and calculated to be 20.2 GPa. The FEA results matched the experimental results well, as seen in Figure 3.1.

The effective Young's modulus, E^*, for a porous or hollow sphere was extracted from the force-deformation behaviour of an individual sphere using classic Hertz contact theory. Full details of the calculations are found in the supplementary information of (Yang, et al., 2016). It should be noted that the effective Young's modulus for a hollow or porous sphere is dependent on the sphere diameter and sphere density. The sphere density takes the total sphere volume including internal porosity, into account. Furthermore, sphere density is related to the ratio of shell:sphere volume, which is approximated as a function of the t:D ratio as well. As such, the effective Young's modulus is not a pure material property, but decreases with increasing sphere diameter.

Figure 3.2 presents results for mesoporous carbon nanospheres that confirms this the relationship between E^* and D.

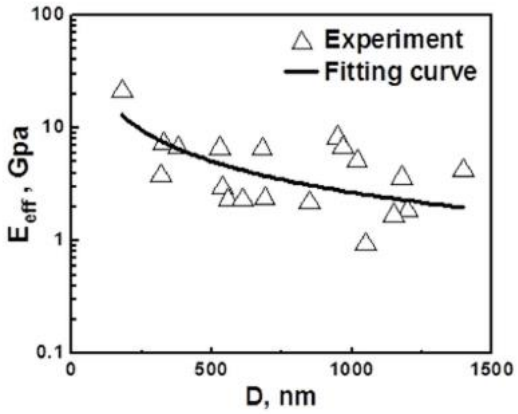

Figure 3.2: Effective Young's modulus (where $E_{eff} = E^*$) for porous spheres of varying diameter, D, taken from (Yang, *et al.*, 2016)

Other conclusions were that the failure strength and failure strain also decreased with increasing sphere diameter, and that the hollow spheres experienced significant elastic deformationbefore failure (Yang, et al., 2016).

3.2.2. Atomic Force Microscopy Compression

Atomic force microscopy (AFM) compression has been used to determine the elastic properties of individual solid polystyrene nanospheres (Guo, *et al.*, 2014). Nanospheres with varying diameter were identified and isolated with the AFM, and the force-vs-displacement behaviour was analysed during compression by the AFM tip.

The contact between the AFM tip and the nanosphere was modelled using the Hertz elastic contact theory. The effective Young's modulus results, as determined using AFM compression on polystyrene nanospheres with various diameters, are presented in Figure 3.3. The Johnson-Kendall-Roberts (JKR) model was also fitted to the data in order to predict the effective Young's modulus. This model considers the adhesion force within the contact region usually used for systems with high adhesion and low stiffness; the derived theory is presented in (Guo, *et al.*, 2014).

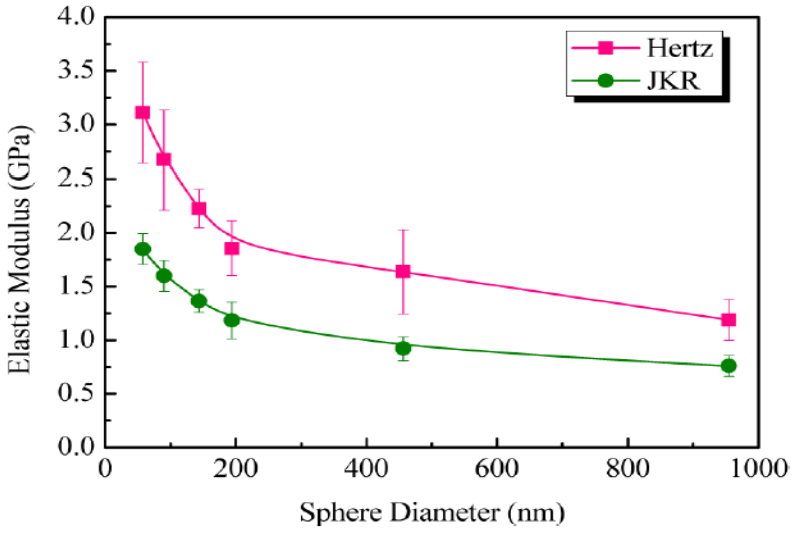

Figure 3.3: Effective Young's modulus (where elastic modulus = effective Young's modulus) results from individual polystyrene nanospheres, taken from (Guo, *et al.*, 2014)

The results from Figure 3.3 showed that the effective Young's modulus increases with decreasing sphere diameter, this is consistent with the TEM nanoindentation results from (Yang, et al., 2016).

3.2.3. Isolated/Individual vs Bulk Nanosphere Testing

The TEM nanoindentation method calculated the effective Young's modulus, yield stress and fracture stress of individual hollow amorphous carbon nanospheres. Video footage of the compression combined with the FEA results also gave an indication of the deformation and failure mechanisms. AFM compression results allowed the calculation of the effective Young's modulus of individual solid polystyrene nanospheres. The advantage of these methods is that they provide quantitative information about the structural integrity and properties of nanospheres.

The main disadvantage of these methods includes the necessity to isolate an individual sphere. Additionally, both methods rely on the availability of expensive equipment. An alternative method would be to test the nanospheres in their bulk form and extract qualitative information about their properties and structural integrity. No literature on bulk powder testing of HCNSs was found, however, there is significant literature on bulk powder compression testing for solid particle powders. This forms the topic of the subsequent section.

3.3. Powder Compaction

Powder compaction is a powder metallurgy technique used to manufacture components by shaping and densifying a powder (German, 2005). Die and punch tools achieve this compaction by applying a uniaxial pressure to the powder. Figure 3.4 presents a schematic of the powder compaction stages in a die compaction setup for metal powders.

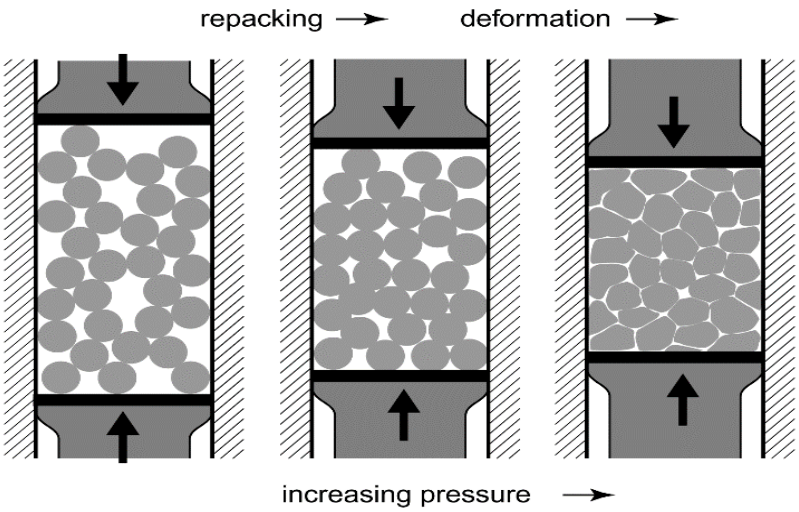

Figure 3.4: Powder compaction stages of a metal powder in a punch and die setup. Taken from (German, 2005)

The first stage in Figure 3.4 shows the rearranging and repacking of the particles. The second stage shows further rearrangement of the particles combined with breaking agglomerates and some particle deformation. The last stage shows only deformation of the particles after a theoretical full packing density had been reached.

Three main compaction stages were then defined:

- **S&R compaction stage:** The static forces and rearrangement stage, corresponding to the first stage in Figure 3.4. This stage is the initial low force linear region of the force-vs-displacement compaction behaviour.
- **R&D compaction stage:** The rearrangement and deformation stage, corresponding to the second stage in Figure 3.4. The force increases exponentially with displacement in this stage.
- **D stage:** The deformation stage, corresponding to the third stage in Figure 3.4. In this stage, the powder starts behaving like the bulk solid and the force-displacement behaviour is linear.

These three powder compaction stages are related to the force-vs-displacement behaviour of the powder being compacted, presented in Figure 3.5.

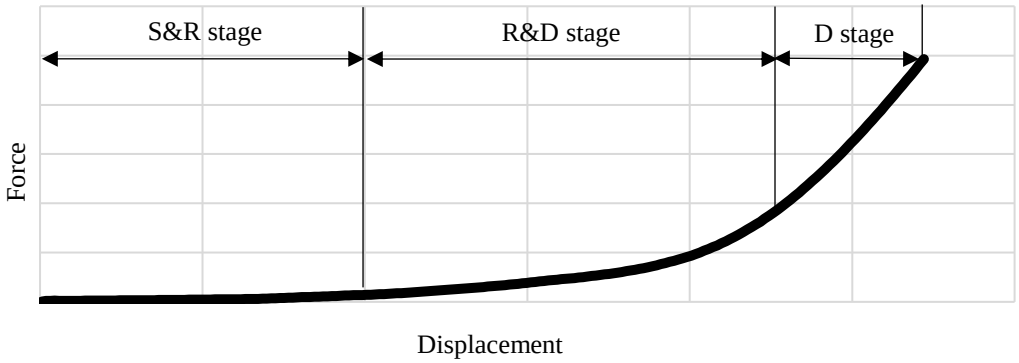

Figure 3.5: Force-vs-displacement behaviour of powder compaction relating to the three main compaction stages.

Powder compaction can also be used to determine the powder compressibility, the relationship between compaction pressure and compact density during powder compaction. During powder compaction, the fractional density of the compact is measured as a function of the applied pressure. This data can be fitted to powder compaction equations, from which powder property parameters can be extracted (Denny, 2002; German, 2005).

3.3.1. Powder Compaction Mechanisms and Modelling

Powder compaction can be modelled with equations that relate the fractional density of the compact to the applied compaction pressure. Reasons for fitting experimental data to compaction equations include:

- Linearising compaction plots for easy comparisons between sets of data.
- Qualitative comparisons of the fitting equation parameters between different powders.
- Predicting the pressure needed for a required compact density.

Different types of powders tend to be modelled with different equations depending on the powder's characteristics. The Heckel and Kawakita equations are most commonly used because they can extract physical properties of the powder being compacted (Denny, 2002).

Different powders compact with different mechanisms and have different relationships between compaction pressure and fractional density. The main compaction mechanisms, as summarised from (Denny, 2002) are:

- Initial stage compaction: This includes the sliding and rearrangement of primary particles as well as the collapsing and breaking of weak agglomerates.
- Fragmentation compaction: Primary particles fragment as a result of brittle fracture. The broken fragments can occupy the smaller spaces between the primary particles increasing the fractional density.
- Plastic flow of deformation compaction: The primary particles deform to fill the areas between particles and increase fractional density.

- Elastic compaction: This is the last mechanism at high compaction pressures when the compact is nearly non-porous and behaves like the bulk material.

A single compaction equation cannot accurately fit all these different mechanisms and stages of die compaction. Therefore, it is important to know the dominant mechanism of powder compaction at each stage to accurately fit a compaction equation.

It was also reported that the following factors affect the accuracy of the compaction equation fitting and parameter determination (Denny, 2002):

- In the case of punch and die compaction, the filling of the die should be consistent and repeatable as settling and rearrangement of the powder can result in significant fractional density changes.
- Internal lubricants should be avoided as this influences the powder density.
- The powder should be characterised in terms of the particle size distribution and presence of agglomerates.
- Die wall frictional effects should be minimised by reducing the compact aspect (height to diameter) ratio.
- The elastic deformation of the punch and die setup could influence the compaction data at high compaction pressures.

To obtain comparisons of the nanosphere structural properties, either the Heckel or Kawakita equations could be used to extract powder properties of the material. It was proved that the two equations are identical at low compaction pressures and it was concluded that the Kawakita equation is only valid for a small range of materials and can be defined as a special case of a modified Heckel equation (Denny, 2002). For this investigation, the more general Heckel equation was chosen for analysis.

3.3.2. Heckel Equation

The Heckel equation was initially developed with metal powders that compact through plastic deformation. It has, however, been used for brittle powders such as pharmaceuticals and oxides (Denny, 2002). The Heckel equation was adapted from (Denny, 2002) and presented in its differential form by

$$-\frac{d\epsilon}{dP} = K\epsilon \,, \tag{4}$$

where ϵ denotes fractional porosity, P the compaction pressure and K is a powder constant, related to the Heckel yield stress, σ_0 , defined by,

$$K = \frac{1}{3\sigma_0} \,. \tag{5}$$

The Heckel yield pressure, P_y , is a powder property that can be calculated directly from K by

$$P_y = \frac{1}{K} \,. \tag{6}$$

Assuming that ϵ_o is the initial porosity of the loose powder at applied compaction pressure P = 0, after integration of Equation 4 from P = 0 to P and ϵ_o to $\epsilon_{@P}$ yields

$$\ln\frac{1}{\epsilon} = \ln\left(\frac{1}{\epsilon_0}\right) + KP \; . \tag{7}$$

Thus Equation 7 gives the residual porosity, ϵ, of a compacted powder at compaction pressures P. Equation 7 can be fit to the experimental data as a straight line, presented by

$$\underbrace{\ln\frac{1}{\epsilon}}_{Y} = \underbrace{\ln\left(\frac{1}{\epsilon_0}\right)}_{C} + \underbrace{KP}_{mX} \; . \tag{8}$$

The non-linear form of the Heckel equation is presented by

$$\epsilon_{\text{Heckel}} = \epsilon_{0_{\text{Heckel}}} e^{KP_c} \; . \tag{9}$$

Finally, the fractional density of a powder can be calculated from the residual porosity as presented by

$$\rho = 1 - \epsilon \; . \tag{10}$$

It was claimed by the authors in (Denny, 2002) that there had been no published data showing the correlation between the Heckel yield pressures and the published yield stress properties of non-metallic materials. However, proportional correlations were found between the measured Young's modulus and Heckel yield pressures for some metal and polymer powders (Roberts & Rowe, 1987). The deformation response of a nanosphere in compression has been shown to be related to the effective Young's modulus through Hertz contact theory (Yang et al., 2016; Guo et al., 2014). Additionally, the inverse relationship between effective Young's modulus and nanosphere diameter has been presented in Section 3.2.1 and 3.2.2 for both hollow and solid nanospheres. This was extended to include a similar relationship to failure stress. Therefore, the Heckel yield pressure is used in this study as a qualitative parameter to compare different powders' elastic response and structural integrity.

4. Methodology

This section presents the experimental setups and procedures followed to achieve the investigation's objectives: to synthesise HCNSs under different conditions and to characterise the products, and to develop a bulk powder testing method capable of evaluating the structural integrity of nanospheres.

4.1. Hollow Carbon Nanosphere Synthesis

In this investigation HCNSs were synthesised using two different methods. The overview of the synthesis methodology is presented in Figure 4.1.

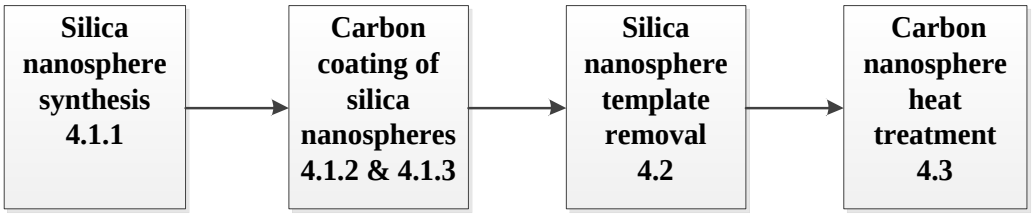

Figure 4.1: HCNS synthesis overview

4.1.1. Silica Nanosphere Template Synthesis

Silica nanospheres were used as the sacrificial templates for the HCNSs. Three sizes of silica spheres were synthesised via the Stöber process with diameters of 200 nm, 300 nm and 400 nm.

The silica nanospheres were synthesised by mixing ethanol, water and ammonia solution in a laboratory beaker on a magnetic stirrer. TEOS was added after 20 minutes to start the nanosphere nucleation process and then the solution was stirred for a further 2 hours. The silica colloid solution was then centrifuged at 5000 rpm for 20 minutes. The liquid part was discarded and the solid washed with ethanol three times. The solid silica powder pellets were then dried for 12 hours in a furnace at 100 ^{o}C. Once dried, the powder was gently ground with a pestle and mortar and stored in labelled glass sample vials.

The relative concentrations and volumes of reagents determine the silica nanosphere diameters. However, the procedure followed for synthesising specific nanosphere diameters was not exact. Silica nanosphere synthesis parameters of specific diameters were estimated based on previous experimental results completed within the Chemistry Department at the University of the Witwatersrand (Mutuma, 2016).

The three samples were denoted S200, S300 and S400 representing their approximate diameters in nanometres. Zetasizing and SEM characterisation was performed to calculate the exact diameter and particle size distribution.

The experimental apparatus, chemical volumes and step-by-step procedures used for the silica synthesis are presented in Appendix A.1.

4.1.2. Chemical Vapour Deposition Method

The carbon shells of the HCNSs used for this investigation were synthesised via two methods, the first being CVD.

For the CVD process, toluene was used as the carbon precursor liquid and argon as the carrier gas. A stationary CVD furnace with a constant diameter quartz tube was used for the deposition with the silica template placed in a quartz boat at the centre of the hot zone. The CVD furnace apparatus is presented in Figure 4.2.

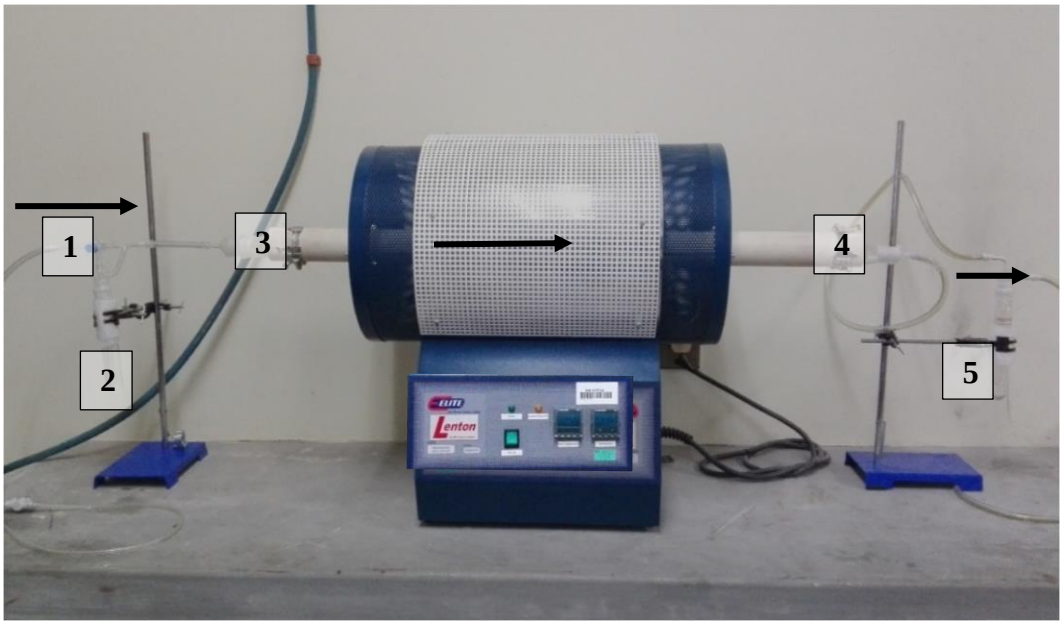

[1] Direction of argon gas inlet
[2] Toluene bubbler with tap to either flow through or bypass toluene
[3] Quartz tube inlet
[4] Quartz tube outlet
[5] Water bubbler to exit vent

Figure 4.2: CVD furnace setup photo.

The furnace was set to ramp up at a rate of 10 ^{o}C/min until 900 ^{0}C was reached. The toluene/argon bubbler tap was turned so that the argon bubbled through the toluene and the residence temperature was held for 4 hours. The argon was then set to bypass the toluene before the furnace was turned off and cooled. The apparatus, chemicals and step-by step procedures are presented in Appendix A.2.

For CVD HCNS synthesis, many factors influence the coating of the silica templates. Initial results of CVD synthesis showed broken HCNSs from SEM characterisation. It was then decided that a few synthesis factors would be manipulated to try obtain whole HCNSs. For this investigation, only a few of these factors were varied to see the effect on structural integrity. These factors are summarised in Table 4.1.

Table 4.1: CVD synthesis factors

Synthesis factor	Varied? Yes/No	Value(s) tested
Argon flow rate	Yes	100, 150 & 200 mL/min
Toluene temperature	Yes	25 ºC & 70 ºC
Mass of silica template	Yes	0.2, 0.5 & 1g
Carbon precursor type	No	Toluene
Residence time	No	4 hours
Reactor temperature	No	900 ºC

4.1.3. Resorcinol Formaldehyde (RF) Method

The second method of HCNS synthesis investigated was the RF method presented in (Dlamini, 2016). The synthesis of the RF HCNSs was completed at the University of Witwatersrand and provided by the CoE-SM. The apparatus and experimental overview can be found in (Dlamini, 2016).

Colloidal silica nanospheres were synthesised in a laboratory beaker by adding TEOS to an ethanol, water and ammonia solution. The mixture was stirred for 1 hour to allow the formation of silica nanospheres. Resorcinol and formaldehyde was then added to the solution and stirred for 24 hours to make the core-shell structures. The RF coated spheres were then hydrothermally treated in an autoclave at 100ºC for 24 hours followed by centrifugation and drying. The dry RF coated silica nanospheres were then carbonised in a tube furnace for 1 hour under a nitrogen atmosphere.

Two samples of RF HCNSs were synthesised by varying the volume of ammonia solution in an attempt to vary the resulting average sphere diameter between the two samples. The step-by-step procedure and reagent volumes are presented in Appendix A.3.

4.2. Silica Removal

Once the silica templates had been coated in graphitised carbon, the templates were removed with hydrofluoric acid. The HF treatment was performed at the Department of Chemistry at Witwatersrand and the Chemical Sciences laboratories at the University of the Western Cape.

10 wt% HF acid was added to a sample of HCNS powder and the solution was stirred for 12 hours. The solution was then diluted with water and centrifuged at 500 rpm for 30 minutes. The clear liquid was discarded and the solid HCNSs were dried at 100 ºC for 12 hours. The apparatus, chemicals and step-by-step procedures are presented in Appendix A.4.

4.3. Heat Treatment of Carbon Spheres

The HCNSs were heat treated under inert conditions to remove any reagents and functional groups on the surface of the spheres from the synthesis or silica removal stages.

The procedure was the same as the CVD HCNS procedure except that HCNSs were placed into the quartz boat instead of silica, the furnace was heated to 800 ^{o}C not 900 ^{o}C and the argon bypassed the toluene for the whole experiment. The step-by-step procedure is presented in Appendix A.5.

4.4. Solid CVD Carbon Sphere Synthesis

Solid carbon spheres were also synthesised for this investigation to serve as structural integrity comparisons to the broken CVD HCNSs. The solid spheres were synthesised using the same CVD HCNS synthesis method except no quartz boat or silica nanosphere templates were used. The solid carbon spheres that resulted had a large particle size distribution and non-uniform shape.

The apparatus, chemicals and step-by-step procedures are presented in Appendix A.2.

4.5. Nitrogen-Doping

In this investigation, the RF HCNSs were doped with nitrogen to determine the effect this treatment had on the sphere's structural integrity.

The apparatus for this treatment is the same as the CVD HCNS apparatus except acetonitrile at 78 ^{o}C was used instead of toluene. The procedure was the same as the CVD HCNS procedure except that RF HCNSs were placed into the quartz boat instead of silica, the furnace temperature of 750 ^{o}C was held for 2 hours instead of 4. The apparatus, chemicals and step-by-step procedures are presented in Appendix A.6.

4.6. Characterisation

All the nanosphere samples were characterised to determine their size, shape and composition. The characterisation procedures are summarised and presented in Table 4.2.

Table 4.2: Nanosphere characterisation summary

Sample	Stage(s)	Methods used
Silica nanospheres	• After drying • After powder compaction	• Zetasizing • SEM
Hollow carbon nanospheres	• After carbon coating • After silica removal and heat treatment • After nitrogen-doping • After powder compaction	• SEM & TEM • TGA
Solid carbon spheres	• After synthesis • After powder compaction	• SEM & TEM • TGA

The sample preparation and analysis of the characterisation techniques is presented in the subsequent sections.

4.6.1. Zetasizing

Zetasizing was used to determine the PSD, mean and standard deviation of the three silica nanosphere samples. A Malvern nano Zetasizer was used in the Kansai Plascon laboratories at the department of Polymer Sciences, Stellenbosch University.

The Zetasizer returned the following results after each run;

- Intensity PSD,
- Number PSD,
- Volume PSD,
- Z-average and
- Polydispersity Index (PI).

The PI served as a quality control parameter. The PI indicates the width of the PSD from 0 (very narrow) – 1 (very wide). An acceptable limit is application dependent. 0.35 was chosen after multiple Zeta sizing runs were performed where most of the consistent results fell under this index. If the test returned a PI > 0.35 then the result was discarded, and the test was repeated.

The number PSD was chosen to characterise the silica nanospheres. This was chosen over the Z-average and other PSDs because the likelihood of agglomerates being present in the sample was high, and the number PSD was the least sensitive to larger particles in the suspension. More information about the Zetasizer is presented in Appendix B.1.

In order to minimise the agglomerates in the suspension, three sample preparation variables were investigated:

- Heating the silica to 250 ^{o}C in air for 1 hour to remove any residual reagents on the surface of the silica spheres.

- Addition of a phosphate fatty acid ether alkane surfactant to the suspension before sonication.
- Sonicating for 20 minutes instead of 10 minutes.

The control sample was not heat treated, did not contain any surfactants and was sonicated for 10 minutes.

4.6.2. Scanning Electron Microscopy (SEM)

SEM images were used to confirm the PSD and surface structure of the silica, and carbon nanospheres. EDS was used in conjunction with the SEM images to determine the elemental composition of the samples. This was used to determine the composition of any impurities, the presence of silica after HF treatment and confirmation of surface doping. A Merlin FE-SEM at the Central Analytical Facility (CAF) of Stellenbosch University was used for the nanosphere characterisation.

To prepare the nanosphere sample for SEM characterisation, conductive carbon tape was placed on a clean aluminium SEM stub. A small piece of aluminium foil was then placed on the tape so that approximately half the exposed carbon tape is covered. A very small amount of nanosphere powder was dropped onto the tape and foil with a spatula. Excess powder was removed with compressed air. If the nanosphere powder contained silica, then the stubs were sputter coated with gold. If the nanosphere powder was pure carbon, coating was not necessary.

With regards to sputter coating it is important that the sample is electrically conductive so that a charge of electrons does not build up on the powder particles, thereby causing bright areas on the image. Figure 4.3 presents SEM images of silica spheres with and without charge build up, illustrating the necessity of sputter coating nonconductive silica particles in gold.

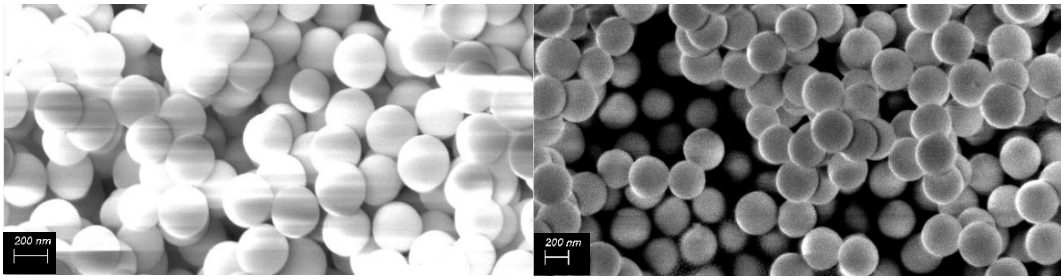

Figure 4.3: SEM images of silica with a charge build-up (left) and without a charge build-up (right)

However, it was important not to overcoat the sample, as presented in Figure 4.4 where the sputter coat interfered with the quality of the image.

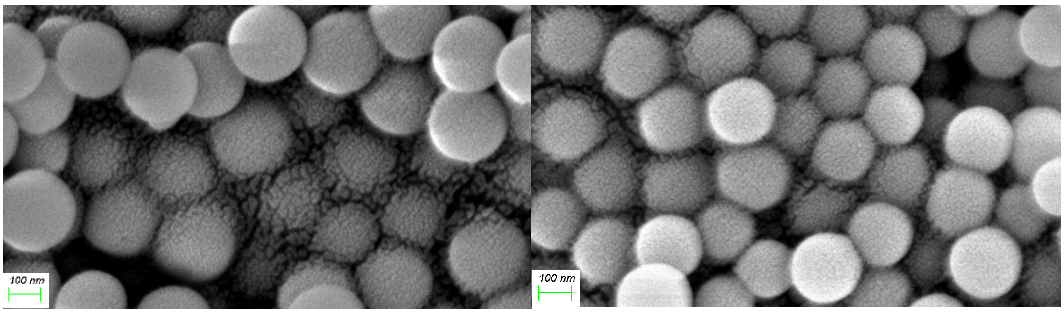

Figure 4.4: Over-coating of silica nanospheres

4.6.3. Transmission Electron Microscopy (TEM)

TEM images were used to determine the internal structure and shell thickness of the HCNSs. FEI Tecnai TEM instruments were used at the Microscopy and Microanalysis Unit at University of the Witwatersrand and at the Electron Microscopy Unit at the University of the Western Cape.

To prepare the samples for TEM characterisation, 1 mg of nanospheres and 5 mL of ethanol were added to a glass sample vial and sonicated for 10 minutes. A single drop of the homogenous suspension was then dropped onto a TEM copper grid on filter paper and allowed to dry completely before characterisation.

TEM was also used in conjunction with SEM characterisation to avoid misinterpretation of the external structure of the nanospheres. Since TEM creates an image based on the entire volume of the specimen, holes and cracks in the surface of the samples could be hidden or misinterpreted in the images. Figure 4.5 presents a SEM and TEM image comparison of the same HCNS sample where the SEM image clearly shows the sphere defects while the TEM image could be misinterpreted.

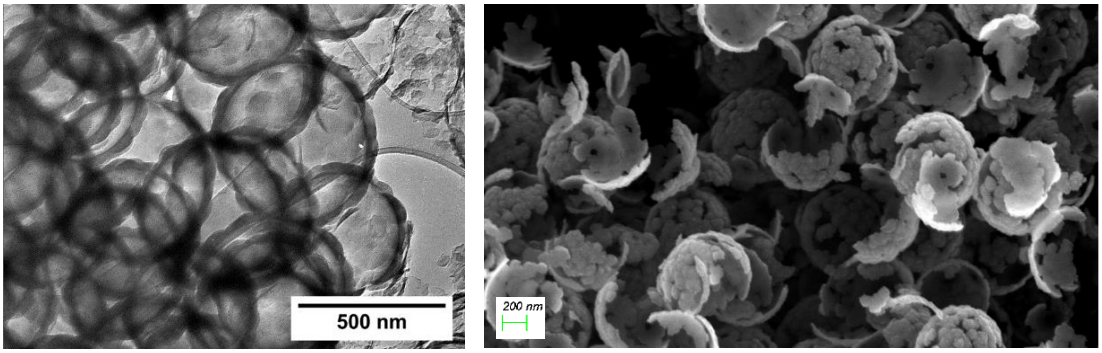

Figure 4.5: TEM image (left) and SEM image (right) comparison of the same HCNS sample showing how TEM can hide surface imperfections

4.6.4. Thermogravimetric Analysis (TGA)

TGA was used to characterise the graphitic carbon of the HCNS shells and solid carbon spheres. TGA was performed at the department of Process Engineering, Stellenbosch University and the Centre for Materials Engineering, University of Cape Town. In this investigation, the specific degree of graphitisation was not of

importance, TGA served as a tool to compare the carbon composition of the nanosphere samples.

To prepare the nanospheres for TGA, 10 mg of carbon powder was loaded into the TGA instrument where the sample was heated in a 20 % O_2 / 80 % N_2 atmosphere at a rate of 10 ^oC/min until 800 ^oC was reached. The TGA instrument returned the mass change-vs-temperature and the differential temperature gradient of the carbon's oxidation.

The differential temperature curves were used to characterise and compare the carbon nanosphere samples.

4.7. Powder Compaction

In this investigation, nanosphere powders were compressed in a punch and die powder compaction setup in order to extract qualitative information about the structural integrity of the nanospheres.

4.7.1. Experimental Setup

The powder compaction was performed with a punch and die setup on a 30 kN load frame MTS universal testing machine at the department of Mechanical Engineering, Stellenbosch University. Photographs of the setup are presented in Figure 4.6 and Figure 4.7. The punch and die dimensions and specifications are presented in Appendix A.7.

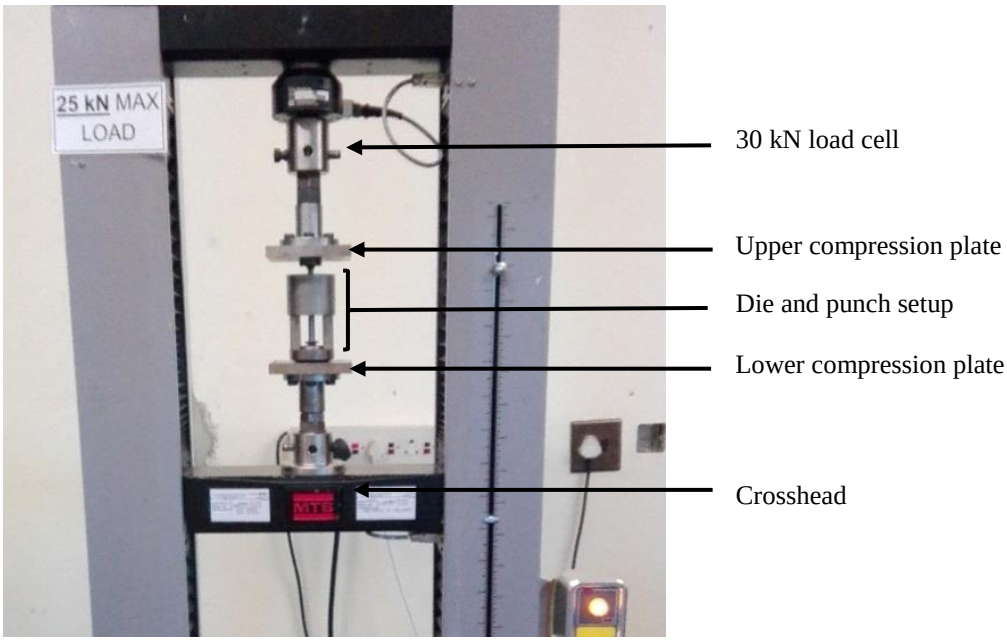

Figure 4.6: Powder compaction universal testing machine.

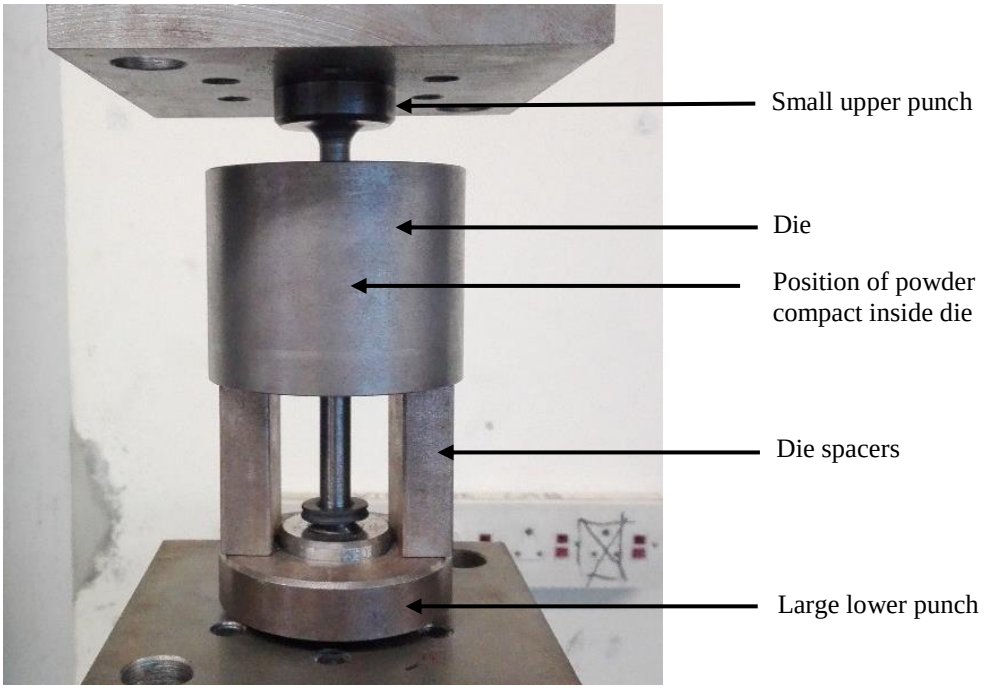

Figure 4.7: Punch and die setup

4.7.2. Experimental Procedure

The mass of powder loaded into the die was calculated so that the initial height of the compact was between 5 – 6 mm for the silica nanosphere samples and 6 – 8 mm for the carbon nanosphere samples. Since the silica and carbon nanospheres had different apparent densities, the sample masses were different. The masses required for each sample is summarised in Table 4.3.

Table 4.3: Powder compaction sample masses

Sample	Mass [mg]
Silica nanospheres	400
CVD HCNS	150
RF HCNS	40
Solid carbon spheres	150

The mass for RF HCNS was much lower than the CVD HCNS and solid carbon spheres since most of the CVD HCNSs were broken and flaky, increasing the apparent (packing) density of the powder compared to the whole spheres in the RF HCNS samples. The silica nanospheres were compacted first to test the setup and determine its sensitivity to nanosphere size.

To prepare the nanospheres for powder compaction, the sample was weighed and loaded into the punch and die setup. The punch and die setup was then hand-tapped until the powder had settled inside the die. The top punch was inserted into the die so that it was resting on the surface of the powder compact and the initial compact

height was measured and recorded. The punch and die setup was then placed between the compression plates of the universal testing machine.

The displacement and force channels were zeroed, and the crosshead velocity was set to 1 µm/second. The powder was then compressed until a compaction pressure of 10 kN was reached. The step-by-step procedure is presented in Appendix A.7.

4.8. Powder Compaction Model Fitting

After the nanosphere powders were compacted, the force-vs-displacement data was analysed and fitted to a powder compaction equation. The model fitting procedure is summarised in Figure 4.8.

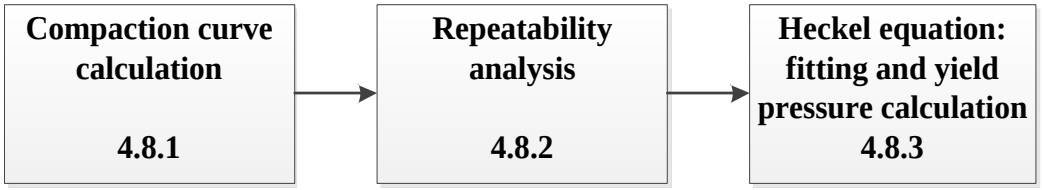

Figure 4.8: Powder compaction equation fitting overview

Each block in Figure 4.8 is further expanded on in the subsequent sections.

4.8.1. Compaction Curve Calculation

The force-vs-displacement data was recorded by the MTS universal testing machine for each powder compaction test. The preload of the small punch, 0.9753N, was added to the force data and then the data points were smoothed by applying an average filter of 20 points.

The compaction stages were mathematically calculated as follows:

- The static forces and rearrangement (S&R) stage was calculated to be the initial linear region. A linear trendline was fitted to the initial data and the end of this stage was demarcated when the R^2 value of the linear trendline was larger than 0.9. This was completed via an iterative approach and linear regression analysis using Microsoft Excel 2016.
- The rearrangement and deformation (R&D) stage was calculated to be the exponential region after the S&R stage, ending when the linear part of the D stage begins
- The deformation (D) stage was calculated to be the final linear region. A linear trendline was fitted to the final data and the beginning of this stage was demarcated when the R^2 value of the linear trendline was larger than 0.99. This was completed via an iterative approach and linear regression analysis using Microsoft Excel 2016.

An example of the compaction stages calculated for the compaction of S300 silica is presented in Figure 4.9.

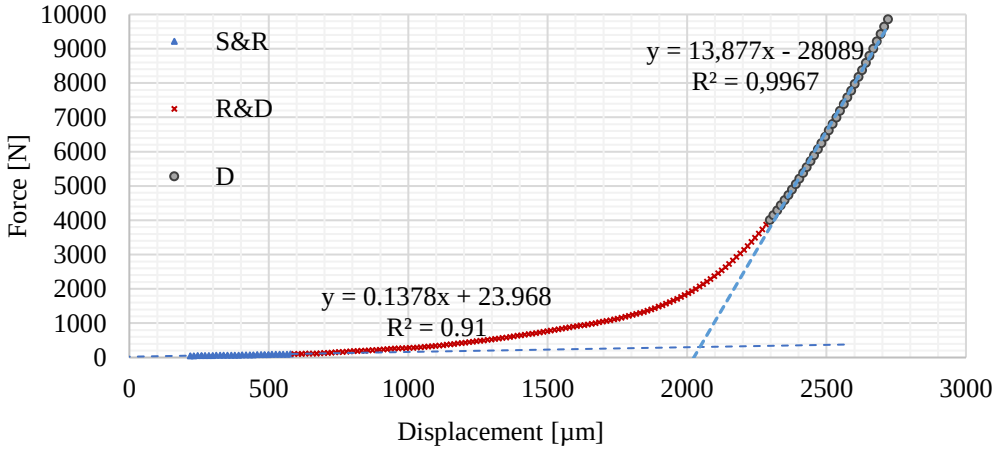

Figure 4.9: Compaction stages of a S300 silica nanosphere powder compaction run

The shape of the force-vs-displacement curve for each powder compaction run was very dependent on the initial apparent density of the powder, making it difficult to directly compare repeat runs of the sample powder. In order to overcome this problem, the force-vs-displacement data was presented as a fractional density-vs-compaction pressure curve. This relationship was denoted the compaction curve, and is not dependent on the initial apparent density of the powder.

The compaction curve of fractional density as a function of compaction pressure was calculated for each test from the smoothed raw data. The fractional compaction density was calculated by

$$\rho_c = \frac{m}{v * \rho_{\text{theoretical}}}, \tag{11}$$

where ρ_c denotes the fractional density of the compact, $\rho_{\text{theoretical}}$ denotes the theoretical density of the solid material and v denotes the volume of the powder compact.

The compaction pressure was calculated by

$$P_c = \frac{F}{A_c}, \tag{12}$$

where P_c denotes the compaction pressure, F denotes the force exerted by the punches and A_c denotes the cross-sectional area of the punch shaft.

In order to estimate the theoretical density of silica and carbon fully dense nanospheres, various literature sources were reviewed. Results from (Parnell, *et al.*, 2016) found porous Stöber silica spheres to have a density of 2040 – 2100 kg/m^3 and 2650 kg/m^3 for crystalline quartz. The porosity of the synthesised silica nanospheres was not known so 2500 kg/m^3 was chosen. Pure graphite has a density of approximately 2266 kg/m^3 (Poco Graphtie, 2015) so the HCNS graphitic carbon density was approximated as 2000 kg/m^3.

The theoretical density accuracy was not of importance since the Heckel yield pressure calculated from the compaction curves was purely qualitative for comparison. The bulk theoretical solid material density approximations for the nanospheres used in this investigation are summarised in Table 4.4.

Table 4.4: Theoretical solid density approximations

Sphere	$\rho_{theoretical}$ [kg/m^3]
Silica nanosphere	2500
RF, CVD and solid carbon nanosphere	2000

The mathematically determined compaction stages from the force-vs-displacement curve, as seen in Figure 4.9, can also be represented on the fractional density-vs-compaction pressure curve, named the compaction curve hereafter. Figure 4.10 presents the compaction stages of a compaction curve of S300 silica nanospheres.

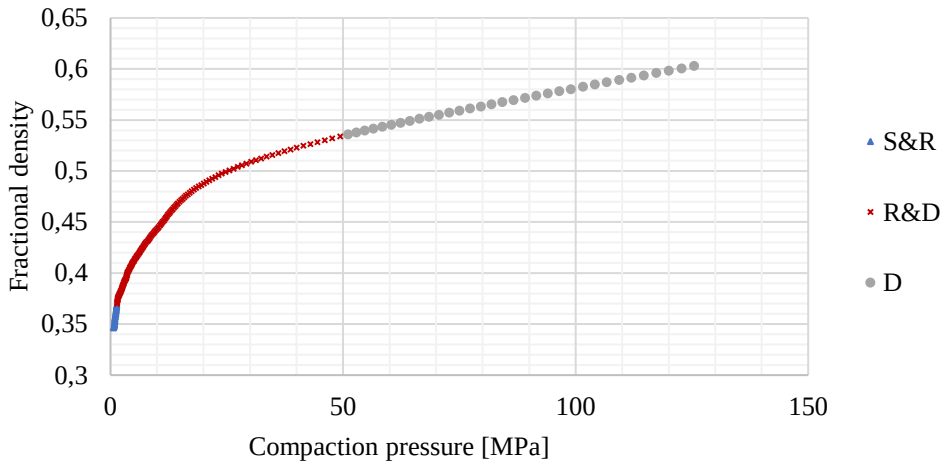

Figure 4.10: Compaction stages of compaction curve of S300 silica nanospheres

4.8.2. Repeatability

The repeatability of the tests was determined by calculating the test's precision. In order to do this, it was necessary to compare ρ_c data points at the same P_c increments. This was obtained by linearly interpolating the ρ_c data at 5 MPa P_c increments.

The fractional density average at each increment of P_c was calculated by

$$\bar{\rho}_{c,i} = \frac{\Sigma \rho_{c_{i,j}}}{N}, \tag{13}$$

where $\bar{\rho}_{c,i}$ denotes the fractional density average, i denotes a specific data point at the i_{th} pressure increment, j is the repeated test point and N is the number of test repetitions.

The fractional density average deviation was calculated by,

$$\Delta\overline{\rho_{c,i}} = \pm\frac{\sum|\rho_{c,i,j}-\overline{\rho_{c,i}}|}{N}, \quad (14)$$

where $\Delta\overline{\rho_{c,i}}$ denotes the fractional density average deviation.

The average deviation was chosen over using the standard deviation since less than five repetitive measurements were analysed (University of California, Irvine, 2013).

The average deviation at each P_c increment was calculated; error bars were used to represent the average deviation at each P_c increment in the plotted data. Figure 4.11 represents an example of the repeatability analysis over four compaction tests of S300 silica nanospheres.

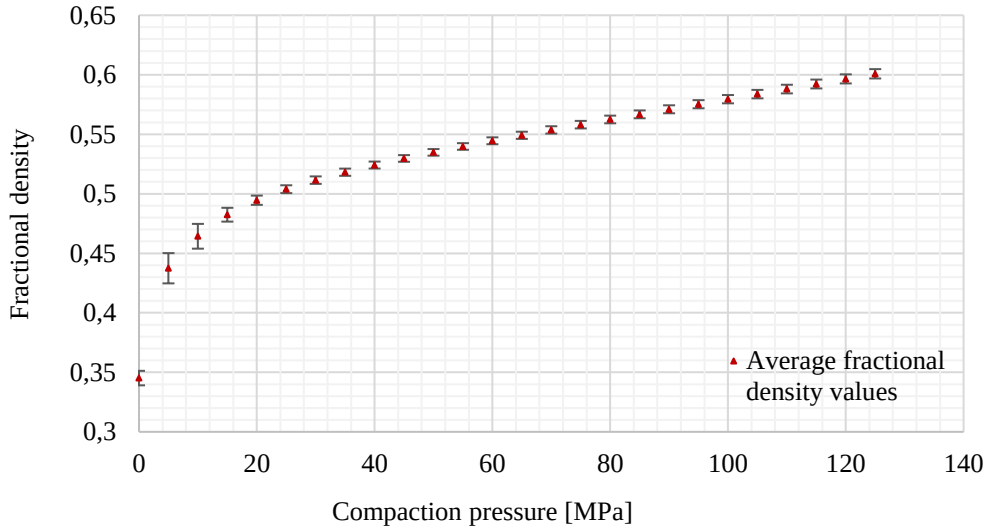

Figure 4.11: Repeatability analysis of four silica nanosphere compaction curves

From Figure 4.11 the average deviation errors bars were the largest in the beginning part of the compaction curve where the static forces and Van der Waals forces were overcome by the application of pressure. Since these forces are not uniform between powders, there is variation in the compaction curves during the particle rearrangement compaction stage. After this initial S&R compaction stage, the average deviation reduced.

4.8.3. Heckel Equation: Fitting and Yield Pressure Calculation

The next step of the analysis was to fit a compaction equation to the data. The Heckel equation was chosen specifically to calculate P_y, the Heckel yield pressure.

The experimental compaction data was linearised using Equation 8 in Section 3.3.2, repeated here for reference,

$$\underbrace{\ln\frac{1}{\epsilon}}_{Y} = \underbrace{\ln\left(\frac{1}{\epsilon_0}\right)}_{C} + \underbrace{KP}_{mX} \quad (15)$$

The experimental data was then plotted as $Y = \ln\left(\frac{1}{\epsilon}\right)$ vs $X = P_c$ and the linear trendline was calculated by linear regression analysis, using Microsoft Excel 2016's linear trendline function. The R^2 value from the linear regression analysis of ≥ 0.95 was considered a good fit. If the linear trendline correlation was considered accurate, the Heckel model parameters, $\ln\left(\frac{1}{\epsilon_0}\right)$ and K were determined from the trendline equation, where K indicates the gradient and $\ln\left(\frac{1}{\epsilon_0}\right)$ the y- intercept of Equation 15.

From these Heckel model parameters, the Heckel compaction curve was calculated using Equations 9 and 10, repeated here for reference,

$$\epsilon_{\text{Heckel}} = \epsilon_{0_{\text{Heckel}}} e^{KP_c} \tag{16}$$

$$\rho_{\text{Heckel}} = 1 - \epsilon_{\text{Heckel}} \,. \tag{17}$$

The experimental data and Heckel compaction curves as a function of compaction pressure were then superimposed for direct comparison.

An example of the Heckel compaction curves superimposed on the experimental compaction curve is presented in Figure 4.12 for a S300 silica nanosphere compaction.

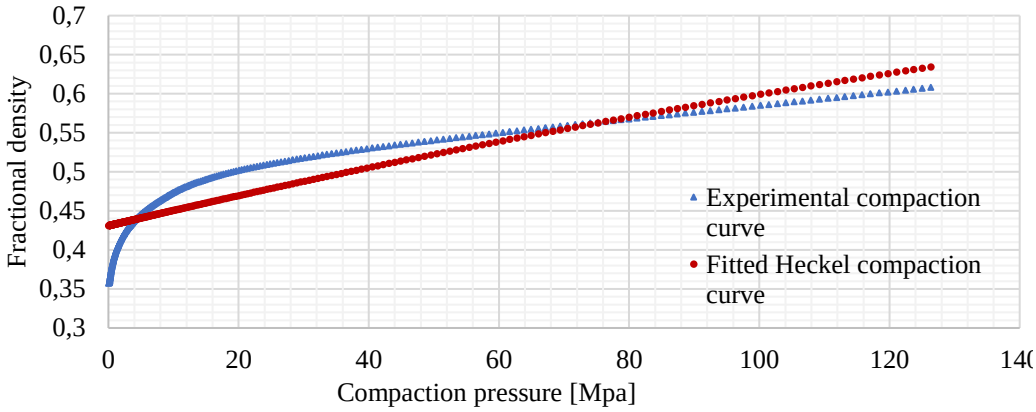

Figure 4.12: Example of Heckel compaction curved superimposed to an experimental compaction curve

As is illustrated in the example shown in Figure 4.12, fitting the data over the entire compaction curve to the Heckel equation results in inaccurate representation of the compaction behaviour, especially in the initial S&R compaction stage. This is expected since the compaction curve contains all three stages of compaction; S&R, R&D and D. Each of these stages is dominated by a different compaction mechanism. The Heckel equation cannot accurately model more than one compaction mechanism simultaneously and must therefore be fitted to each compaction stage separately (Denny, 2002).

Since the R&D stage is a combination of rearrangement and deformation of the particles, the densification behaviour is a combination of both the pure rearrangement (S&R) and pure deformation (D) stages. Therefore, the Heckel equation was separately fitted to the S&R and D stages, and then extrapolated until they intercept. The Heckel compaction curve stages were then superimposed on the experimental compaction curve and compared. An example of this multiple Heckel fitting is presented in Figure 4.13.

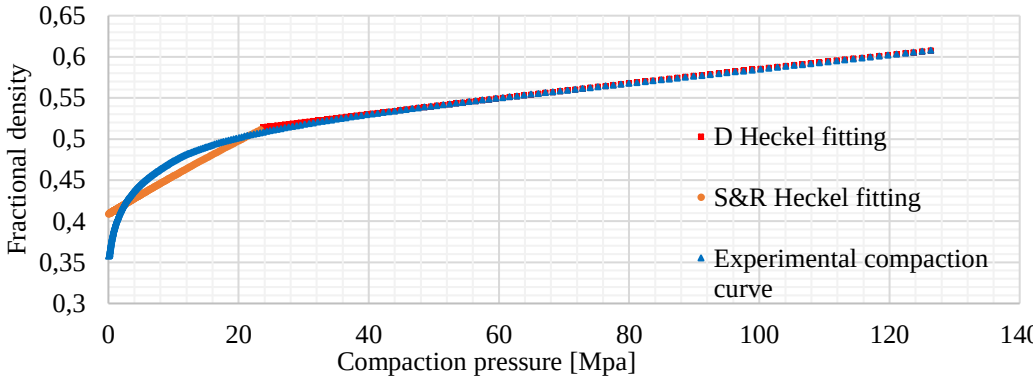

Figure 4.13: Example of multiple Heckel fitting for a S300 silica nanosphere compaction test superimposed on the experimental compaction curve

Comparing the Heckel compaction curves in Figure 4.12 and Figure 4.13, the multiple Heckel fitting compaction curve approximated the experimental compaction curve more accurately. To quantify the comparison, the error was calculated between the Heckel and experimental compaction curves using the RMS error, presented by,

$$RMS_{\text{error}} = \sqrt{\frac{\Sigma\left(\rho_{\text{cExperimental}} - \rho_{\text{cHeckel}}\right)^2}{N}}. \tag{18}$$

The RMS error for the single Heckel fitting of the example S300 compaction presented in Figure 4.12 was 0.414 while the multiple Heckel fitting error in Figure 4.13 was 0.099. The lower RMS error for the multiple Heckel fitting confirms that it yielded a more accurate approximation of the experimental compaction curves.

For the Heckel yield pressure calculation, only the D compaction stage was considered. This was because the D stage was the only stage that contained one compaction mechanism as well as where the spheres deform.

The Heckel yield pressure was calculated from the D stage Heckel fitting parameters. For the S300 silica nanosphere example presented in Figure 4.13, the Heckel parameter, K, was calculated from the linear trendline of the D compaction stage. The Heckel yield pressure was then calculated using $P_{\text{y}} = \frac{1}{K}$.

5. Results, Analysis and Discussion

The following section presents the results and discussions of the procedures followed in the methodology to obtain the investigation's objectives.

5.1. Silica Nanosphere Synthesis and Characterisation

5.1.1. Sample Summary

Three sizes of silica nanospheres were synthesised according to the procedure presented in Section 4.1.1. The samples were labelled S200, S300 and S400 respectively.

SEM images were taken of the silica samples to determine the surface structure and shape. SEM images of the samples are presented in Figure 5.1.

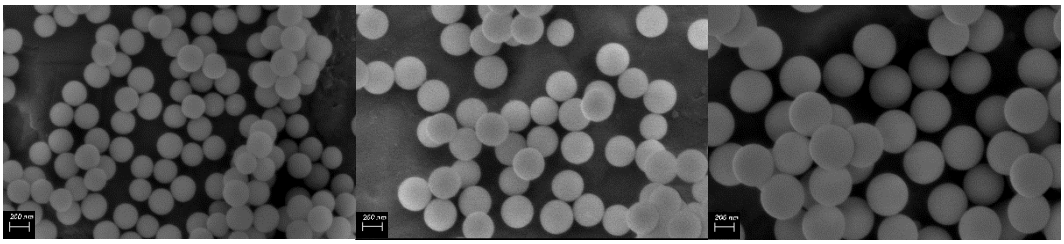

Figure 5.1: SEM images of S200 (left), S300 (middle) and S400 (right) silica nanospheres taken at the same magnification

From Figure 5.1 it was concluded that the silica samples contained spherical silica nanospheres with a uniform surface structure.

The silica PSD was then determined from the Zetasizing characterisation procedure presented in Section 4.6.1. The investigation of sample preparation factors was first completed, with the initial number PSD results presented in Figure 5.2.

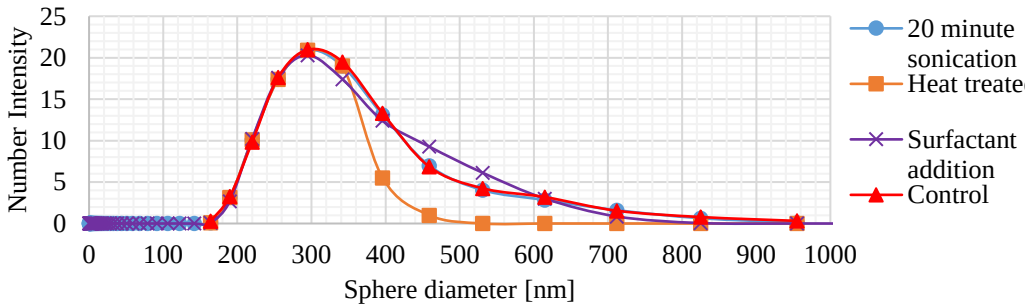

Figure 5.2: Initial number PSD results for 200 nm silica nanospheres with varying sample preparation techniques where the control sample was only sonicated for 10 minutes.

From the results in Figure 5.2, it was decided for sample preparation, the spheres were first heat treated in a furnace at 250 ºC for 1 hour. After cooling to room temperature, 2 mg of dried silica powder and 5 mL of distilled water was added to a glass sample vial. The vial was then sonicated for 10 minutes so that a homogenous suspension was formed.

The results of the Zetasizing for the three silica nanosphere samples are summarised in Table 5.1 with the raw data in Appendix B.1.

Table 5.1: Silica PSD from Zetasizing

Sample label	Peak mean [nm]	Standard deviation [nm]
S200	283.6	68.62
S300	323.0	84.35
S400	419.8	102.4

The Zetasizer results seemed to overestimate the peak means for the silica samples with relatively large deviations. Therefore, MATLAB image processing was used on the samples to calculate the mean and standard deviation of the PSD based on three SEM images per sample. The image processing algorithm used the MATLAB function *imfindcircles* which detected circles in an image based on the circular Hough transform. The code, images and supplementary information is presented in Appendix B.2.

The results of the PSD are summarised in Table 5.2.

Table 5.2: Silica PSD from SEM images

Sample label	Mean [nm]	Standard deviation [nm]
S200	236.75	17.41
S300	309.46	17.33
S400	416.32	14.82

From comparing the results from the Zetasizing in Table 5.1 and the SEM characterisation in Table 5.2, it was seen that the Zetasizing overestimated the PSD for all the samples. The standard deviations of the Zetasizing were much higher than the SEM standard deviations. This was consistent with results of gold nanoparticle PSD characterisation in (Khlebtsov & Khlebtsov, 2011) and therefore the SEM PSD results were used for this investigation.

As noted in Section 4.1.1, the process parameters for accurately synthesising specific nanosphere diameters is based on a trail-and-error approach. The PSDs reported in Table 5.2 were deemed close enough to the desired 200, 300 and 400 nm diameters for the purpose of this investigation.

5.2. CVD HCNS Synthesis and Characterisation

5.2.1. Sample Summary

CVD HCNSs were synthesised using the S300 and S400 silica templates with the procedure and synthesis variations presented in Section 4.1.2 and Table 4.1 respectively. The sample labels of the HCNSs with their size and synthesis variables are summarised in Table 5.3.

Table 5.3: CVD HCNS sample summary

Sample label	Silica nanosphere template	Argon flow rate [mL/min]	Toluene temperature [^{0}C]	Template mass [g]
CVD01	S300	100	25	0.5
CVD02	S300	150	25	0.5
CVD03	S300	200	25	0.5
CVD04	S300	150	75	0.5
CVD05	S300	100	75	0.5
CVD06	S300	200	75	0.5
CVD07	S300	150	25	0.2
CVD08	S300	150	25	1
CVD09	S400	150	25	0.2
CVD10	S400	150	25	0.5
CVD11	S400	150	25	1

With these samples the following relationships were determined using SEM characterisation:

- The effect of argon flow rate on the spherical structure of the HCNSs.
- The effect of toluene temperate on the spherical structure of the HCNSs.
- The effect of template mass on spherical structure of the HCNSs.

None of the CVD synthesis procedures produced whole HCNSs. In order to characterise the structure of the CVD synthesised HCNSs, characterisation terms were defined, presented in Table 5.4.

Table 5.4: CVD HCNS characterisation terms

Characterisation term	Explanation	SEM image example
Sphere flakes	The whole sampled consisted of broken sphere flakes, with no partial spheres.	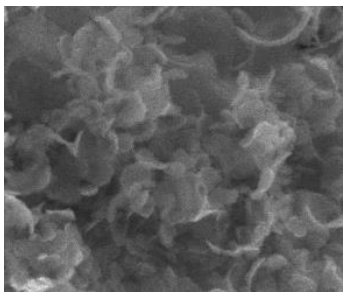
Broken partial spheres	The sample consisted of mostly flakes as well as a few partial spheres.	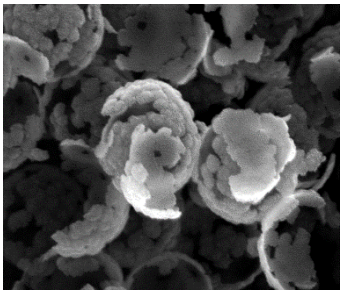
Partial spheres	The sample consisted of mainly partial spheres and some flakes.	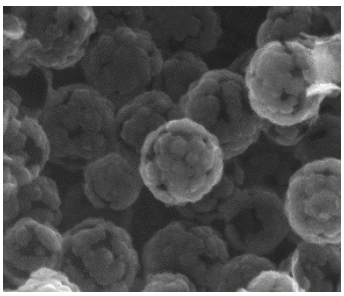
Agglomerated spheres	The sample consisted of over coated spheres that were bonded together.	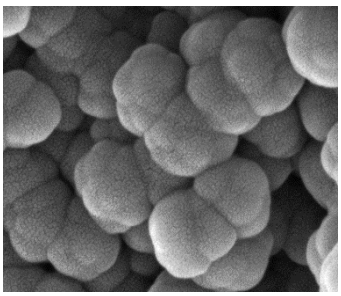

5.2.2. The Effect of Argon Flow Rate

In order to test the effect argon flow rate and consequently carbon precursor flow rate had on the CVD HCNS spherical structure, three argon flow rates were tested.

After CVC HCNS synthesis, HF treatment and heat treatment, SEM images were taken of samples, CVD01, CVD02 and CVD03. The SEM images are presented in Figure 5.3 - Figure 5.5.

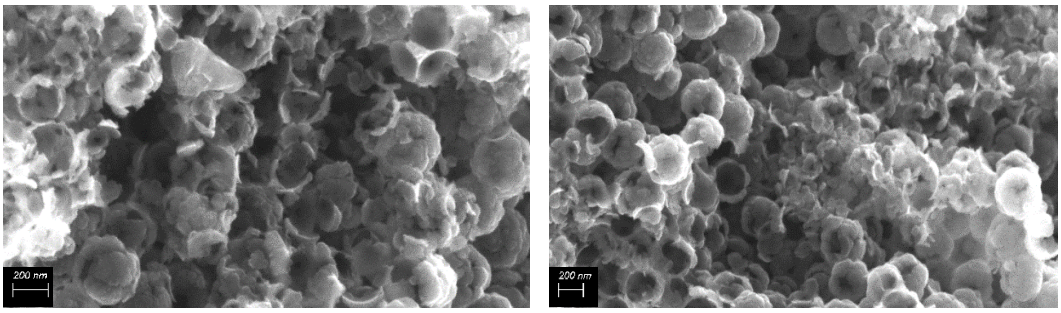

Figure 5.3: CVD01 (broken partial spheres) SEM images with a 100 mL/min argon flow rate

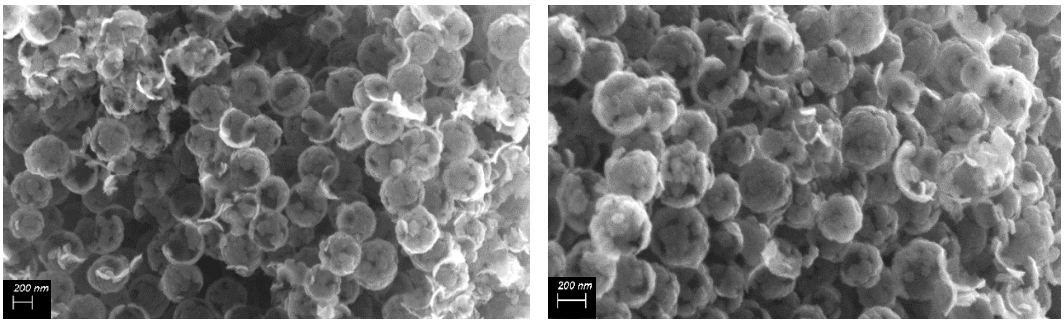

Figure 5.4: CVD02 (partial spheres) SEM images with a 150 mL/min argon flow rate

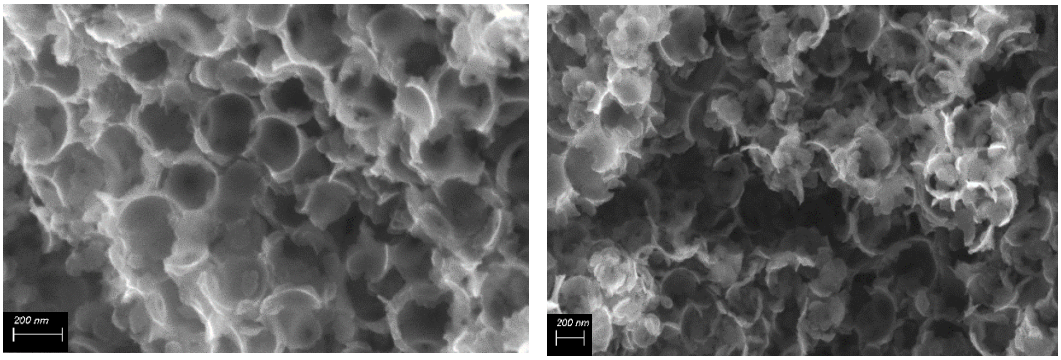

Figure 5.5: CVD03 (sphere flakes) SEM images with 200 mL/min argon flow rate

As seen in Figure 5.3 - Figure 5.5, none of the samples produced whole spherical structures. The 100 mL/min argon flow rate produced mostly sphere flakes with a few partial spheres. The 150 ml/min flow rate produced mainly partial spheres and the 200 mL/min argon flow rate produced only sphere flakes. It was concluded that 150 mL/min argon flow rate was the best option out of the three experiments, however not enough toluene vapour was being carried into the hot zone of the furnace to form a full shell of graphitic flakes on the silica templates.

The result of argon flow rate affecting the template coverage was similar to the effect of varying the residence time in the results of (Su, *et al.*, 2006), presented in Figure 5.6.

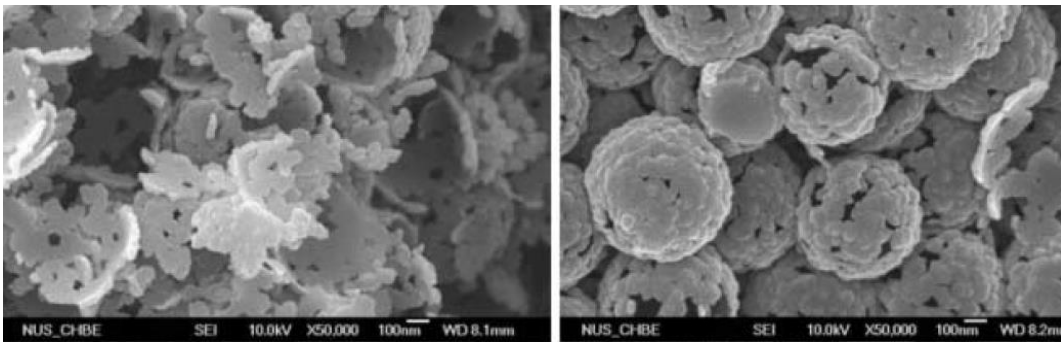

Figure 5.6: SEM images of HCNS synthesised via CVD with benzene as the carbon precursor and 1 hr residence time resulting in sphere flakes (left) and 2.5 hrs residence time resulting in partial spheres (right) (Su, *et al*., 2006)

Varying the argon flow rate or residence time of the CVD synthesis method affected the amount of carbon precursor reaching the hot zone of the tube furnace and depositing as graphitic flakes on the silica nanosphere templates. In order to increase the carbon coating, the amount of carbon precursor reaching the hot zone should be increased.

5.2.3. The Effect of Toluene Temperature

In an attempt to increase the amount of toluene vapours being carried into the hot zone of the furnace, the toluene was heated to 75 ^{o}C in the bubbler. SEM images were taken of CVD04 after synthesis, but before HF and heat treatment as presented in Figure 5.7.

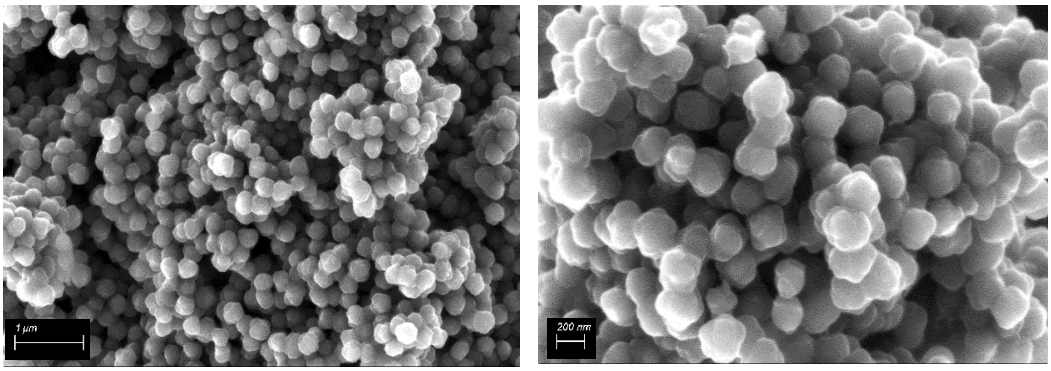

Figure 5.7: SEM images of CVD04 before template removal, showing agglomerated spheres

The HCNS in Figure 5.7 showed larger clumped flakes on the agglomerated spheres when compared to the partial spheres in Figure 5.4, where the only variation in synthesis was the toluene temperature. This uneven coating was not ideal since the HCNSs were still not spherical in structure. After template removal and heat treatment, the agglomerated HCNS resulted in sphere flakes, as presented in Figure 5.8.

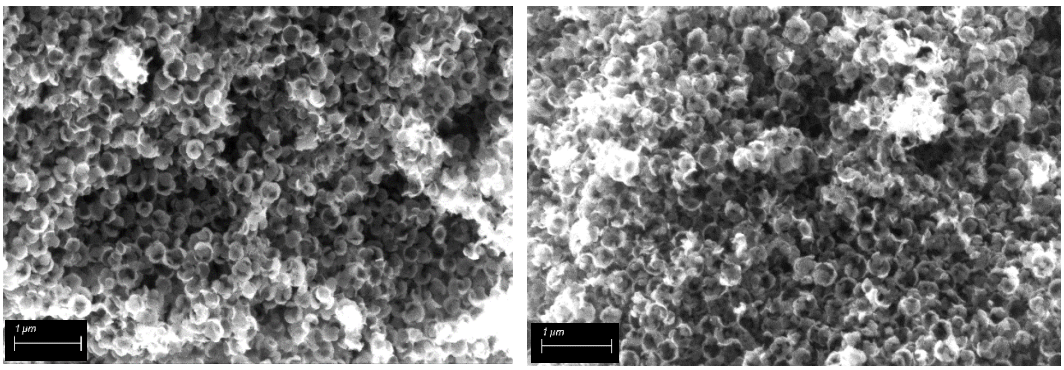

Figure 5.8: SEM image of CVD04 after template removal resulting in sphere flakes

To further investigate the effect of toluene temperature on the spherical structure of the CVD HCNS, samples CVD05 and CVD06 were synthesised with argon flow rates of 100 mL/min and 200 mL/min respectively. SEM images were taken of these two samples before template removal and presented in Figure 5.9.

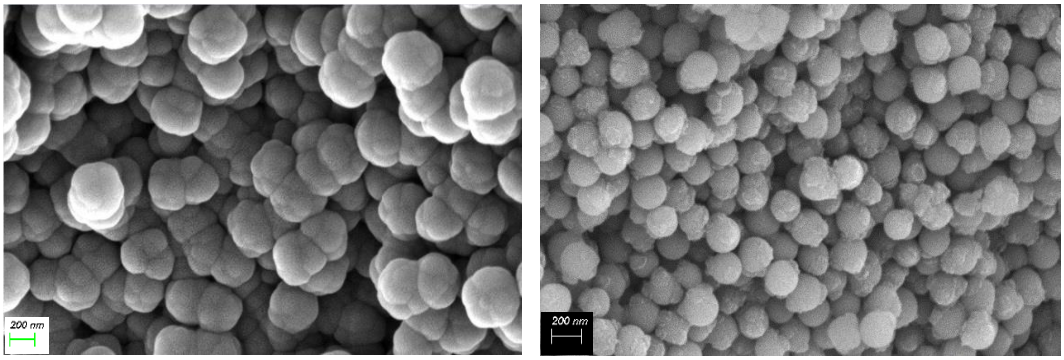

Figure 5.9: SEM image of CVD05 (agglomerated spheres) (left) and CVD06 (partially covered silica spheres) (right)

From Figure 5.7 and Figure 5.9 it was seen that decreasing the argon flow rate from 150 mL/min to 100 mL/min while keeping the toluene temperature at 75 ^{o}C increased the amount of graphitised carbon coverage on the silica templates. The results from the 200 mL/min argon flow rate showed insufficient coverage, showing that the toluene vapours did not have sufficient time in the hot zone to deposit graphitised flakes on the silica nanosphere templates.

However, even though the silica templates were completely covered in the CVD05 (agglomerated spheres) sample, the graphitised flakes produced by the heated toluene were far thicker than the room temperature toluene experiments. These thick flakes appear to clump together and bond the HCNSs together forming agglomerates which resulted in sphere flakes after template removal as seen in Figure 5.8.

It was concluded that heating the toluene in the bubbler increased the thickness of graphitised carbon flakes and resulted in an uneven carbon coating. It was also seen that the argon flow rates and toluene temperature were not independent synthesis

variables but depend on other variables for the resulting spherical structural integrity of the CVD HCNSs.

5.2.4. The Effect of Template Mass

Toluene at 25 ^{o}C provided a more uniform carbon coverage than toluene at 75 ^{o}C. However, even at the best argon flow rate out of the three tests, 150 mL/min, the spheres did not have complete spherical structures. In order to increase the sphere coverage without heating the toluene, the mass of the silica nanosphere templates was varied. Samples CVD07, CVD02 and CVD08 were synthesised, HF treated and heat treated to compare the effect of silica nanosphere template mass on the carbon coating. Figure 5.10 - Figure 5.12 presents the SEM image comparisons.

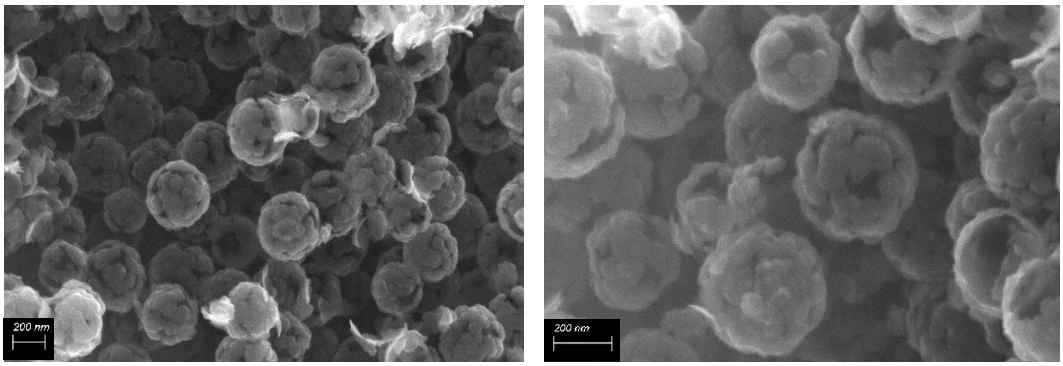

Figure 5.10: SEM images of CVD07 (partial spheres) with 0.1 g silica nanospheres

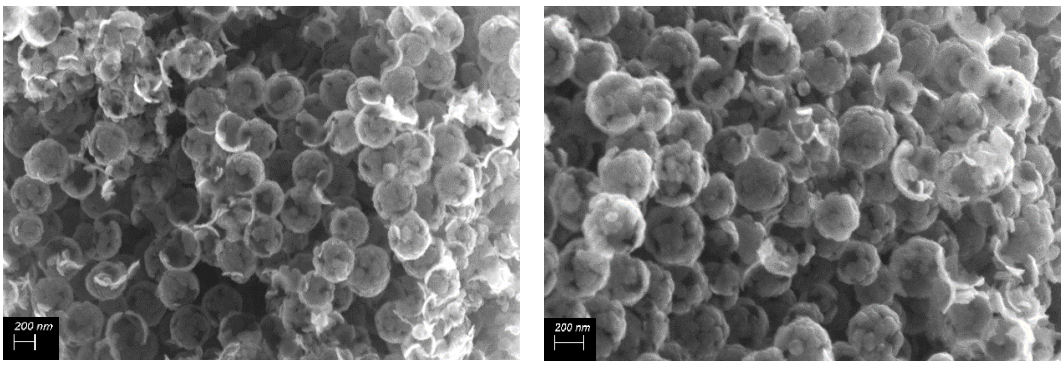

Figure 5.11: SEM images of CVD02 (partial spheres) with 0.5 g silica nanospheres

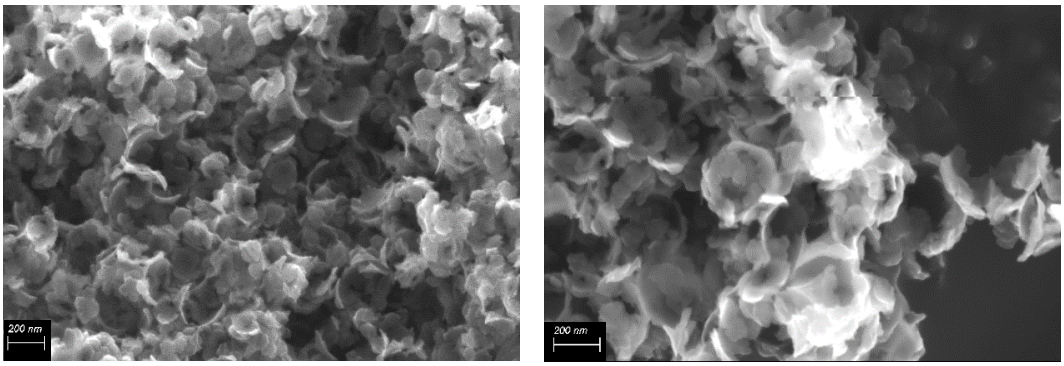

Figure 5.12: SEM images of CVD08 (sphere flakes) with 1 g silica nanospheres

From Figure 5.10 - Figure 5.12 it was seen that the template mass had a large effect on the spherical structure of the CVD HCNS. The results from CVD07 with a template mass of 0.1 g showed HCNSs with the best coverage. However, the spheres were still only partially formed.

Also, synthesising CVD HCNS in batches of only 0.1 g of silica template at a time was not scalable for powder compaction purposes since each CVD run would only produce about 3 mg of CVD HCNSs but a minimum of 150 mg of CVD HCNSs were required per powder compaction test.

It was concluded that the CVD synthesis variables had large effects on the spherical structure of the HCNSs. Variables such as argon flow rate, residence time and silica nanosphere template mass were also dependent on each other and could not be optimised separately.

5.2.5. Shell Structure

To investigate the carbon bonding structure of the CVD HCNSs, TGA was performed on samples CVD02 (partial spheres) and CVD04 (sphere flakes). The CVD02 sample was synthesised with toluene at 25 °C and argon flow rate of 150 mL/min and the CVD04 sample was synthesised with toluene at 75 °C and argon flow rate of 150 mL/min. These samples were chosen to determine the effect the toluene temperature has on the carbon bonding structure.

The mass loss rate or differential temperature gradient (DTG) results for the two CVD HCNS samples are presented in Figure 5.13. The additional TGA curves are presented in Appendix C.1.

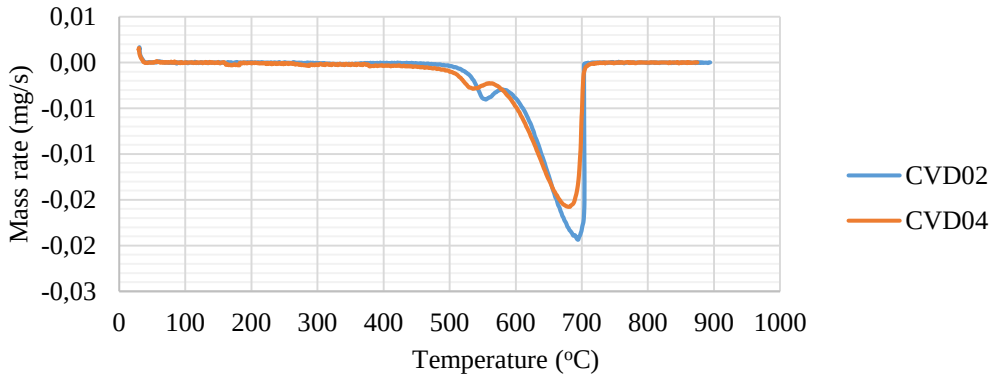

Figure 5.13: DTG results for CVD02 (25 °C toluene) and CVD04 (75 °C toluene)

The DTG for CVD02 showed two troughs, one at approximately 550 °C and the other at 690 °C. The smaller first through corresponded to amorphous carbon. However, since the trough was small, only a small amount was present in the CVD02 HCNS sample. The second trough corresponded to the graphitic carbon flakes.

The DTG results for CVD04 showed similar results to CVD02. A small trough at approximately 540 °C corresponded to the presence of amorphous carbon while the

larger trough at approximately 680 °C corresponded to the graphitic carbon flakes. This second trough was only 10 °C lower tat the second CVD02 trough, therefore from these initial results the toluene temperature did not seem to largely affect the carbon bonding structure of the CVD HCNSs.

The temperature of the DTG troughs as well as the width gave an indication of the degree of graphitisation and the presence of defects in the graphitic structure. Results from (McKee & Vecchio, 2006) shows TGA results from mixtures of amorphous carbon, carbon nanotubes and pure graphite. The results are presented in Figure 5.14.

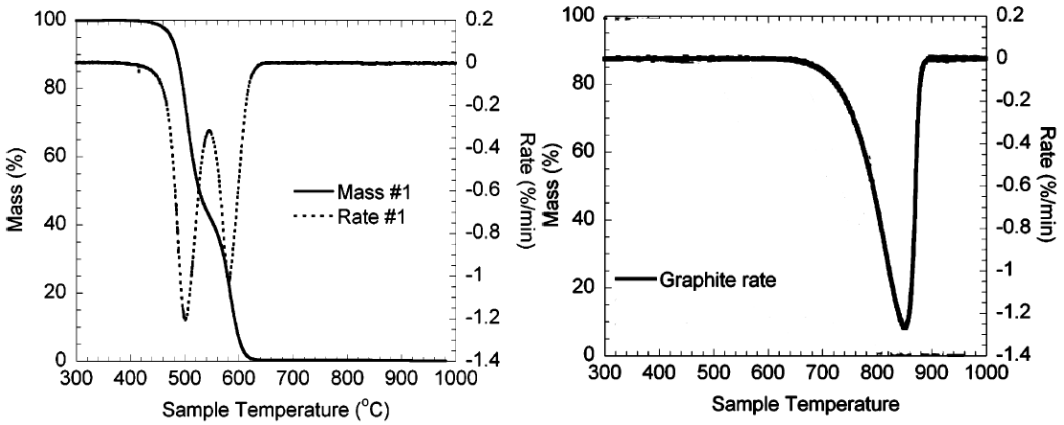

Figure 5.14: TGA results adapted from (McKee & Vecchio, 2006) where sample #1 was a combination of amorphous carbon and carbon nanotubes synthesised at 800 °C

The DTG results from Figure 5.14 showed troughs at 500 °C corresponding to amorphous carbon, 580 °C corresponding to carbon nanotubes and 850 °C corresponding to pure graphite. The DTG trough from the graphitic carbon shell in the CVD HCNSs was around 680 °C, indicating that the degree of graphitisation of the CVD HCNS shells was lower than pure graphite but higher than the carbon nanotubes synthesised by (McKee & Vecchio, 2006). Since carbon nanotubes were expected to have a higher degree of graphitisation due to their single-walled graphene structure, this result could be attributed to the fact that the CVD HCNSs were synthesised at 900 °C, compared to the 800 °C synthesis temperature of the carbon nanotubes. Higher temperatures had been proved to increase the degree of graphitisation of carbon nanostructures. (McKee & Vecchio, 2006).

To better understand the graphitic carbon structure of the CVD HCNS shells, high resolution TEM images were taken of sample CVD02 (partial spheres), presented in Figure 5.15.

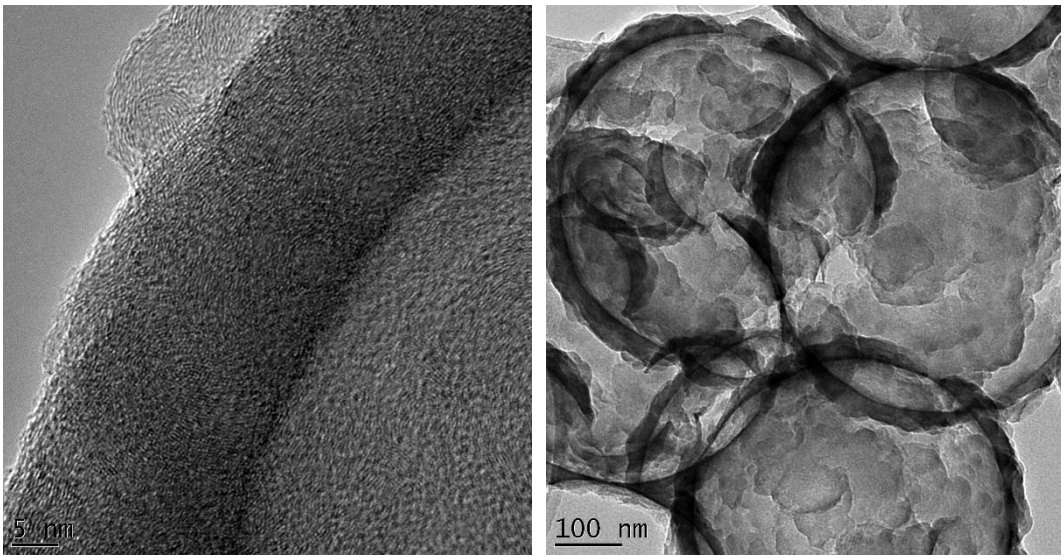

Figure 5.15: High resolution TEM images of CVD02 (partial spheres) HCNS shell showing the shell thickness

From the TEM images in Figure 5.15, the randomly oriented graphitised flakes can be seen forming a fingerprint-like structure. These random orientations are what give the graphitised carbon nanostructures their strength and thermal and electrical conductivity in all directions. Pure graphite only possesses strength and high conductivities in-plane.

The CVD02 (partial spheres) TEM images seen in Figure 5.15 showed a similar graphitised structure to the graphitised outer structure of carbon spheres synthesised by (Yoshizawa, *et al*., 2006), presented in Figure 5.16. These spheres had a higher degree of graphitisation than the CVD HCNSs.

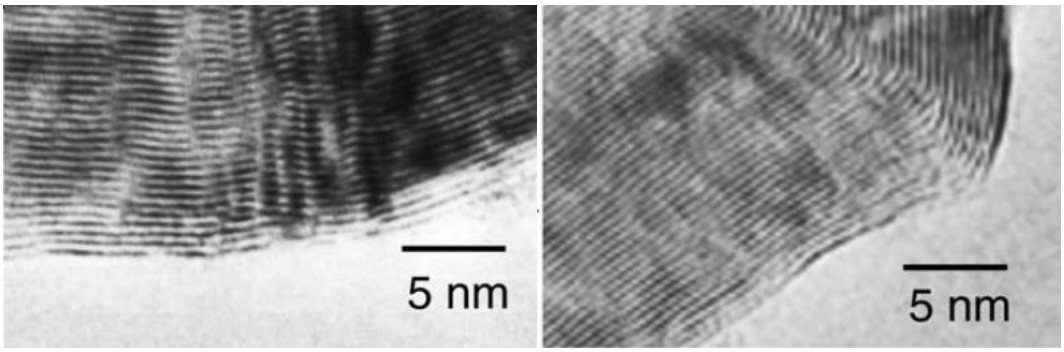

Figure 5.16: TEM images of carbon spheres with graphitised outer structures from (Yoshizawa, *et al*., 2006).

5.3. CVD Solid Carbon Sphere Synthesis and Characterisation

5.3.1. Sample summary

Solid carbon spheres were synthesised following the procedure in Section 4.4. The solid sphere sample, SCS01, served as a structural integrity comparison to the CVD

HCNSs. The spheres were not expected to be perfectly spherical in structure or uniform in size due to the lack of template in the synthesis method.

SEM images were used to characterise the solid carbon sphere surface structure and shape. Figure 5.17 presents SEM images of the carbon sphere sample, SCS01.

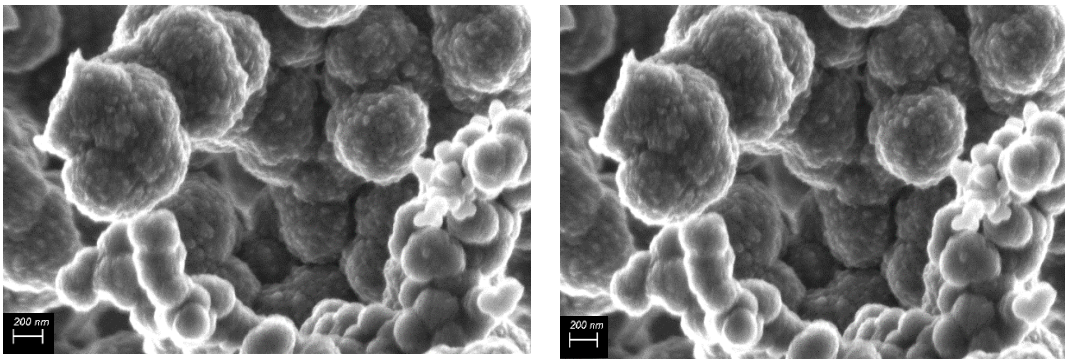

Figure 5.17: SEM images of SCS01showing the large PSD and non-uniform shape

The SEM images in Figure 5.17 showed carbon globules with a wide size distribution from 100 to 2000 nm in diameter. The structure of the spheres was also non-uniform.

5.3.2. Sphere structure

TGA was performed on the solid carbon sphere sample SCS01 with the results presented in Figure 5.18.

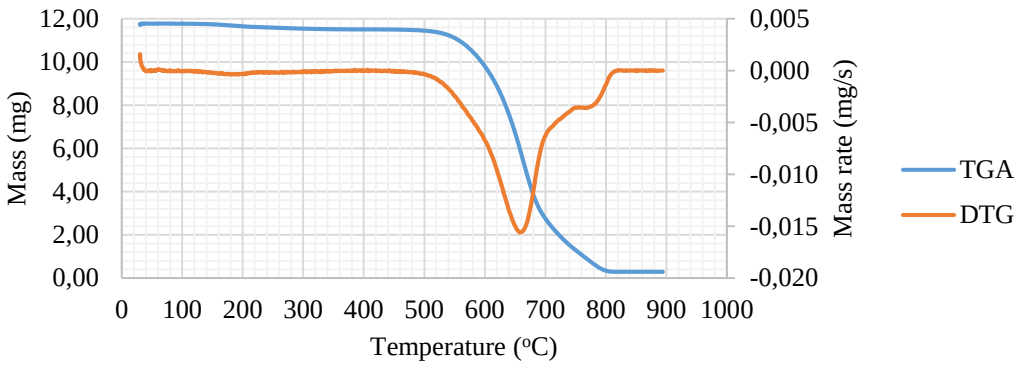

Figure 5.18: TGA and DTG results of SCS01

The TGA results in Figure 5.18 showed that the solid carbon spheres and CVD HCNSs had very similar carbon shell structures. The trough at a lower temperature of 660 °C and wider trough distribution indicated a slightly lower degree of graphitisation of the spheres.

High resolution TEM images were taken of the solid CVD spheres to further investigate the carbon structure and internal features. The TEM images of SCS01 are presented in Figure 5.19.

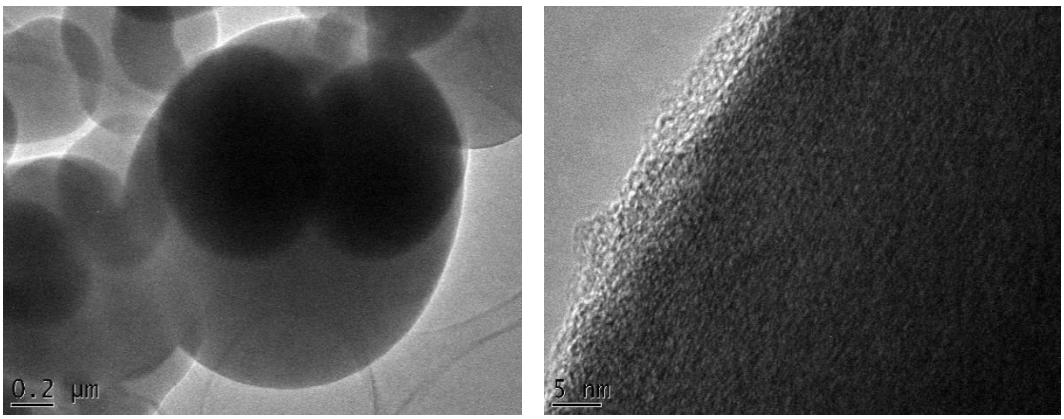

Figure 5.19: TEM images of SCS01 showing the solid structure and graphitic carbon

The TEM images in Figure 5.19 confirmed that the carbon spheres were indeed solid. The carbon structure of the solid spheres appeared slightly less graphitic compared to the high resolution TEM images of the CVD HCNSs. This was consistent with the TGA results.

5.4. RF HCNS Synthesis and Characterisation

5.4.1. Sample Summary

Three samples of RF HCNSs were investigated, namely RF01, RF02 and DRF01. RF01 and RF02 were synthesised following the procedure in Section 4.1.3 and DRF01 was doped with nitrogen following the procedure presented in Section 4.5. EDS and elemental analysis were used to confirm the success of the nitrogen-doping, presented in Appendix C.2.

SEM characterisation provided information about the spherical structure of the RF HCNSs. Figure 5.20 - Figure 5.22 presents SEM images of the three RF HCNS samples.

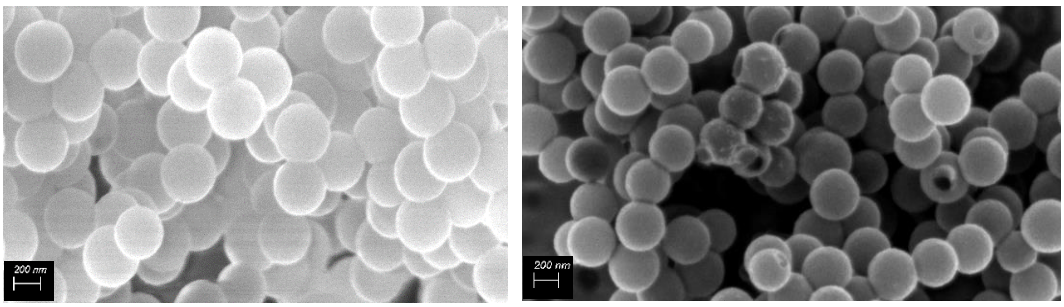

Figure 5.20: SEM images of RF01 showing small silica particles and vacuum holes in the right image.

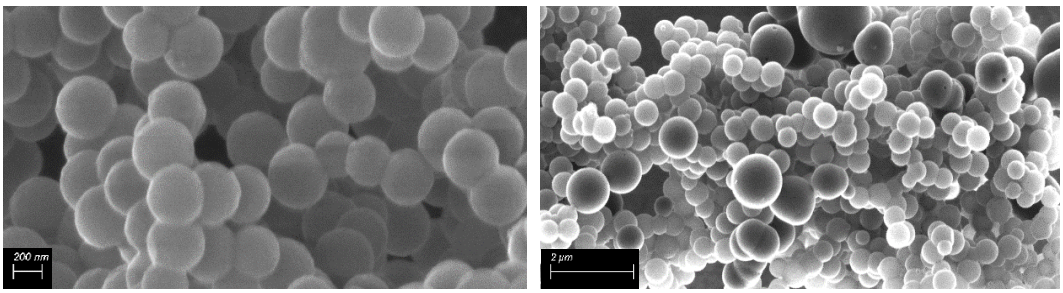

Figure 5.21: SEM images of RF02 showing the presence of large solid carbon impurities in the right image.

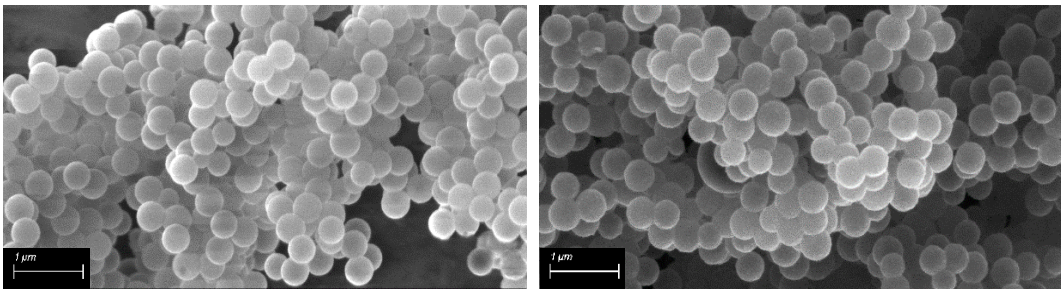

Figure 5.22: SEM images of DRF01, nitrogen doped RF01 where no visible difference can be seen between the DRF01 and RF01 samples.

From Figure 5.20 and Figure 5.21 it was seen that the RF method produced whole spherical particles that were not broken. The surface of the carbon shells also appeared much smoother that the CVD HCNSs.

The SEM image on the right of Figure 5.20 showed small particles on the surface of some of the spheres. EDS was performed on these spheres and it was found the particles were composed of silica. Small holes were also present in some of the spheres. It was hypothesised that these holes were not originally present but were a result of the vacuum inside the SEM. These 'vacuum holes' also occurred in hollow silica particles in (van Wijk, *et al*., 2013).

The SEM image on the right of Figure 5.21 showed large impurities around the HCNS. EDS was performed on the impurities where they were found to be composed of carbon. It was unknown what caused these impurities and it was hypothesised that they would severely affect the powder compaction results.

From the SEM images of DRF01, the nitrogen doped RF01 spheres in Figure 5.22, no major structural differences between these two samples could be seen.

From the SEM images it was seen that the samples contained spherical HCNSs centred on an average particle size of approximately 460 nm. Since the silica nanosphere PSD information was not available, the PSD was determined with TEM images.

TEM characterisation provided information about the internal structure, PSD and shell thickness of the RF HCNSs. Figure 5.23 - Figure 5.25 presents TEM images of the three RF HCNS samples.

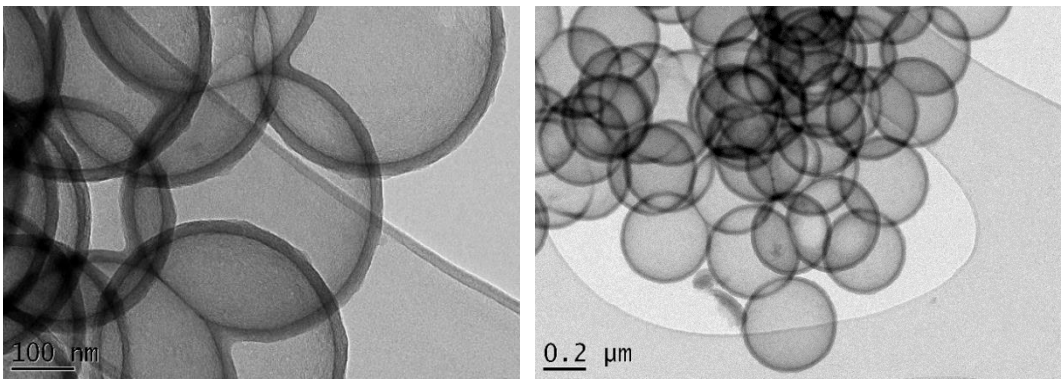

Figure 5.23: TEM images of RF01 showing hollow spheres with removed silica template

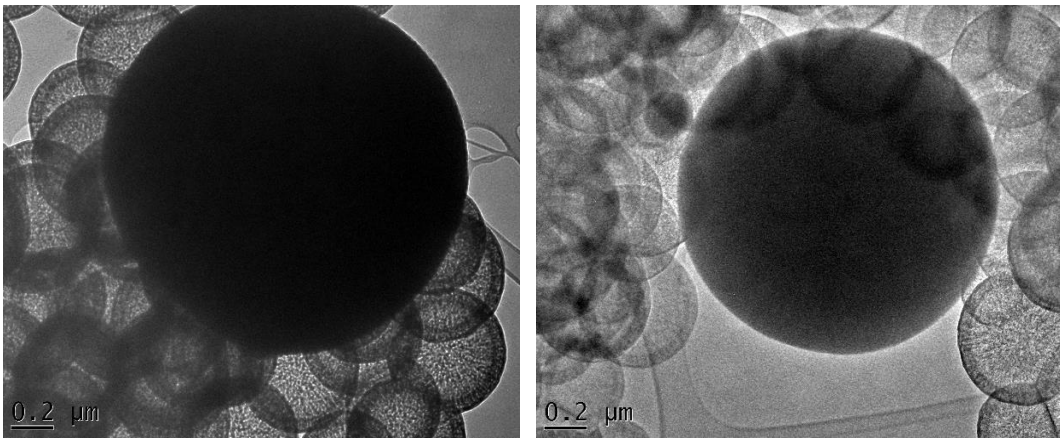

Figure 5.24: TEM images of RF02 showing hollow spheres with removed silica template plus large solid impurities

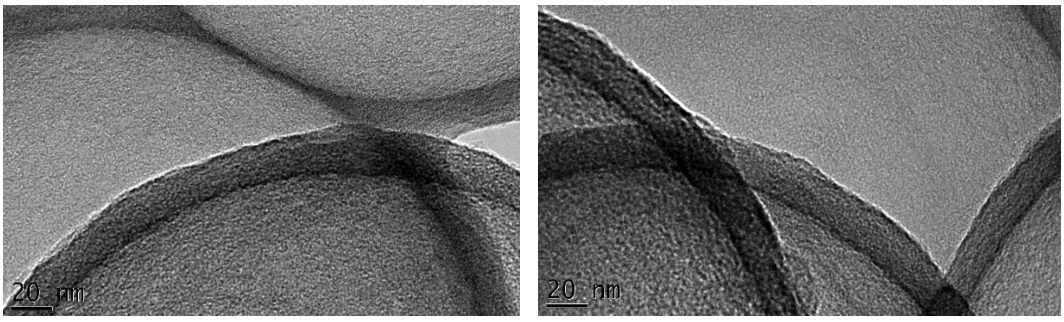

Figure 5.25: TEM images of DRF01 (doped RF01) showing similar structure and shell thickness to RF01

The TEM images confirmed that the RF HCNS were hollow, and the silica template was successfully removed. No major difference could be seen between RF01 and nitrogen doped DRF01.

From the TEM images of RF02 in Figure 5.24 it was confirmed that the large impurities were solid and composed of carbon. The HCNS shells were also thicker in the RF02 sample. The RF02 HCNSs seemed to have a porous structure from the TEM images. Since this feature was not initially seen in the SEM images in Figure

5.21, higher magnification SEM images were taken of this sample presented in Figure 5.26.

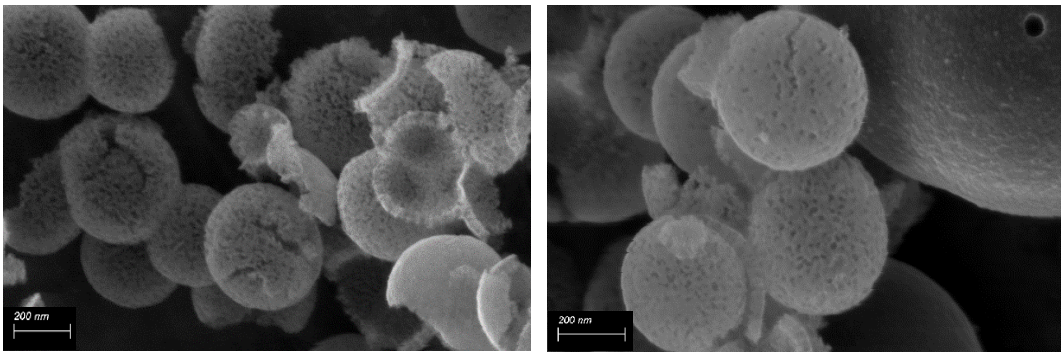

Figure 5.26: High magnification SEM images of RF02 HCNSs showing the porous shell structure (taken after 125 MPa compaction)

From the high magnification images in Figure 5.26 it was confirmed that the RF02 HCNS were indeed porous, unlike the RF01 HCNSs. It was also unknown why the spheres were porous in the RF02 sample compared to the non-porous RF01 sample. It was hypothesised the different volumes of ammonia used in the synthesis method somehow affected the sphere shell porosity and thickness. This would form a topic for a future investigation.

The particle size distributions and shell thicknesses were calculated from the TEM images. The results of the size characteristics for the RF HCNS sample are presented in Table 5.5 with the calculations and additional TEM images in Appendix E.2.1.

Table 5.5: RF HCNS sample characteristics

Sample label	Average shell thickness [nm]	Outer diameter Mean [nm]	Standard deviation (O.D) [nm]
RF01 (whole HCNSs)	19.2	440.6	25.9
RF02 (porous with impurities)	63.1	522.48	58.2
DRF01 (nitrogen doped RF01)	19.1	440.7	25.5

The results in Table 5.5 combined with the TEM and SEM images, showed that the two RF HCNS samples (RF01 and RF02) had different particle size averages, standard deviations, shell thickness, shell porosity and amount of impurities. It would be difficult to draw any relationships from these samples. However, all the RF HCNS samples were still further analysed and compared for structural integrity.

5.4.2. Shell Structure

TGA was performed on the RF HCNS samples. The results are presented in Figure 5.27.

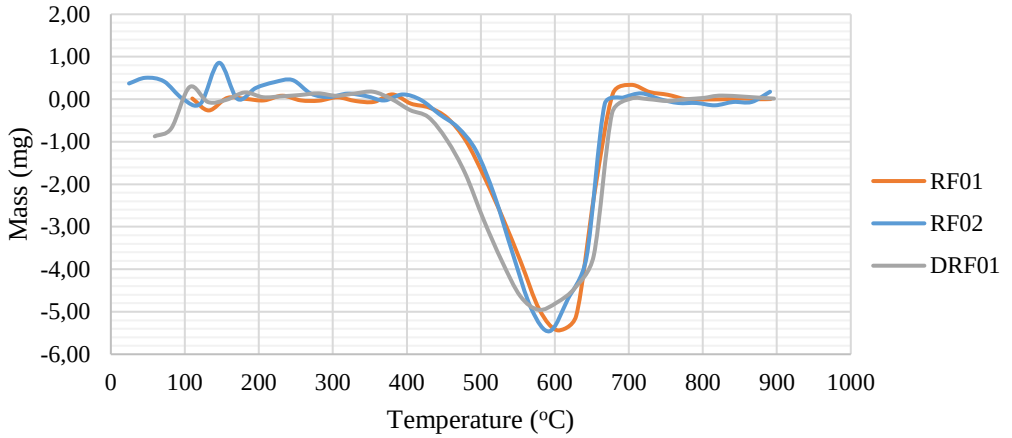

Figure 5.27: TGA results of RF01 (whole spheres), RF02 (porous and impurities) and DRF01 (nitrogen doped RF01)

The DTG results in Figure 5.27 showed that the RF01 (whole spheres) and RF02 (porous HCNS with impurities) have similar carbon compositions. The slight deviation could be a result of the impurities having a larger mass than the HCNSs with a slightly different carbon structure. The trough at approximately 600 °C for the two RF HCNS samples is less than the CVD solid and HCNSs, meaning that the RF method produced carbon shells with a lower degree of graphitisation and oxidative stability.

The DTG results of the nitrogen doped sample, DRF01, showed a wider trough at approximately 590 °C. This slight decrease in graphitisation and oxidative stability with nitrogen-doping of carbon materials is consistent with literature (Xiong, *et al.*, 2014).

All the RF HCNS samples showed residual silica mass from the TGA curve results presented in Appendix C.1. This was consistent with the SEM and EDS results showing small silica particles on the surface on the RF HCNSs.

5.5. Powder Compaction

Powder compaction was performed on the nanospheres according to the procedures in Section 4.7 in order to obtain their compaction curves and Heckel yield pressures. The results were then compared with the sphere characteristics where qualitative relationships between synthesis conditions and structural integrity were determined. This section summarised the important results, supplementary results are presented in Appendix D.

5.5.1. Silica Compaction

Three samples of silica nanospheres were compacted, S200, S300 and S400. Four compaction tests were performed on each sample to determine precision and repeatability of the tests. In each experimental run, the initial compact height and force-vs-displacement data was recorded.

The compaction curve results of the silica nanosphere tests were then calculated and presented in Figure 5.28.

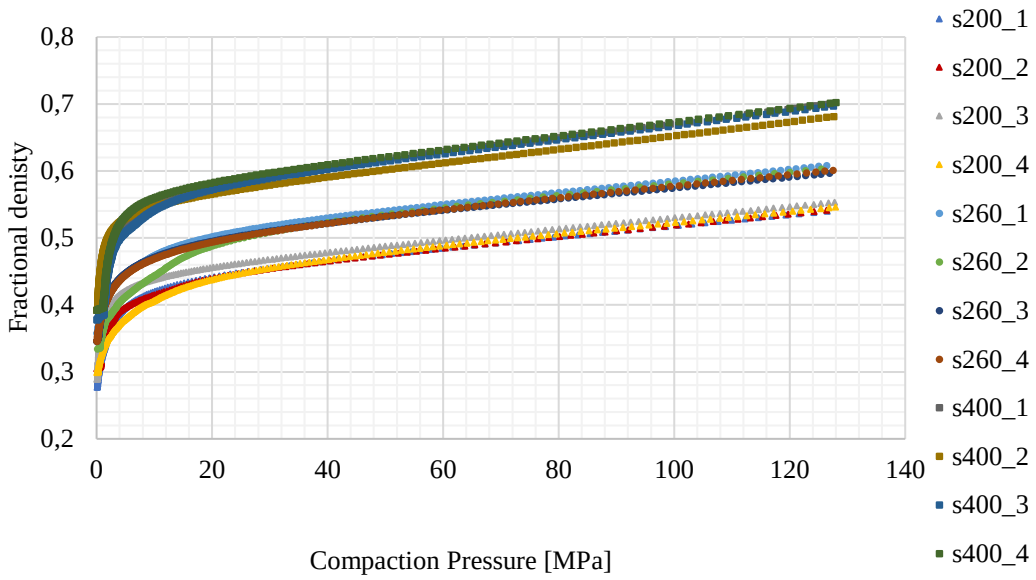

Figure 5.28: Compaction curves of silica nanospheres with varying diameters

From Figure 5.28 it was seen that the silica powders with smaller diameters compacted to less dense compacts at the same compaction pressures. It was hypothesised that this occurred because the smaller spheres were stiffer than the larger spheres. Therefore, the larger spheres deformed elastically to a greater extent during compaction, increasing the fractional density of the compact.

The repeated tests showed visual similarity, this repeatability was then confirmed with statistical methods shown in Section 4.8.2. First, the fractional densities of all the runs were interpolated at 5 MPa compaction pressure increments for direct comparison.

Figure 5.29 presents the interpolated fractional densities, average fractional density and average deviations as error bars at each compaction pressure increment for the S200, S300 and S400 runs, respectively.

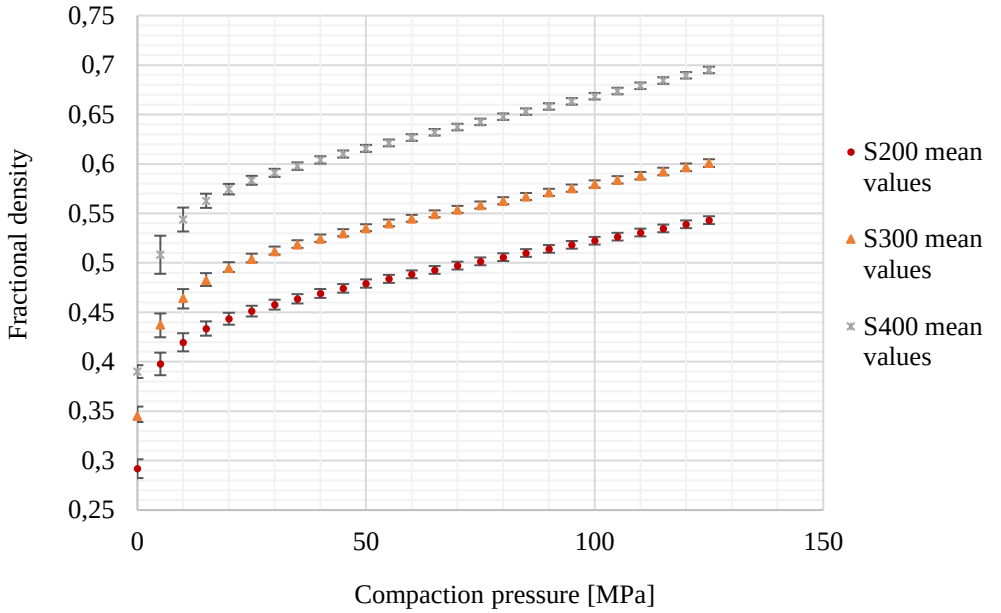

Figure 5.29: Interpolated fractional densities and average deviation at 5 MPa compaction pressure increments for the silica nanosphere compactions.

All three silica nanosphere samples showed large average deviations in the S&R and R&D stages but small deviations in the D stage. The larger deviations were due to the nanosphere powders initially having large static and Van der Waals forces that caused differences in initial apparent density depending on the handling and loading of the powders.

These deviations did not seem to affect the D stage of the compaction. Since the Heckel yield pressure parameters were calculated using the D compaction stage, the larger deviations at the beginning of the powder compaction did not affect these results. Therefore, for the calculation of Heckel yield pressure, the silica nanosphere compaction tests were concluded to be repeatable.

Since the silica nanosphere compaction results for each size sample proved to be repeatable, the Heckel compaction equation was fitted to the silica nanosphere compaction curve and the Heckel yield pressure was calculated following the procedure in Section 4.8.

The Heckel yield pressure results are presented as a function of the mean silica nanosphere diameter in Figure 5.30. The average Heckel yield pressure results are summarised in Table 5.6. The experimental data and Heckel fitting curves are presented in Appendix D.1.

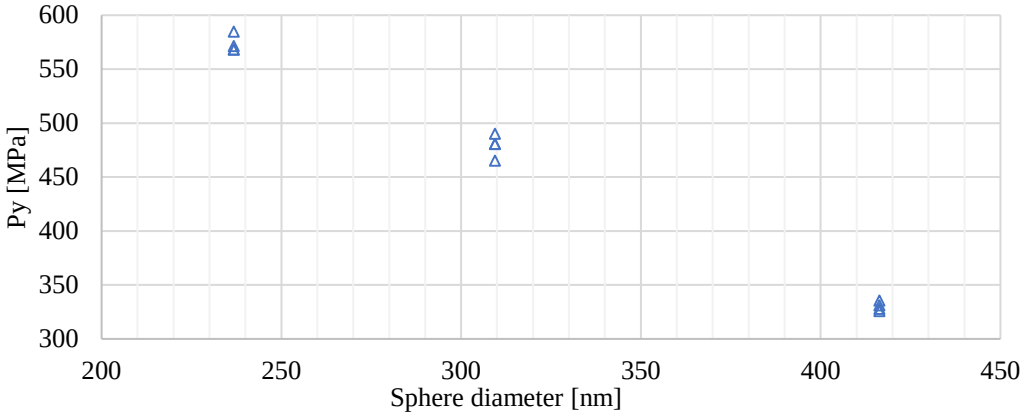

Figure 5.30: Heckel yield pressure as a function of the mean silica nanosphere diameter

Table 5.6: Average Heckel yield pressures for the silica nanospheres.

Sample	Mean sphere diameter [nm]	Heckel yield pressure [MPa]
S200_average	236.75	573.15
S300_average	309.46	479.22
S400_average	416.32	330.08

From Figure 5.30 and Table 5.6 it is seen that the Heckel yield pressures of the silica nanospheres showed a clear relationship of increasing with decreasing diameter.

These size dependent relationships have been found for Young's modulus for polystyrene nanospheres (Guo, *et al*., 2014), and amorphous HCNSs (Yang, et al., 2016). Additionally, proportional correlations have been found between Young's modulus and Heckel yield pressure (Roberts & Rowe, 1987). Therefore, it follows through this proportionality that these results are consistent with literature.

It was therefore concluded that the powder compaction followed by Heckel equation fitting provided a good qualitative comparison for the structural integrity of silica nanospheres.

SEM images were taken of the S400 sample after compaction to 125 and 300 MPa, in order to check whether the silica nanospheres fractured or deformed. Figure 5.31 presents the SEM images.

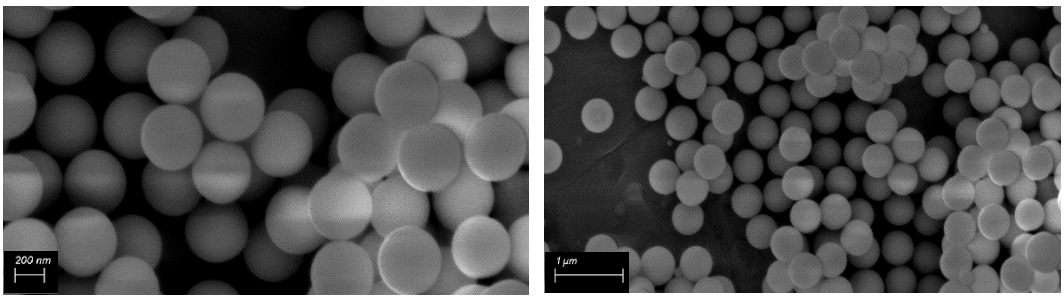

Figure 5.31: SEM images of S400 after 125 MPa compaction (left) and 300 MPa compaction (right)

From Figure 5.31 it was seen that the spheres still appeared spherical in structure and no fragmentation was present. It was concluded that the spheres did not deform plastically to a noticeable amount and most of the deformation was in the elastic region. However, small plastic deformations could have occurred. Additional SEM images are presented in Appendix E.1.

5.5.2. CVD HCNS Compaction

Two samples of CVD HCNSs with varying degrees of carbon coverage were compacted in the punch and die setup. Sample CVD02 was used to represent partial spheres and sample CVD03 to represent sphere flakes. These two samples were compared to determine the effect spherical structure had on structural integrity and compaction behaviour of HCNSs.

Both samples were synthesised with the S300 silica nanosphere templates. It was decided not to test CVD HCNSs with varying diameter because of the broken structure of the spheres.

Three compactions were performed from each sample. The force-vs-displacement data was then converted into compaction curves for direct comparison. The six compaction curves are presented in Figure 5.32.

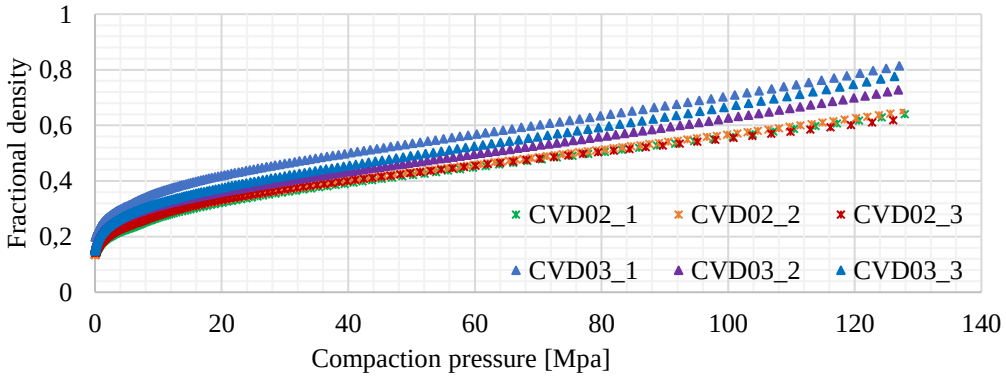

Figure 5.32: Compaction curves of CVD02 (partial spheres) and CVD03 (sphere flakes), demonstrating the effect spherical structure had on compaction behaviour

From Figure 5.32 it was seen that the partial spheres, CVD02 showed better repeatability between tests than the sphere flakes, CVD03. This could be a result of the sphere flakes, CVD03 not having uniform consistency between the samples. It

was then hypothesised that the non-uniform nature of the sample would reduce the accuracy of the bulk compaction testing.

The Heckel compaction equation was then fitted to the CVD HCNS compaction curves. The Heckel parameters were then determined from the linear fitting equation and the parameters were then used to calculate the Heckel yield pressure for each test. The Heckel yield pressure results are presented in Figure 5.33 and summarised in Table 5.7.

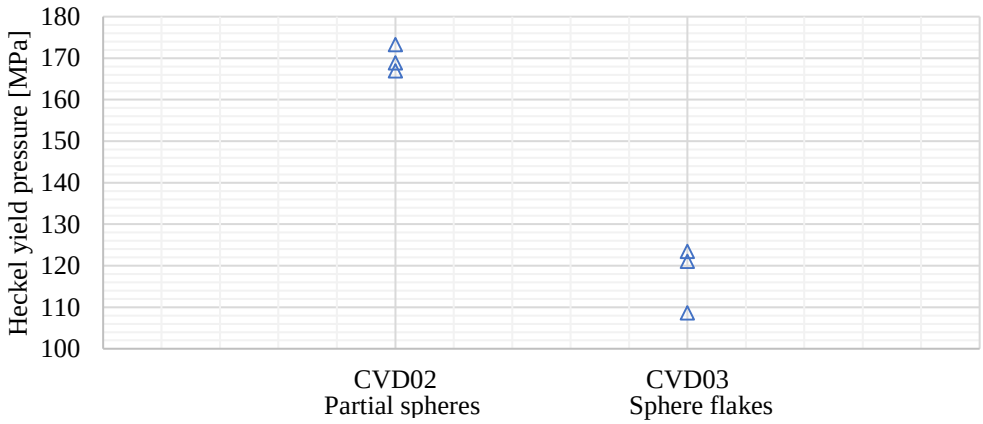

Figure 5.33: Heckel yield pressure scatter plot for the two CVD HCNS samples with varying degrees of carbon coverage

Table 5.7: CVD HCNS Heckel yield pressure summary

Sample	Average Heckel yield pressure [MPa]
CVD02_average (partial spheres)	169.73
CVD03_average (sphere flakes)	117.74

From Figure 5.33 and Table 5.7 it was seen that the sphere flakes sample had on average a smaller Heckel yield pressure than the partial spheres. It was then concluded that, as expected, the very broken or sphere flakes of CVD HCNSs were qualitatively weaker than the slightly broken CVD HCNSs when exposed to compressive stresses. The Heckel yield pressure also showed a decrease with the decrease in structural integrity of the CVD HCNS samples.

5.5.3. CVD Solid Carbon Sphere Compaction

One sample of CVD synthesised solid carbon spheres, SCS01, was compacted in the punch and die setup. Three tests were performed on the sample under the same conditions. The force-vs-displacement data was then converted into compaction curves for direct comparison. The compaction curves are presented in Figure 5.34.

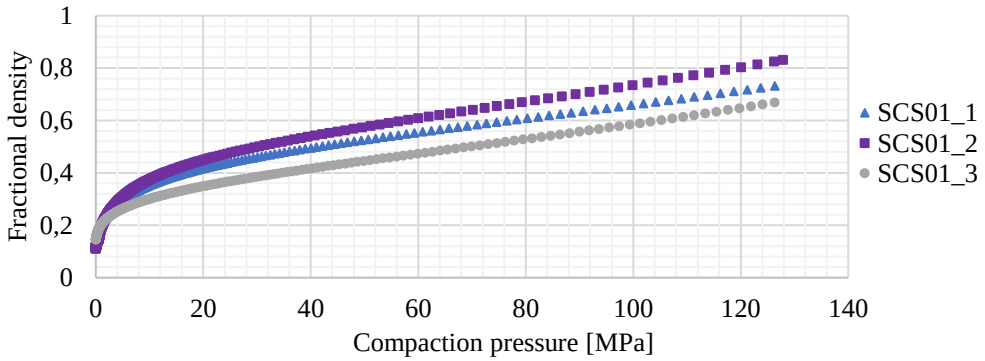

Figure 5.34: Compaction curves of SCS01 showing that the multiple tests did not show repeatability.

From Figure 5.34 it was seen that the three tests on the sample of SCS01 did not show repeatability. This was the same outcome of the CVD sphere flakes, CVD03. This behaviour was most likely a result of the wide size distribution and non-uniform particle structure of the CVD solid carbon spheres.

The Heckel yield pressures were calculated for each test, presented in Table 5.8.

Table 5.8: Heckel yield pressures for SCS01 solid carbon spheres

Test	Heckel yield pressure [MPa]
SCS01_1	135.87
SCS01_2	100.60
SCS01_3	167.79

The Heckel yield pressure results in Table 5.8 showed larger deviations from each other, as expected from the compaction curve results in Figure 5.34. The Heckel yield pressure values were also all lower than that of the CVD HCNSs.

SEM images were taken after compaction where it was noted that the sample appeared to be visually the same as before it was compressed. These SEM images are presented in Appendix E.1. It was hypothesised that the spheres only deformed elastically during compaction and did not fracture, returning to their original size after the load was removed.

It was concluded that if a sample contained these CVD solid carbon spheres then the powder compaction results would be negatively affected and not be repeatable.

5.5.4. RF HCNS Compaction

Three samples of RF HCNSs were compacted in the die and press setup, RF01 which did not contain impurities, RF02 which contained porous shells many large solid carbon impurities and DRF01 which was doped with nitrogen.

Two tests were performed on each sample under the same conditions. The force-vs-displacement data was then converted into compaction curves for direct comparison. The compaction curves are presented in Figure 5.35.

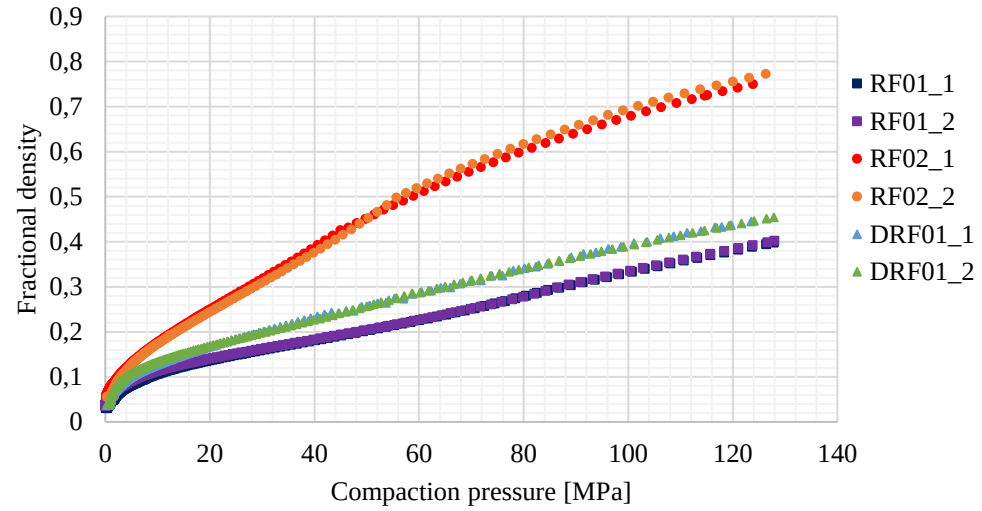

Figure 5.35: Compaction curves of RF HCHSs with each sample showing repeatability

The compaction curves showed good visual repeatability between the samples. The Heckel compaction equation was then fitted to the RF HCNS compaction curves. The Heckel yield pressure results are presented in Figure 5.36 and summarised in Table 5.9.

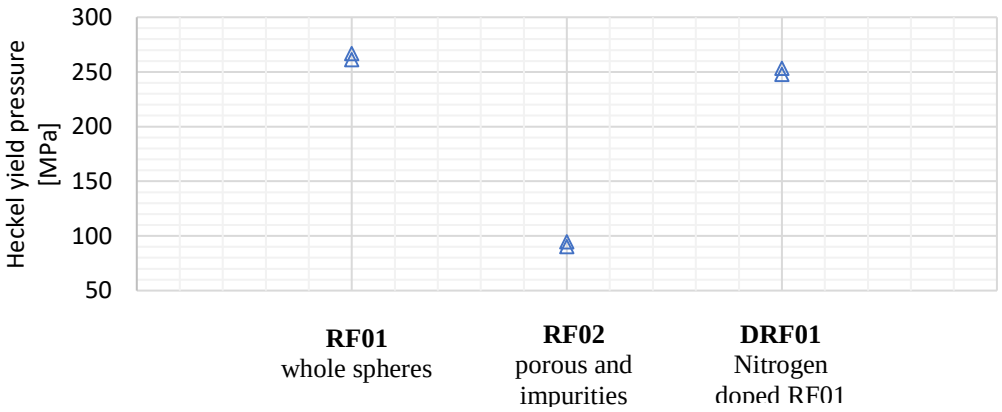

Figure 5.36: Heckel yield pressures for RF HCNS

Table 5.9: Heckel yield pressure summary for RF HCNSs

Sample	Heckel yield pressure [MPa]
RF01_average (whole spheres)	263.88
RF02_average (porous and impurities)	92.26
DRF01_average (N_2 doped RF01)	250.34

From the results in Figure 5.36 and Table 5.9 it was seen that the RF sample with impurities resulted in the combined particles having a smaller Heckel yield pressure. However, the tests still showed repeatability, unlike the solid CVD

spheres. It was also seen that doping the RF HCNSs decreased the Heckel yield pressure of the particles, but only to a slight degree.

The RF HCNSs without impurities proved to be qualitatively stronger than the CVD HCNSs under compressive forces. This was hypothesised to be because of the whole, unbroken spherical structure of the RF HCNSs. To investigate this, a sample of RF01 was crushed with a pestle and mortar to break up the spheres. This sample was then characterised with SEM images, presented in Figure 5.37.

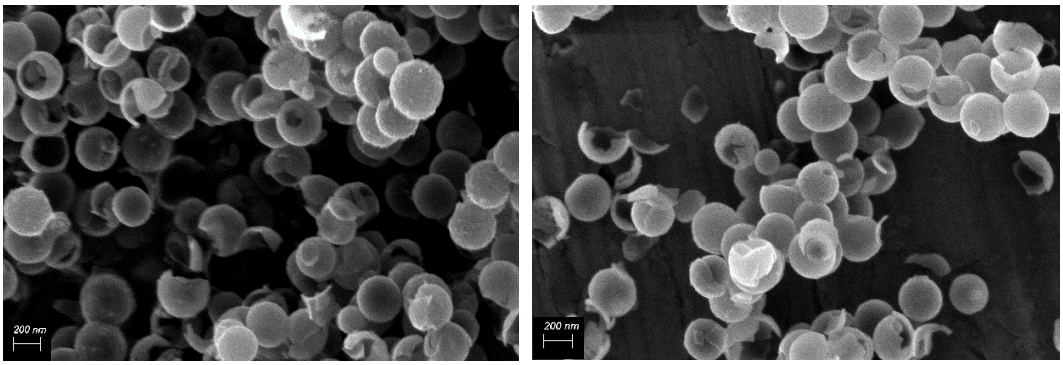

Figure 5.37: SEM images of crushed RF HCNSs

The crushed RF HCNS sample, CRF01 was then compacted, fitted to the Heckel equation and the Heckel yield pressure was calculated. All the RF HCNS Heckel yield pressures are presented in Figure 5.38.

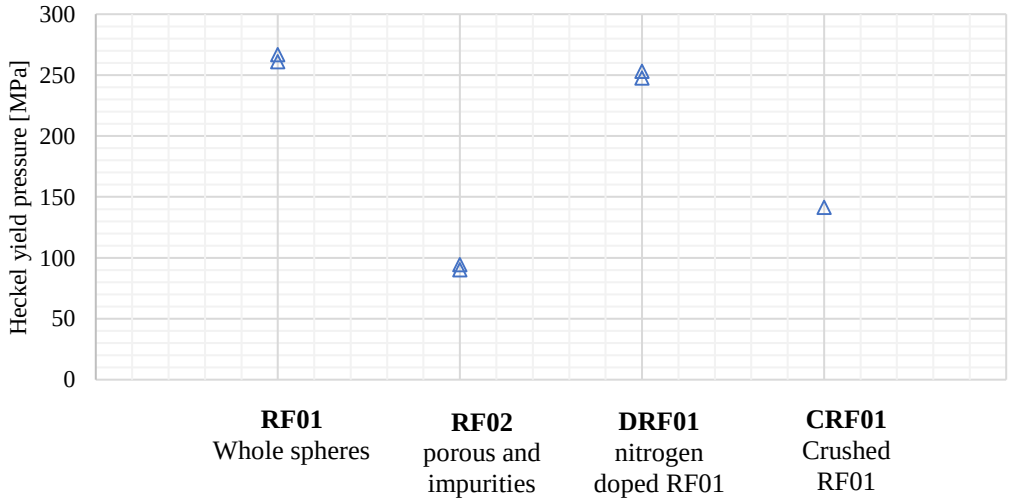

Figure 5.38: RF HCNS Heckel yield pressure results

As seen in Figure 5.38 the RF01 sample had the largest Heckel yield pressure. This was expected since it was the only sample that contained whole spheres with no impurities. Sample DRF01, which consisted of RF01 spheres doped with nitrogen showed a slight decrease in Heckel yield pressure as a result of the doping. Since this Heckel yield pressure difference is small, it cannot be concluded that doping the RF HCNSs affects the sphere's structural integrity without further individual

testing. However, initial results show that doping the spheres with nitrogen does not seem to affect the structural integrity to a large degree.

The Heckel yield pressure of the RF HCNS sample that consisted of porous shells and contained impurities, RF02, was considerably lower than the other RF HCNS samples. This could be a result of the porous shell being structurally weaker than the non-porous shells in RF01, or the presence of the large solid impurities. The result could also be a combination of both of these factors. It was therefore concluded that the Heckel yield pressure result for the RF02 sample could not be used to determine the structural integrity because of the non-uniformity of the sample.

The Heckel yield pressure of the crushed RF01 spheres, CRF01, was considerably smaller than the whole RF01 spheres. This result showed that the Heckel yield pressure decreased with the decrease in structural integrity of the RF HCNSs.

In order to better understand how and when the HCNSs broke during compaction, SEM images were taken after compaction of the RF01 and RF02 samples, presented in Figure 5.39. These two samples were chosen since they were the only samples that contained whole HCNSs that were not initially broken.

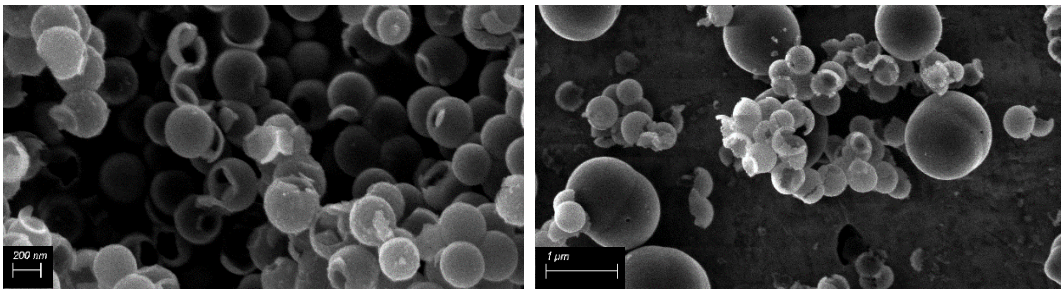

Figure 5.39: SEM images taken after compaction of RF01 (left) and RF02 (right)

From the SEM image of RF01 after compaction in Figure 5.39 it was seen that the smaller porous HCNSs fractured but the larger solid carbon impurities stayed intact. This could be explained by the large solid carbon impurities only deforming by elastic deformation during compaction. The HCNSs most likely deformed by elastic deformation followed by fracture. It was concluded that the larger solid spheres had a relatively smaller Young's modulus than the smaller spheres. This could influence the compaction equation fitting results.

From the SEM images taken after compaction in Figure 5.39, it was also seen that not all of the RF HCNSs were broken. To further investigate this, SEM images were taken at different compaction pressures along the compaction curve. Figure 5.40 presents the compaction curve of RF01_1 with the denoted SEM images in Figure 5.41.

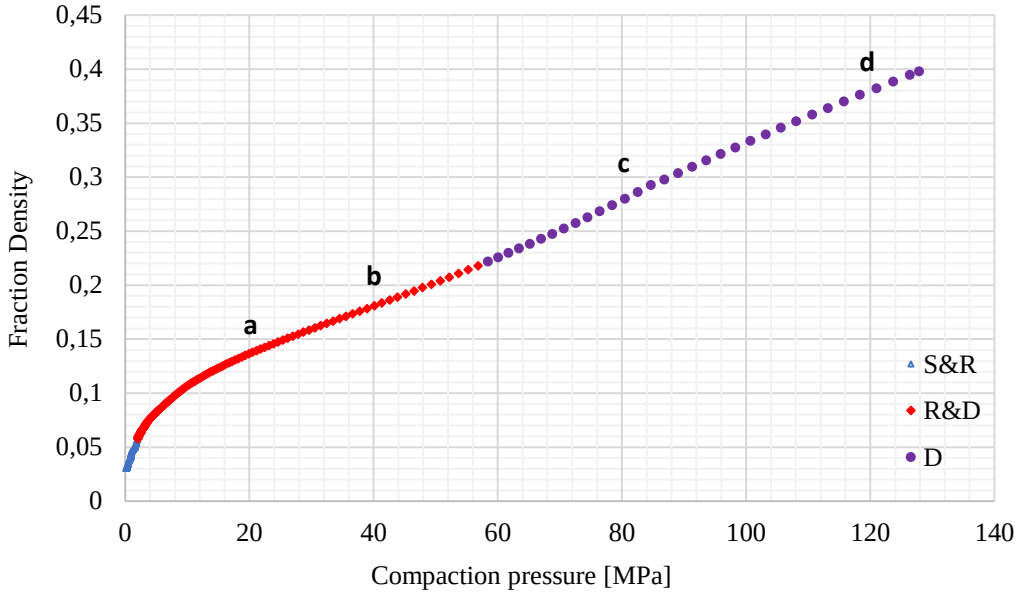

Figure 5.40: RF01_1 compaction curve with denoted pressures where SEM images were taken as presented in Figure 5.41.

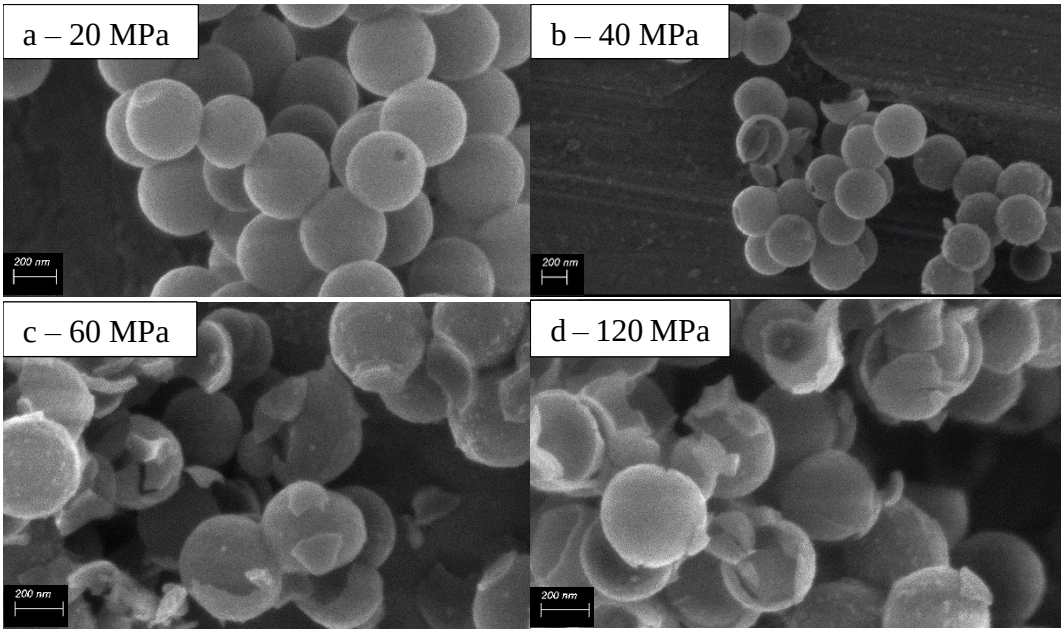

Figure 5.41: SEM images taken at various compaction pressures in Figure 5.40.

From the SEM images in Figure 5.41 and additional images in Appendix E.2.2., it was seen that the spheres started breaking at compaction pressures just before 40 MPa. The number of broken spheres then increased sharply with increasing compaction pressures until approximately 80 MPa where the number of broken spheres remained relatively constant.

The larger hollow spheres in the sample seemed to fracture before the smaller spheres; this was consistent with the smaller silica nanospheres having a larger Heckel yield pressure than the larger silica nanospheres. Compaction experiments of RF HCNS with varying sizes would further investigate this size dependent behaviour. This forms part of the investigation's future recommendations.

5.5.5. Heckel Yield Pressure Comparisons

In summary, seven samples of carbon nanosphere powders were compacted and fitted to the Heckel equation where the Heckel yield pressure was calculated. The Heckel yield pressures for these samples are presented in Figure 5.42

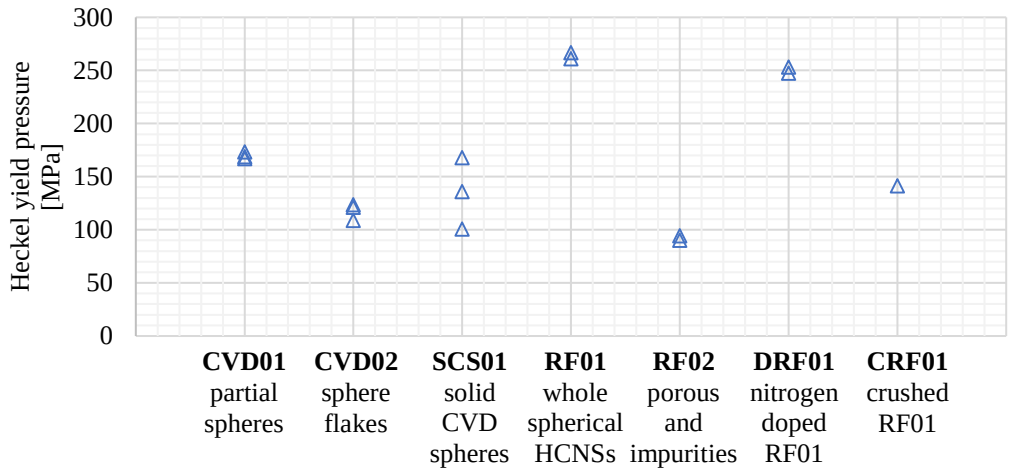

Figure 5.42: Heckel yield pressure comparisons of all carbon spheres

The Heckel yield pressure results in Figure 5.42 provided qualitative comparisons for the structural integrity of the carbon HCNSs. The following conclusions comparing the synthesis factors were made:

- The whole RF HCNSs possessed better structural integrity than the CVD HCNSs with the exception of the RF02 sample that included porous shells and impurities.
- The RF02 sample with impurities showed a considerably smaller Heckel yield pressure than the whole RF01 HCNSs and crushed CRF01 HCNSs. This could be a result of the presence of larger solid impurities detrimentally affecting the Heckel fitting, like the CVD solid spheres. However, it could result from a combination of the impurities, porous structure, larger diameter average and wide particle size distribution. The Heckel yield pressure of the RF02 sample was similar to the CVD sphere flakes and solid carbon spheres. However, it was concluded that the Heckel yield pressure result for the RF02 sample could not be used to determine the structural integrity owing to the non-uniformity of the sample.
- The crushed RF HCNSs closely approximated the broken CVD HCNSs in terms of Heckel yield pressure. This showed that the broken spheres had poor structural integrity regardless of the synthesis method used.

As expected, the spherical structure of the HCNSs played a large role in the spheres structural integrity. The RF synthesising method produced whole unbroken HCNSs while the CVD method produced broken partial spheres. The broken partial spheres resulted in poor structural integrity, as confirmed with characterisation and the Heckel yield pressure determination from the bulk powder compaction testing method.

6. Conclusions and Recommendations

This section summarises the conclusions and future recommendations that stemmed from the results of this investigation.

6.1. Conclusions

HCNSs can be used in various applications where the requirement is for the shell structure to stay intact. Therefore, the structural integrity of these spheres is of importance and was the main motivation behind this investigation. In evaluating the structural integrity of HCNSs, synthesised under different conditions, important relationships were identified. The Heckel yield pressure provided a good qualitative comparison for the structural integrity of the nanospheres. The conclusions of this investigation were separated according to the two main objectives.

6.1.1. Objective 1: To Synthesise HCNSs under Different Conditions and Characterise the Products

Three samples of silica nanosphere templates were synthesised: S200, S300 and S400, representing their approximate diameters in nanometres. The samples were characterised with SEM where the spherical shape and smooth surface was confirmed, and the PSD was determined.

Ten samples of HCNSs were then synthesised using the CVD method to coat the silica nanosphere templates. These samples were synthesised and characterised with SEM, TEM and TGA where the following relationships were concluded:

- The argon flow rate affects the carbon coverage of the HCNSs with the best flow rate of 150 mL/min only producing partial spheres.
- Increasing the toluene temperature to 75 ^{o}C does not improve the carbon coverage of the HCNSs but rather produces lumpy flakes and agglomerated spheres.
- Decreasing the mass of silica nanospheres increases the carbon coverage of the HCNSs, but the yield rate is too low for practical purposes.
- At best, the CVD synthesis method produces only partial spheres.
- The synthesis variables had large effects on the sphere shell structure and could not be optimised independently.

Two samples of HCNSs synthesised using the RF method were characterised for comparison to the CVD method. The following points were concluded:

- The RF method produces spheres than are not broken and are completely covered in a smooth carbon shell. As such, the RF method is a better synthesis method than the CVD methods for producing HCNSs.
- The RF method for synthesising HCNSs is very sensitive to synthesis conditions, such as the amount of ammonia used.
- No major structural integrity differences, apart from a slight decrease in oxidative stability, was observed for nitrogen-doped HCNSs.

6.1.2. Objective 2: To Develop a Bulk Powder Testing Method Capable of Evaluating the Structural Integrity of Nanospheres.

The three silica nanosphere samples were compacted in a punch and die setup on a 30 kN load frame MTS universal testing machine, where the punch force was recorded as a function of displacement. The powder compaction data was then fitted to the Heckel equation where the Heckel yield pressure was calculated for each test.

The Heckel yield pressure results for the silica nanospheres showed a clear decrease with increasing sphere diameter. These size dependent relationships had been found for Young's modulus for polystyrene nanospheres and amorphous HCNSs in literature. Additionally, proportional correlations are reported between Young's modulus and Heckel yield pressure in literature. It was therefore hypothesised that Heckel yield pressure parameter provided a good qualitative comparison for the structural integrity of the nanospheres.

Two CVD HCNS samples were compacted, CVD02 (partial spheres) and CVD03 (sphere flakes). The Heckel yield pressure results showed that the partial spheres had a higher Heckel yield pressure and repeatability than the sphere flakes, which had a lower Heckel yield pressure. The tests results showed variability due to the non-uniform nature of the broken flakes. It was concluded that the partial spheres had a better structural integrity than the sphere flakes, as well as hypothesising that non-uniform samples could not be accurately tested with the developed bulk compaction test.

Three RF HCNS samples were compacted, RF01 (whole, non-porous HCNSs), RF02 (porous HCNSs with impurities) and DRF01 (nitrogen doped RF01 HCNSs). The Heckel yield pressure results showed the whole, non-porous HCNSs had the highest yield pressure of all the HCNSs, including the CVD partial spheres. This was concluded to be a result of the whole spherical structure, confirmed by crushing the RF01 HCNSs and performing the compaction test thereafter. This resulted in a much lower Heckel yield pressure.

The nitrogen doped RF HCNSs showed a slight decrease in Heckel yield pressure. However, individual nanosphere testing methods are recommended in order to validate this result.

The RF02 (porous HCNSs with impurities) sample resulted in a different shaped compaction curve when compared to the other RF HCNS samples, as well as a lower Heckel yield pressure. However, it was concluded that the Heckel yield pressure result for the RF02 sample could not be used to determine the structural integrity because of the non-uniformity of the sample.

In conclusion, the bulk powder compaction test followed by Heckel yield pressure calculation provided a good qualitative parameter to compare different samples of nanospheres. The Heckel yield pressure showed a clear increase with decreasing diameter for silica nanospheres and a clear decrease with decreasing structural integrity for HCNSs.

6.2. Future Recommendations

The future recommendations of this investigation were separated according to the two main objectives.

6.2.1. Objective 1: To Synthesise HCNSs under Different Conditions and Characterise the Products

For the CVD synthesis of HCNSs, the argon flow rate, toluene temperature and silica nanosphere template mass was varied. However, none of the synthesis procedures produced whole HCNSs. It was concluded that the synthesis factors were dependent on each other and could not be optimised separately. A future recommendation would be to investigate the factors of CVD synthesis and optimise these to produce large amounts of whole, fully covered and smooth HCNSs.

Two RF HCNS samples were produced and provided by the CoE-SM through the University of the Witwatersrand. One sample consisted of whole, smooth, fully covered HCNS with no impurities while the other sample consisted of porous shells, a wider size distribution and large solid impurities. It was unclear what caused these variations which could be investigated in future research.

6.2.2. Objective 2: To Develop a Bulk Powder Testing Method Capable of Evaluating the Structural Integrity of Nanospheres.

The size effect of silica nanospheres on the Heckel yield pressure, and therefore structural integrity was determined by compacting three powders with different diameters. It was hypothesised that the same effect would be seen with HCNSs. In order to test this hypothesis, RF HCNS samples with different diameters should be synthesised and tested.

The Heckel yield pressure results gave a qualitative comparison for the nanosphere powder's structural integrity. It is recommended for future research, to test the nanospheres individually so as to have a direct comparison between the Heckel yield pressure and individual sphere material properties. This could be achieved through AFM compression or in-situ TEM nanoindentation.

A further future recommendation would be to test the affect sphere shell thickness has n HCNS structural integrity. This recommendation ties in with further research into various HCNS synthesis methods.

7. References

CAF Stellenbosch Univeristy, 2017. *FEG-SEM,* Stellenbosch: CAF Stellenbosch Univeristy.

Denny, P. J., 2002. Compaction equations: a comparison of the Heckel and Kawakita equations. *Powder Technology,* Volume 127, pp. 162-172.

Deshmukh, A. A., Mhlanga, S. D. & Coville, N. J., 2010. Carbon spheres. *Materials Science and Engineering R,* Volume 70, pp. 1-28.

Dlamini, M., 2016. Spherical carbons as model supports for Fe, Co and Fe-Co Fischer-Tropsch catalysts. *Unpublished PhD dissertation* .

Fuertes, A., Valled-Vignon, P. & Sevilla, M., 2012. One-step synthesis of silica@resorcinol–formaldehyde spheres and their application for the fabrication of polymer and carbon capsules. *Chemistry Communniation,* Volume 48, pp. 6124-6126.

German, R. M., 2005. *Powder Metallurgy & Particulate Materials Processing.* New Jersey: MPIF.

Green, D. et al., 2003. Size, volume fraction, and nucleation of Stober silica nanoparticles. *Journal of Colloid and Interface Science,* Volume 266, pp. 346-358.

Guo, D. et al., 2014. Elastic Properties of Polystyrene Nanospheres Evaluated with Atomic Force Microscopy: Size Effect and Error Analysis. *Langmuir,* Volume 30, pp. 7206 - 7212.

Huang, Q. et al., 2016. Hollow Carbon Nanospheres with Extremely Small Size as Anode Material in Lithium-Ion Batteries with Outstanding Cycling Stability. *The Journal of Physical Chemistry,* Volume 120, pp. 3139-3144.

Ibrahim, I. A., Zikry, A. & Sharaf, M. A., 2010. Preparation of spherical silica nanoparticles: Stober silica. *Jornal of American Science,* 6(11), pp. 985-989.

Kaufmann, E. N., 2003. *Characterization of Materials.* 1 ed. Canada: John Wiley & Sons.

Khlebtsov, B. & Khlebtsov, N., 2011. On the Measurement of Gold Nanoparticle Sizes by the Dynamic Light Scattering Method. *Colloid Journal,* Volume 73, pp. 118-127.

Li, S., Pasc, A., Fierro, V. & Celzard, A., 2016. Hollow carbon spheres, synthesis and applications – a review. *Journal of Materials Chemistry A,* Volume 4, pp. 12686-12713.

Liu, C. et al., 2015. Controllable Synthesis of Functional Hollow Carbon Nanostructures with Dopamine As Precursor for Supercapacitors. *Applied Materials and Interfaces,* Volume 7, pp. 18609-18617.

Liu, J. et al., 2011. Extension of The Stober Method to the Preparation of Monodisperse Resorcinol–Formaldehyde Resin Polymer and Carbon Spheres. *Angewandte Chemie*, Volume 50, pp. 5947-5951.

Malvern, 2011. *Malvern Intruments.* [Online]
Available at: http://www.biophysics.bioc.cam.ac.uk/wp-content/uploads/2011/02/DLS_Terms_defined_Malvern.pdf
[Accessed 13 February 2017].

McKee, G. S. B. & Vecchio, K. S., 2006. Thermogravimetric Analysis of Synthesis Variation Effects on CVD Generated Multiwalled Carbon Nanotubes. *Journal of Physical Chemistry B*, Volume 110, pp. 1179-1186.

Mutuma, B., 2016. Correspondence. September, Johannesburg.

Mutuma, B. K. et al., 2016. Generation of open-ended, worm-like and graphene-like structures from layered spherical carbon materials. *Royal Society of Chemistry*, Volume 6, pp. 20399-20408.

Mutuma, B. et al., 2017. Hollow carbon spheres and a hollow carbonsphere polyvinylpyrrolidone composite ammonia sensors. *Jornal of Materials Chemistry A*, Volume 5, pp. 2539-2549.

Nongwe, I. et al., 2014. Synthesis of gold encapsulated in spherical carbon capsules with a mesoporous shell structure. A robust catalyst in a nanoreactormesoporous shell structure. A robust catalyst in a nanoreactor. *Catalysis Communications*, Volume 53, pp. 77-82.

Nongwe, I., Ravat, V., Meijboom, R. & Coville, N., 2013. Efficient and reusable Co/nitrogen doped hollow carbon spherecatalysts for the aerobic oxidation of styrene. *Applied Catalysis A: General*, Volume 466, pp. 1-8.

Parnell, S. et al., 2016. Porosity of silica Stöber particles determined by spin-echo small angle neutron scattering. *Royal society of chemistry*, Volume 12, pp. 4709-4714.

Phaahlamohlaka, T., Kumi, D. D. M. & Jewell, L. C. N., 2016. Ruthenium nanoparticles encapsulated inside porous hollow carbonspheres: A novel catalyst for Fischer–Tropsch synthesis. *Catalysis today*, Volume 275, pp. 76-83.

Phaahlamohlaka, T. N. et al., 2017. Effects of Co and Ru Intimacy in Fischer−Tropsch Catalysts Using Hollow Carbon Sphere Supports: Assessment of the Hydrogen. *ACS Catalysis*, Volume 7, pp. 1568-1578.

Poco Graphtie, 2015. *Properties and characteristics of Graphite.* [Online]
Available at: http://poco.com/Portals/0/Literature/Semiconductor/IND-109441-0115.pdf
[Accessed 23 February 2016].

Roberts, R. & Rowe, R., 1987. The compaction of pharmaceutical and other model materials - a pragmatic approach. *Chemical Engineering Science,* 42(4), pp. 903-911.

Su, F. et al., 2006. Hollow carbon spheres with a controllable shell structure. *Journal of Materials Chemistry,* Volume 16, pp. 4413-4419.

Tiwari, S. K. et al., 2016. Magical Allotropes of Carbon: Prospects and Applications. *Critical reviews in Solid State and Materials Science,* 41(4), pp. 257-317.

University of California, Irvine, 2013. *Analysis of Errors.* [Online] Available at: http://faculty.sites.uci.edu/chem1l/files/2013/11/RDGerroranal.pdf [Accessed 5 11 2016].

van Wijk, J. et al., 2013. Poly(methyl methacrylate)–silica microcapsules synthesized by templating Pickering emulsion droplets. *Journal of Materials Chemistry B,* Volume 1, pp. 2394-2406.

Xiong, h., Motchelah, M., moyo, M. & Jewell, L., 2014. Fischer–Tropsch synthesis: Iron-based catalysts supported on nitrogen-doped carbon nanotubes synthesized by post-doping. *Applied Catalysis A: General,* Volume 482, pp. 377-386.

Xu, H., Guo, J. & Suslick, K. S., 2012. Porous Carbon Spheres from Energetic Carbon Precursors using Ultrasonic Spray Pyrolysis. *Advanced Materials,* Volume 24, pp. 6028-6033.

Yang, W. et al., 2016. Large-deformation and highstrength amorphous porous carbon nanospheres. *Nature,* Volume 6, pp. 1-9.

Yoshizawa, N. et al., 2006. TEM and electron tomography studies of carbon nanospheres for lithium secondary batteries. *Carbon,* Volume 44, pp. 2558-2564.

Yuan, D., Chen, J., Zeng, J. & Tan, S., 2008. Preparation of monodisperse carbon nanospheres for electrochemical capacitors. *Electrochemsitry communications,* Volume 10, pp. 1067-1070.

Zhang, C. et al., 2014. Hollow graphitic carbon nanospheres: synthesis and properties. *Journal of Material Science,* Volume 49, pp. 1947-1956.

Appendix A: Experimental Apparatus and Step-By-Step Procedures

A.1. Silica Nanosphere Synthesis

Three samples of silica nanospheres were synthesised for this investigation. The apparatus and chemicals used are summarised in Table A.1.

Table A.1 Silica synthesis apparatus and chemicals

Equipment	Laboratory supplies	Chemicals
• Magnetic stirrer and stirrer beads • Centrifuge • Drying furnace • Fume hood	• Glass beakers, 500 mL • Glass measuring cylinders, 10 mL and 100 mL • Pipettes • Stainless steel spatula • 50 mL polypropylene (PP) centrifuge tubes • Parafilm • Pestle and mortar	• TEOS, 98 % RG • Ethanol, 99.9 % AR • Ethanol, 96 % RG • Ammonia solution, 25 % AR • Water, distilled

The silica synthesis procedure was repeated several times to make multiple samples with three different nanosphere diameters. The volumes of reagents determined the diameter of the silica nanospheres, as summarised in Table A.2.

Table A.2: Reagent volumes for varying silica sizes

Diameter [nm]	Ethanol 99.9 % [mL]	Ethanol 96 % [mL]	Water [mL]	Ammonia solution [mL]	TEOS [mL]
200	160	-	28	4	6
300	-	160	28	4	6
400	180	-	126	10	32

The following step-by-step procedure was performed to synthesise the silica nanosphere samples:

Step 1: Synthesis of colloidal silica nanospheres

- The water and ethanol were measured and poured into the 500 mL beaker in fume hood.
- One stirrer bead was added to the beaker and stirred with a magnetic stirrer at 500 rpm for 5 minutes.
- The ammonium solution was measured and added to the beaker.
- The beaker was covered with parafilm and stirred for 20 minutes.
- TEOS was measured and added quickly to the beaker. The quick addition of TEOS allows for the nucleation of all silica nanospheres to occur

simultaneously, resulting in a small standard deviation in the PSD (Mutuma, *et al.*, 2016).
- The beaker was covered with parafilm and stirred for 2 hours.

Step 2: Separating the solid silica via centrifugation

- The beaker was removed from the stirrer and the solution was decanted into 50 mL centrifuge tubes.
- The solution was centrifuged at 4000 rpm for 20 minutes. There should be a clear separation of the white silica nanospheres and clear liquid.
- The liquid part is discarded and the solid is washed with ethanol three times.

Step 3: Drying and storing the silica nanosphere powder

- The centrifuge tube containing the solid silica was dried in a furnace at 100 ^{o}C for 12 hours.
- The solid silica pellets were ground gently with a pestle and mortar and placed in labelled sample vials.

A.2. Hollow and Solid Carbon Nanosphere Synthesis

The hollow and solid carbon nanospheres were synthesised using the same tube furnace and similar procedures. The apparatus and chemicals used are summarised in Table A.3.

Table A.3: CVD synthesis apparatus

Equipment	Laboratory supplies	Chemicals
• Tube furnace • Quartz tube with fittings • Quartz boat • Glass flow meter	• Glass bubbler with two-way bypass tap • Glass bubbler • Plastic tubing • Silicon grease • Parafilm	• Tap water • Acetone, 99.0 % for cleaning • Toluene, 99.5 % AR

The following step-by-step procedure was performed to synthesise the HCNSs.

Step 1: Setting up the experiment

- The silica nanosphere template powder was weighed and placed into the quartz boat.
- The quartz boat was placed into the centre of the quartz tube, to ensure that the entire boat will be in the hot zone when placed in the tube furnace.
- The quartz tube was then placed in the tube furnace, taking care not to rotate the tube and tip the boat.
- The water and toluene/argon bubblers were filled with tap water and toluene respectively.
- The plastic tubes were connected to the glass fittings.
- The glass fittings were inserted into the quartz tube with silicon grease.

- The argon flow rate was set and connected to the toluene bubbler. The flow rate of the argon was set using a glass volumetric flow meter and needle valve.
- The toluene bubbler tap was turned so that the argon bypassed the toluene liquid.
- All connections were wrapped with parafilm to ensure air-tight seals.

Step 2: Running the furnace

- The tube furnace was heated at a rate of 10 ^{o}C/min until 900 ^{o}C was reached.
- The tap of the toluene bubbler was turned so that the argon bubbled through the toluene liquid.
- The furnace was held at 900 ^{o}C for 4 hours and then turned off.
- The tap of the toluene bubbler was turned so that the argon bypassed the toluene.

Step 3: Removing the sample

- The furnace was allowed to cool to room temperature.
- The glass fittings, quartz tube and quartz boat were removed from the furnace.
- The carbon covered silica was then placed in a labelled sample vial.

Step 4: Cleaning the quartz boat and tube

- The empty quartz boat was placed in the centre of the quartz tube.
- The quartz tube was placed in the tube furnace.
- The tube furnace was heated up at a rate of 10 ^{o}C/min until 800 ^{o}C was reached.
- The furnace was held at 800 ^{o}C for 2 hours and then turned off.
- The furnace was allowed to cool to room temperature.
- The clean quartz tube and boat was removed. Any residual carbon was wiped off with acetone.

The following step-by-step procedure was following in order to synthesise the solid carbon spheres

Step 1: Setting up the experiment

- The empty quartz tube was placed in the tube furnace.
- The plastic tubes were connected to the glass fittings.
- The glass fittings were inserted into the quartz tube with silicon grease.
- The argon flow rate was set and connected to the toluene bubbler. The flow rate of the argon was set using a glass volumetric flow meter and needle valve.
- The toluene bubbler tap was turned so that the argon bypassed the toluene liquid for the whole experiment.
- All connections were wrapped with parafilm to ensure air-tight seals.

Step 2: Running the furnace

- The tube furnace was heated at a rate of 10 ^{o}C/min until 900 ^{o}C was reached.
- The tap of the toluene bubbler was turned so that the argon bubbled through the toluene liquid.

- The furnace was held at 900 ^{o}C for 4 hours and then turned off.

Step 3: Removing the sample

- The furnace was allowed to cool to room temperature.
- The glass fittings and quartz tube were removed from the furnace.
- The quartz tube was tipped and tapped to collect the solid carbon spheres in the hot zone of the tube.

Step 4: Cleaning the quartz boat and tube

- The quartz tube was placed in the tube furnace.
- The tube furnace was heated up at a rate of 10 ^{o}C/min until 800 ^{o}C was reached.
- The furnace was held at 800 ^{o}C for 2 hours and then turned off.
- The furnace was allowed to cool to room temperature.
- The clean quartz tube was removed. Any residual carbon was wiped off with acetone.

A.3. RF HCNSs

Two samples of RF HCNSs were synthesised and provided by the CoE-SM through the University of the Witwatersrand. The apparatus and chemicals used are summarised in Table A.4.

Table A.4: RF synthesis apparatus and chemicals

Equipment	Laboratory supplies	Chemicals
• Tube furnace • Quartz tube with fittings • Teflon lined stainless steel autoclave • Centrifuge • Magnetic stirrer	• Glass beakers • Measuring cylinders • Plastic tubing • Silicon grease • Parafilm	• TEOS • Absolute ethanol • Deionized water • Ammonia, 25% • Resorcinol • Formaldehyde • Nitrogen gas

The reagent volumes for the two samples are summarised in Table A.5.

Table A.5: Reagent summary for RF HCNS synthesis

RF sample	Ethanol 99.9 % [mL]	TEOS [mL]	Water [mL]	Ammonia solution [mL]	Resorcinol [g]	Formaldehyde [mL]
RF01	62.5	2,13	7.5	5	0.5	0.7
RF02	62.5	2.13	7.5	2.5	0.5	0.7

The following step-by-step procedure was performed to synthesise the RF HCNSs.

Step 1: Synthesis of colloidal silica nanospheres

- The water, ethanol and ammonia were measured and poured into the beaker in fume hood.
- One stirrer bead was added to the beaker and stirred with a magnetic stirrer.
- TEOS was measured and added quickly to the beaker.
- The beaker was covered with parafilm and stirred for 1 hour.

Step 2: Addition the resorcinol and formaldehyde

- The resorcinol and formaldehyde were added to the solution to form the core-shell composite.
- The solution was then stirred for 24 hours.

Step 3: Carbonising the resorcinol formaldehyde coating

- The beaker containing the solution was transferred into the autoclave and then heat treated at 100 ^{o}C for 24 hours.
- The solids were then separated from the liquid by centrifugation for 5 minutes.
- The solid part was then dried in a furnace at 70 ^{o}C for 12 hours.
- The powder was then carbonised in a tube furnace similar to the CVD method, for 1 hour at 900 ^{o}C under a nitrogen atmosphere with a flow rate of 20 mL/min.

A.4. HF Treatment

All the coated silica nanospheres were treated in aqueous HF acid in order to remove the template.

The apparatus and chemicals used are summarised in Table A.6.

Table A.6: Silica removal apparatus

Equipment	Laboratory supplies	Chemicals
• Fume hood • Magnetic stirrer • Centrifuge • Drying furnace • Glass flow meter	• PP centrifuge tubes, 50 mL • PP beakers, 100 mL • PP measuring cylinders, 10 mL and 100 mL • PP pipettes • 10 mL and 50 mL plastic measuring cylinder • Stirrer beads	• Distilled water • Hydrofluoric acid, 40 % • Hydrogen borate crystals

The following step-by-step procedure was followed in order to remove the silica template to form HCNSs.

Step 1: HCNS sample prep and experimental setup

- 1 g of HCNS powder was added to a 50 mL PP centrifuge tube.
- A stirrer bead was added to the centrifuge tube placed on a magnetic stirrer in a fume hood.

Step 2: HF treatment

- 30 mL of 10 wt% HF was added to the centrifuge tube and stirred for 12 hours.

Step 3: System neutralisation

- 1 g of hydrogen borate and 15 mL of distilled water was added to the tube and stirred for 5 minutes. The boric acid 'neutralised' the system by bonding the free fluoride ions as fluoroboric acid, reducing the personal handling risk.

Step 4: HCNS separation

- The tubes were centrifuged at 500 rpm for 30 minutes.
- The clear liquid was removed, and the black solids were dried in a furnace at 100 ^{o}C for 12 hours.
- The dry HCNS powder was stored in labelled glass vials.

A.5. Heat Treatment

All the HCNSs were heat treated under inert conditions to remove any residual reagent and surface functional groups. The apparatus and chemicals used are summarised in Table A.7.

Table A.7: Heat treatment apparatus.

Equipment	Laboratory supplies	Chemicals
• Tube furnace • Quartz tube with fittings • Quartz boat	• Plastic tubing • Silicon grease • Parafilm	• Tap water • Acetone, 99.0 % for cleaning

The following step-by-step procedure to heat treat the HCNS was performed:

Step 1: Setting up the experiment

- A sample of HCNSs was loaded into the quartz boat and placed in the centre of the quartz tube.
- The quartz tube was placed in the tube furnace.
- The plastic tubes were connected to the glass fittings.
- The glass fittings were inserted into the quartz tube with silicon grease.
- The argon flow rate was set and connected to the toluene bubbler. The flow rate of the argon was set using a glass volumetric flow meter and needle valve.
- The toluene bubbler tap was turned so that the argon bypassed the toluene liquid for the whole experiment.
- All connections were wrapped with parafilm to ensure air-tight seals.

Step 2: Running the furnace

- The tube furnace was heated at a rate of 10 ^{o}C/min until 800 ^{o}C was reached.
- The furnace was held at 800 ^{o}C for 2 hours and then turned off.

Step 3: Removing the sample

- The furnace was allowed to cool to room temperature.
- The glass fittings and quartz tube were removed from the furnace.
- The quartz boat was removed and the HCNSs were stored in labelled glass vials.

Step 4: Cleaning the quartz boat and tube

- The quartz boat and quartz tube were placed in the tube furnace.
- The tube furnace was heated up at a rate of 10 ^{o}C/min until 800 ^{o}C was reached.
- The furnace was held at 800 ^{o}C for 2 hours and then turned off.
- The furnace was allowed to cool to room temperature.
- The clean quartz boat and tube was removed. Any residual carbon was wiped off with acetone.

A.6. Nitrogen-Doping

A sample of the RF01 HCNSs were doped with nitrogen in a tube furnace. The apparatus and chemicals used are summarised in

Table A.8: Apparatus for nitrogen-doping

Equipment	Laboratory supplies	Chemicals
• Tube furnace • Quartz tube with fittings • Quartz boat	• Glass bubbler with two-way bypass tap • Glass bubbler • Plastic tubing • Silicon grease • Parafilm	• Acetone, 99.0 % for cleaning • Acetonitrile, 99.5 % AR

The following step-by-step procedure to heat treat the HCNS was performed:

Step 1: Setting up the experiment

- A sample of HCNSs was loaded into the quartz boat and placed in the centre of the quartz tube.
- The quartz tube was placed in the tube furnace.
- The plastic tubes were connected to the glass fittings.
- The glass fittings were inserted into the quartz tube with silicon grease.
- The argon flow rate was set and connected to the acetonitrile bubbler. The flow rate of the argon was set using a glass volumetric flow meter and needle valve.
- The toluene bubbler tap was turned so that the argon bypassed the acetonitrile.
- All connections were wrapped with parafilm to ensure air-tight seals.

Step 2: Running the furnace

- The tube furnace was heated at a rate of 10 ^{o}C/min until 750 ^{o}C was reached.
- The acetonitrile bubbler tap was turned so that the argon bubbled through the acetonitrile.

- The furnace was held at 750 ^{o}C for 2 hours and then turned off.
- The acetonitrile bubbler tap was turned so that the argon bypassed the acetonitrile.

Step 3: Removing the sample

- The furnace was allowed to cool to room temperature.
- The glass fittings and quartz tube were removed from the furnace.
- The quartz boat was removed and the HCNSs were stored in labelled glass vials.

Step 4: Cleaning the quartz boat and tube

- The quartz boat and quartz tube were placed in the tube furnace.
- The tube furnace was heated up at a rate of 10 ^{o}C/min until 800 ^{o}C was reached.
- The furnace was held at 800 ^{o}C for 2 hours and then turned off.
- The furnace was allowed to cool to room temperature.
- The clean quartz boat and tube was removed. Any residual carbon was wiped off with acetone.

A.7. Powder Compaction

Powder compaction was performed on the nanospheres to extract qualitative information about their structural integrity. The apparatus used is listed below:

- 30 kN load frame MTS universal testing machine,
- Upper and lower compression stages,
- Die and punch setup with a circular 10 mm diameter punch cross section,
- Digital scale, and
- Weighing paper.

The following procedure was performed for the powder compaction:

Step 1: Preparing sample and experiment setup

- The nanosphere sample was weighed and loaded into the punch and die setup.
- The punch and die setup was tapped until the powder had settled inside the die.
- The top punch was inserted into the die so that it was resting on the surface of the powder compact.
- The initial compact height was measured and recorded.
- The die punch and die setup was placed between the compaction stages of the universal testing machine.

Step 2: Running the powder compaction

- The displacement and force channels were zeroed.
- The crosshead velocity was set to 1um/second and the compression limit to 10 kN.
- The powder was compressed until a compaction pressure of 10 kN.
- The force vs displacement data was then recovered.

The technical drawings of the punch and die tools used are presented in Figure A.1 - Figure A.3

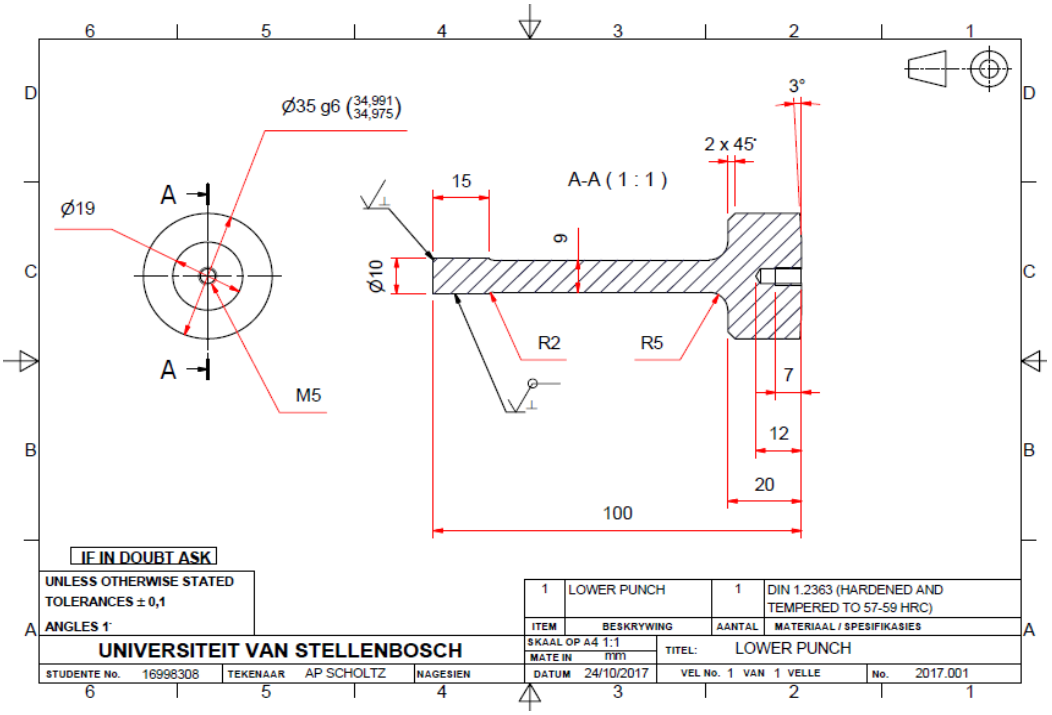

Figure A.1: Lower punch dimensions

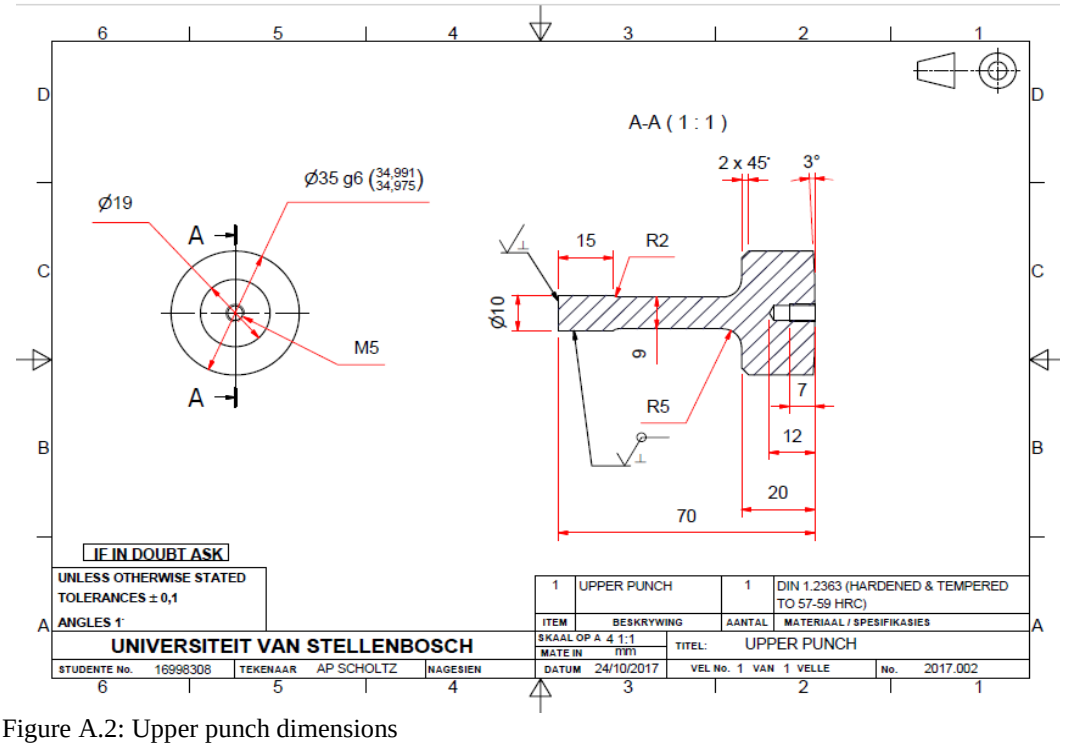

Figure A.2: Upper punch dimensions

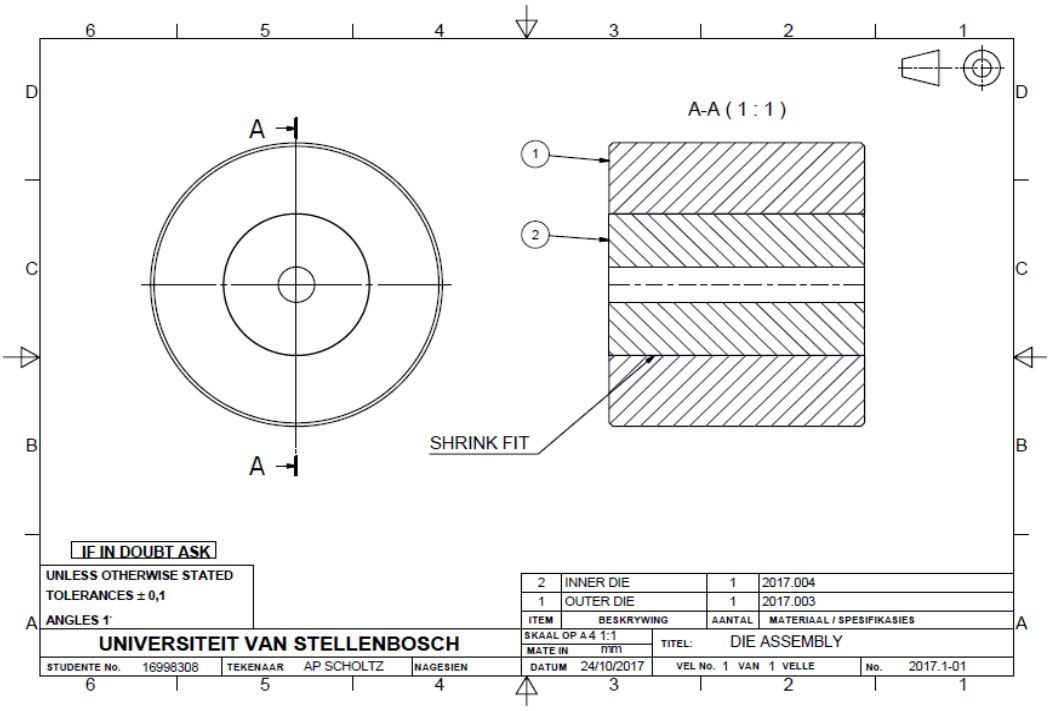

Figure A.3: Die dimensions

Appendix B: Silica PSD Characterisation

B.1. Zetasizer

The results and parameters returned from a DLS analysis are summarised in Table B.1.

Table B.1: Dynamic light scatter analysis results, adapted from (Malvern, 2011)

Parameter	Explanation
Hydrodynamic diameter	Diameter of theoretical sphere will equal diffusion coefficient as measured particle.
Z – average size	Hydrodynamic parameter, known as the cumulants mean. Sensitive to wide size distributions, agglomerates and particle sphericity.
Polydispersity Index	Used to evaluate if the sample is suitable for DLS analysis. A wide size distribution will yield inaccurate results. Should be less than 0.7
Intercept	Used to evaluate signal-to-noise ratio based on the instrument calibration. Should be in the range of 0.6 - 1.
Intensity distribution	PSD that is weighted according to the scattering intensity of a particle size. Sensitive to agglomeration and the presence of larger particles.
Volume distribution	PSD calculated from Intensity distribution using Mie theory. This bases the distribution on the particles mass and volume instead of scattering intensity. Sensitive to agglomeration and the presence of larger particles.
Number distribution	PSD where each individual particle has equal weighting.

The Zetasizer was set to return the number distribution for the silica nanosphere analysis. The results are presented in the subsequent Figures.

		Size (d.nm...	% Intensity:	St Dev (d.n...
Z-Average (d.nm): 300.2	Peak 1:	283.6	100.0	68.62
PdI: 0.246	Peak 2:	0.000	0.0	0.000
Intercept: 0.904	Peak 3:	0.000	0.0	0.000

Result quality Good

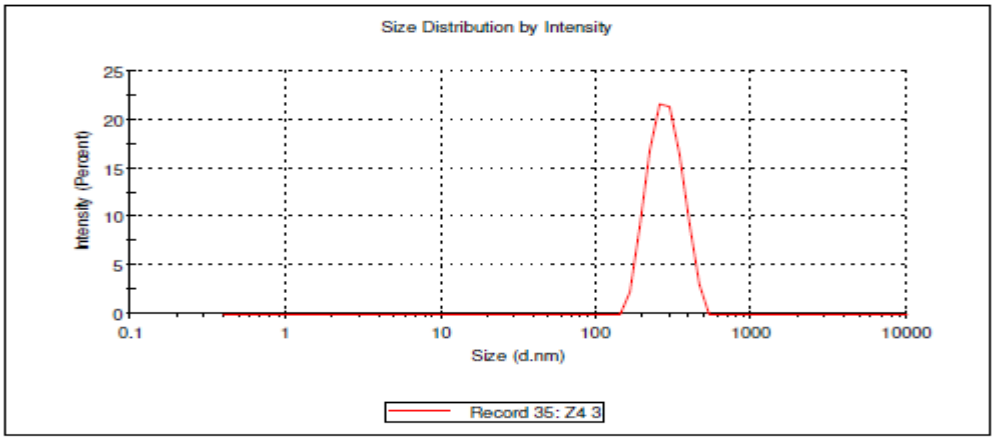

Figure B.1: S200 Zetasizing results

Results

		Size (d.nm...	% Intensity:	St Dev (d.n...
Z-Average (d.nm): 343.7	Peak 1:	323.0	96.2	84.35
PdI: 0.259	Peak 2:	5209	3.8	468.7
Intercept: 0.930	Peak 3:	0.000	0.0	0.000

Result quality Good

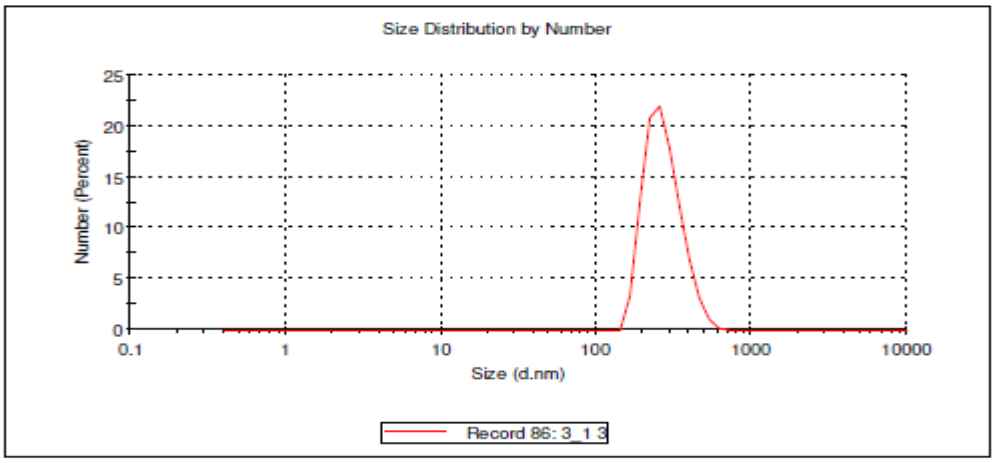

Figure B.2: S300 silica nanosphere Zetasizing results

			Size (d.nm...	% Intensity:	St Dev (d.n...
Z-Average (d.nm):	396.3	Peak 1:	419.8	100.0	102.4
PdI:	0.052	Peak 2:	0.000	0.0	0.000
Intercept:	0.948	Peak 3:	0.000	0.0	0.000
Result quality	Good				

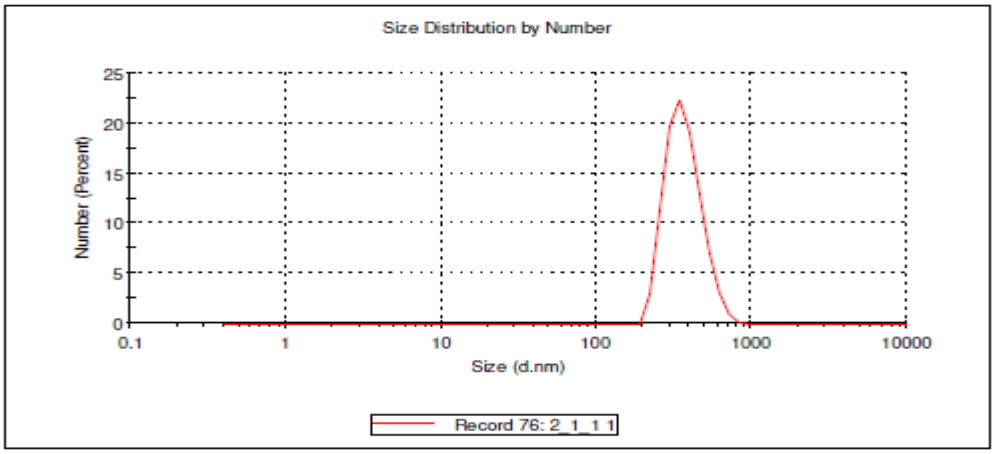

Figure B.3: S400 silica nanosphere Zetasizing results

B.2. SEM PSD

The PSD of the silica nanospheres was also calculated directly from the SEM images using MATLAB. Three or four images for each sample was analysed where more than 80 particles were correctly selected. The MATLAB algorithm displayed the detected spheres over the original micrograph so that each image could be visually inspected for incorrect detection and other errors before the PSD data was extracted. The percentage of spheres that were correctly detected on an image largely depended on the image quality and spatial distribution of the particles (SEM sample preparation). For example, a SEM image with few spheres that do not overlap will result in 100% correct sphere detection where a SEM image with many spheres overlapping each other will result in a much lower percentage. The MATLAB code is presented below with the particle selections in Figure B.4- Figure B.6

```
close all% closes all open figures and windows
I200=imread('S200.tif'); % reads the tiff file and saves the image
I200_1=im2bw(I200,0.3);% converts the greyscale image to binary
black and white, thresholded
[c,r]=imfindcircles(I200_1,[30 45],'ObjectPolarity' ,'bright'
,'Sensitivity' ,0.9); % detects bright circles in the image
figure; % opens a figure window
imshow(I200); % displays original figure
viscircles(c,r); % plots selected circles on original figure
```

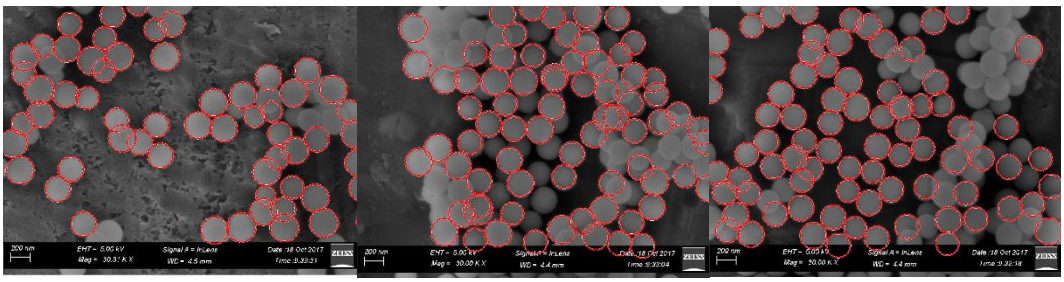

Figure B.4: S200 MATLAB PSD particle selection

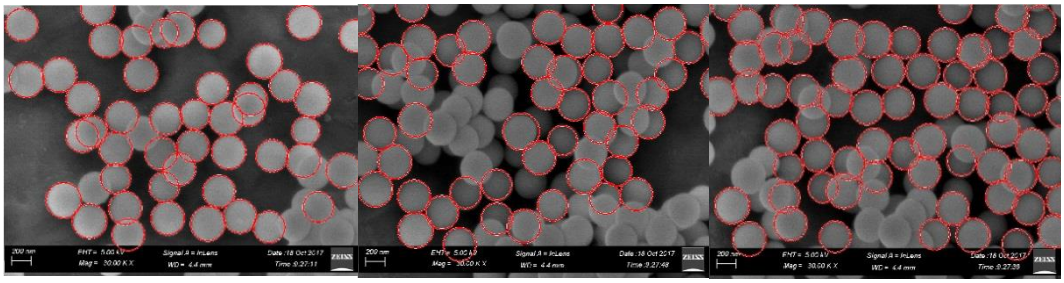

Figure B.5: S300 MATLAB particle size selection

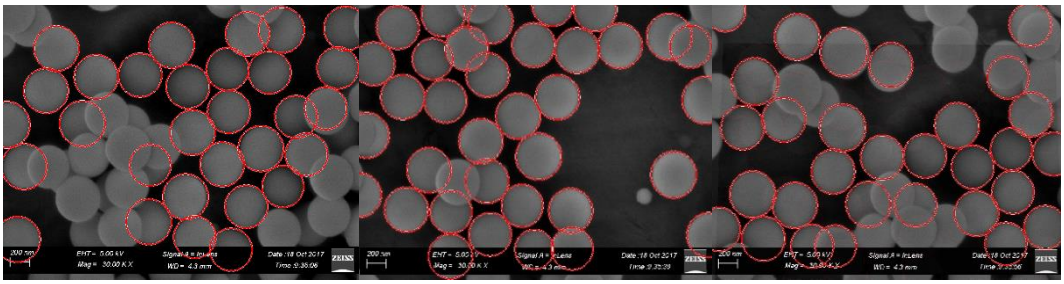

Figure B.6: S400 MATLAB particle size selection

Appendix C: TGA, EDS and Elemental Analysis

C.1. TGA Results

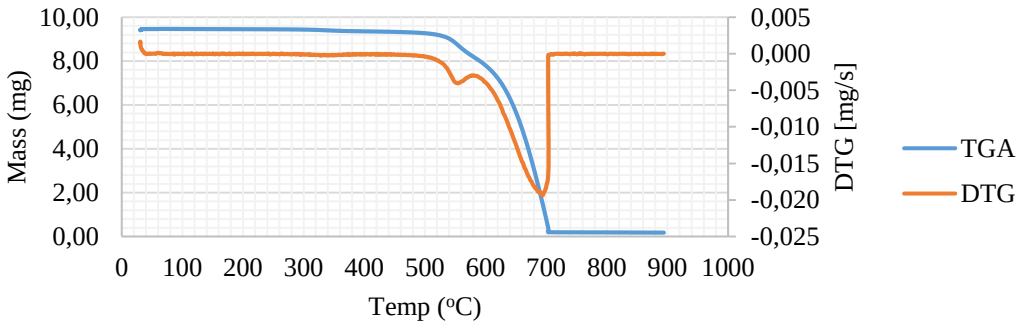

Figure C.1: TGA and DTG results of CVD02 (partial spheres)

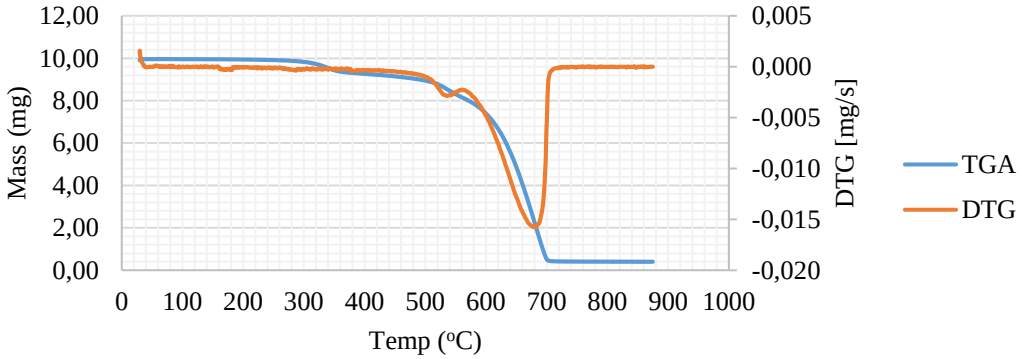

Figure C.2: TGA and DTG results of CVD04 (sphere flakes)

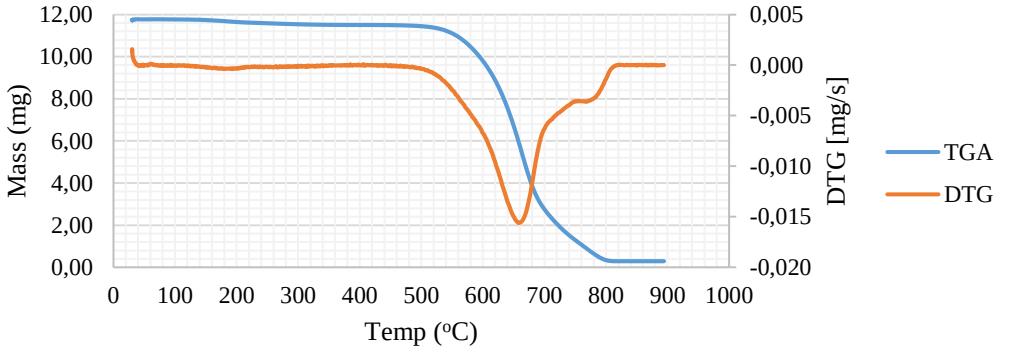

Figure C.3: TGA and DTG results of SCS01 (solid carbon)

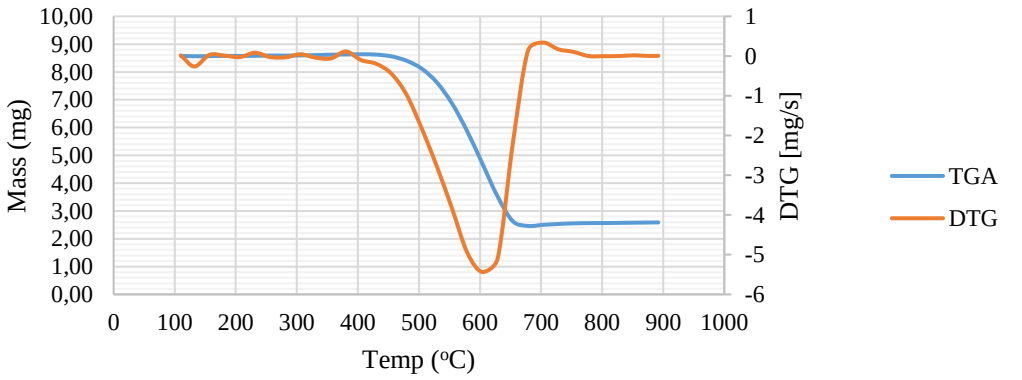

Figure C.4: TGA and DTG results of RF01 (whole, non-porous HCNSs)

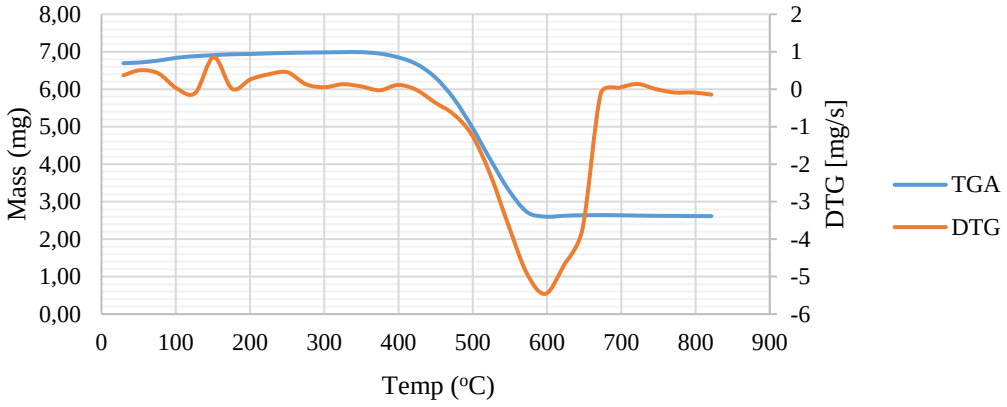

Figure C.5: TGA and DTG results for RF02 (porous HCNSs with impurities)

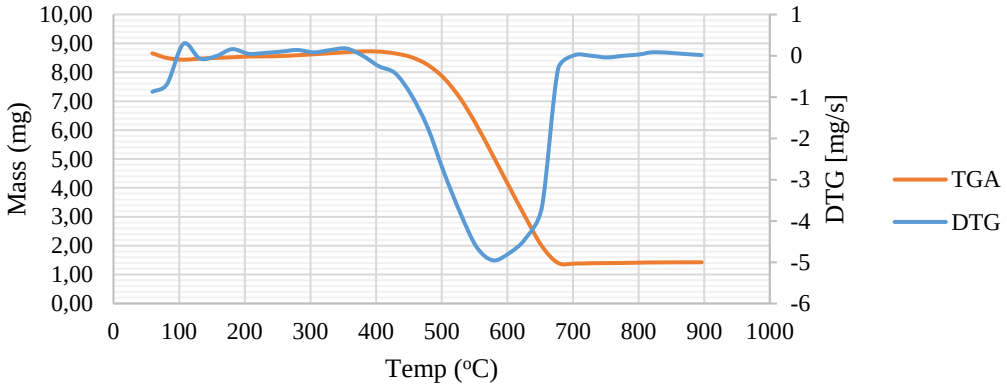

Figure C.6: TGA and DTG results of DRF01 (nitrogen doped RF01 HCNSs)

C.2. EDS and Elemental Analysis on Nitrogen doped DRF01

EDS as well elemental analysis was performed on the nitrogen doped RF HCNS sample, DRF01 to confirm the nitrogen-doping and determine the mass % nitrogen in the sample. The EDS and elemental analysis results are presented in Figure C.7 and Table C.1 respectively.

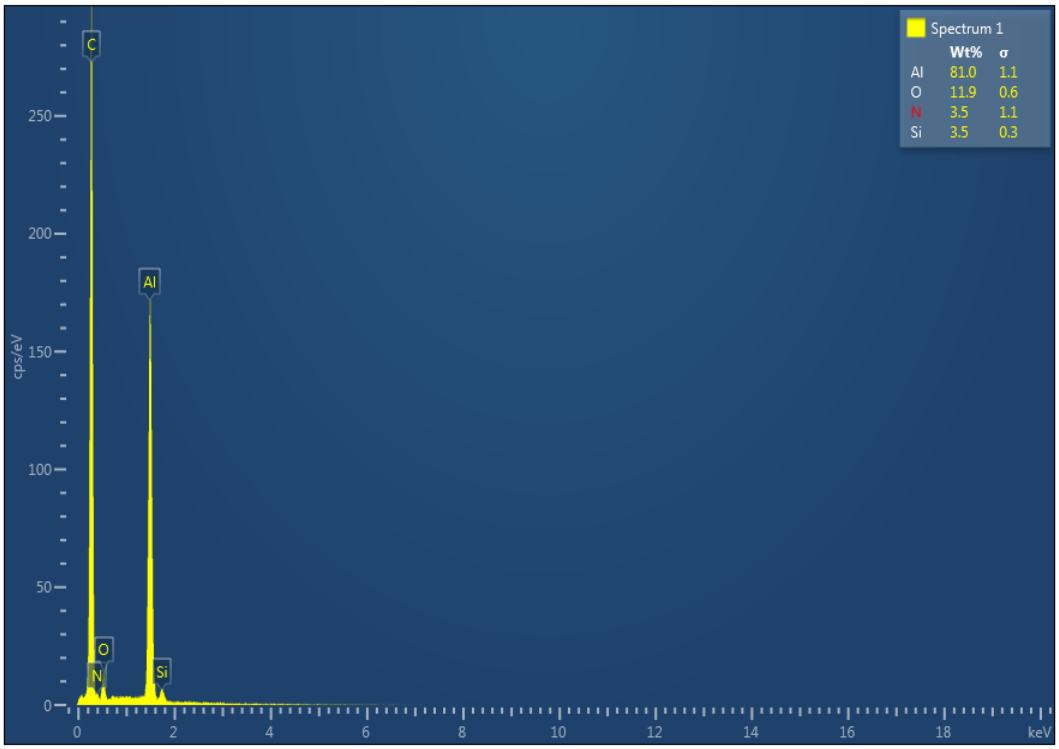

Figure C.7: EDS results of nitrogen doped DRF01 HCNSs

Table C.1: Elemental analysis of DRF01

Name	Weight [mg]	N [%]	C [%]	H [%]	S [%]
DRF01	1.6	3.1	81.9	1.7	0.1

Appendix D: Powder Compaction Results

Additional Heckel fitting results are presented in this section to support the summarised results in Section 5.5.

D.1. Silica Nanospheres

Twelve tests were completed for the silica compaction. The deformation stage Heckel linear trendline fitting equations and calculated Heckel parameters are summarised in Table D.1.

Table D.1: Heckel fitting parameter summary and yield pressure calculation for silica nanospheres

Run	Linear trendline	$\ln\left(\frac{1}{\epsilon_0}\right)$	K	$P_y = 1/K$ [MPa]
S200_1	Y = 0.5595 + 1.75E-6 (X)	0.5595	1.75E-6	584.80
S200_2	Y = 0.5566 + 1.71E-6 (X)	0.5566	1.71E-6	571.43
S200_3	Y = 0.5796 + 1.76E-6 (X)	0.5796	1.76E-6	568.18
S300_4	Y = 0.5564 + 1.76E-6 (X)	0.5564	1.76E-6	568.18
S300_1	Y = 0.6727 + 2.08E-6 (X)	0.6727	2.08E-6	480.77
S300_2	Y = 0.6443 + 2.08E-6 (X)	0.6443	2.08E-6	480.77
S300_3	Y = 0.6443 + 2.15E-6 (X)	0.6443	2.15E-6	465.12
S300_4	Y = 0.6575 + 2.04E-6 (X)	0.6575	2.04E-6	490.20
S400_1	Y = 0.8060 + 3.07E-6 (X)	0.806	3.07E-6	325.73
S400_2	Y = 0.7913 + 2.98E-6 (X)	0.7913	2.98E-6	335.57
S400_3	Y = 0.7993 + 3.05E-6 (X)	0.7993	3.05E-6	327.87
S400_4	Y = 0.8177 + 3.02E-6 (X)	0.8177	3.02E-6	331.13

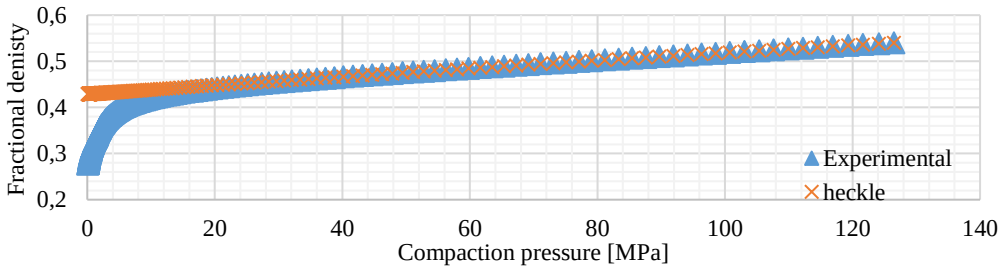

Figure D.1: Silica S200_1 compaction curve with superimposed Heckel equation

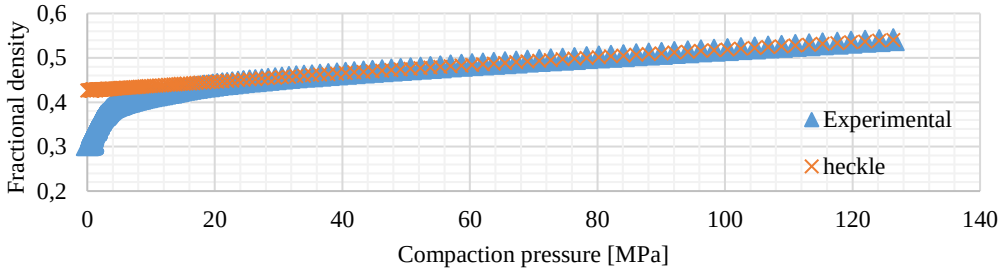

Figure D.2: Silica S200_2 compaction curve with superimposed Heckel equation

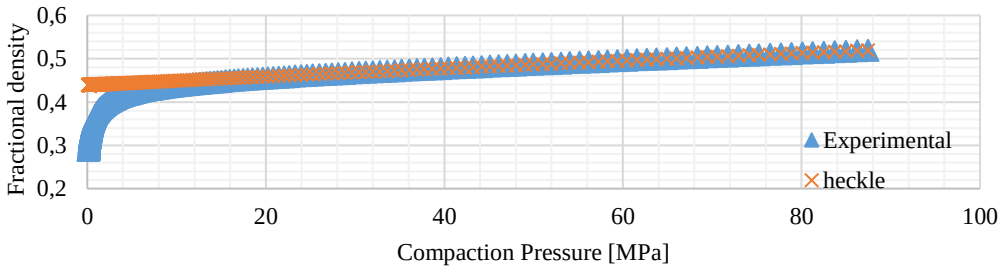

Figure D.3: Silica S200_3 compaction curve with superimposed Heckel equation

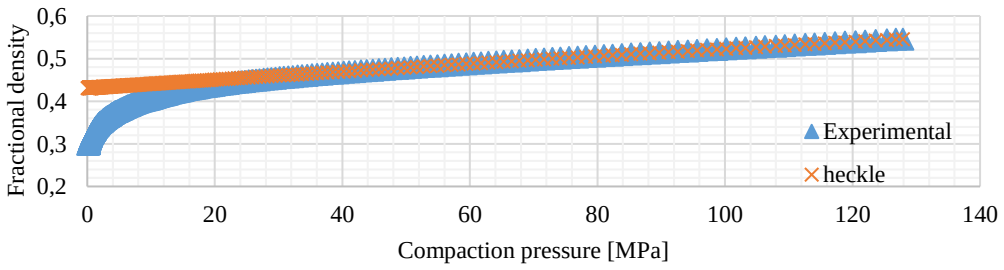

Figure D.4: Silica S200_4 compaction curve with superimposed Heckel equation

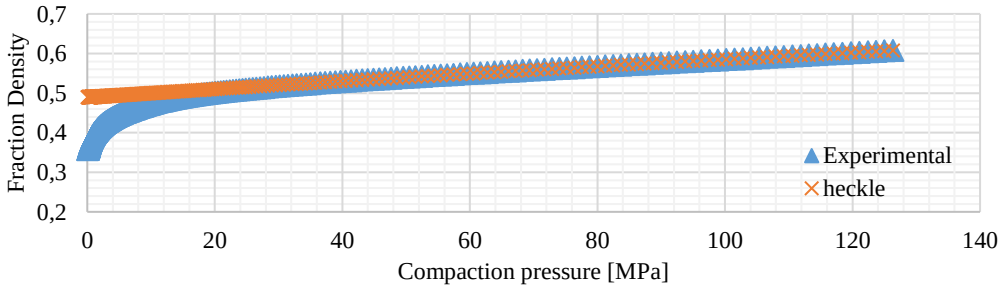

Figure D.5: Silica S300_1 compaction curve with superimposed Heckel equation

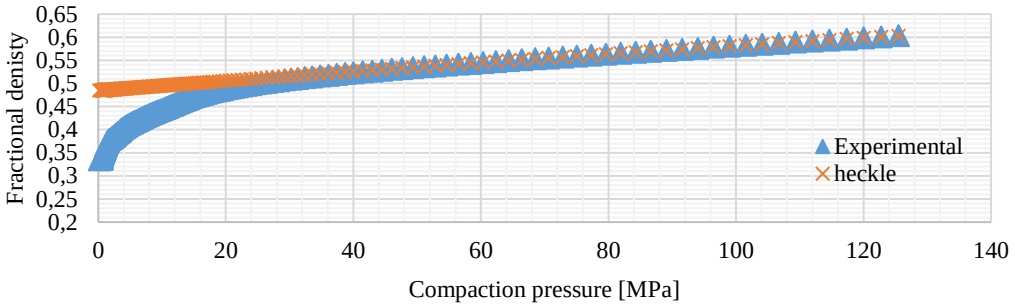

Figure D.6: Silica S300_2 compaction curve with superimposed Heckel equation

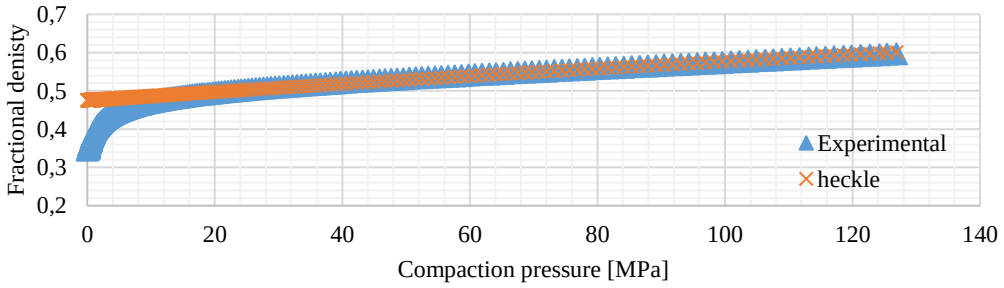

Figure D.7: Silica S300_3 compaction curve with superimposed Heckel equation

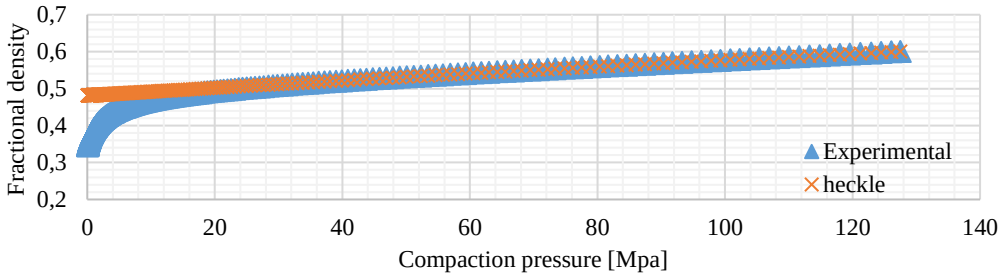

Figure D.8: Silica S300_4 compaction curve with superimposed Heckel equation

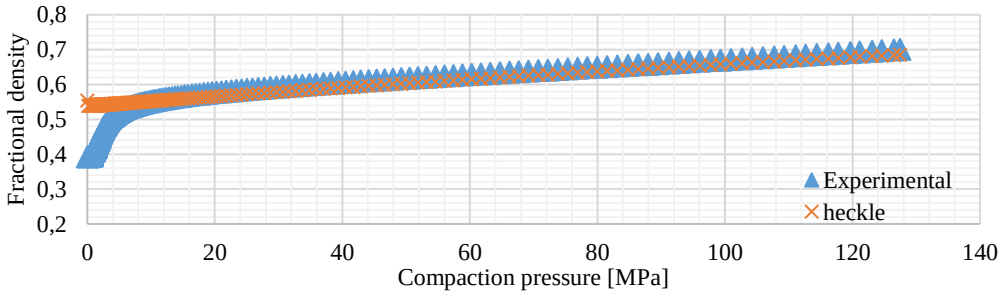

Figure D.9: Silica S400_1 compaction curve with superimposed Heckel equation

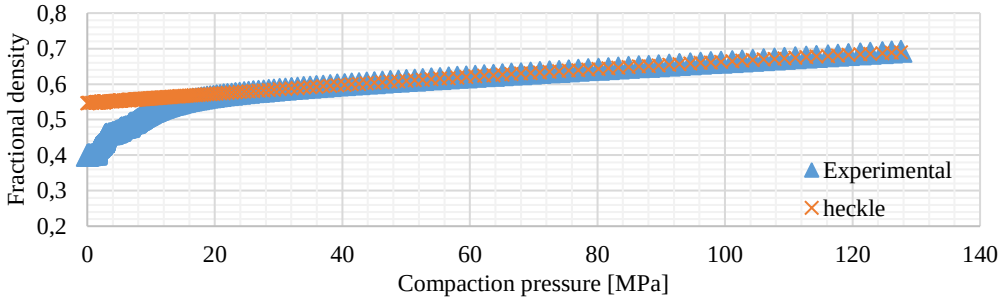

Figure D.10: Silica S400_2 compaction curve with superimposed Heckel equation

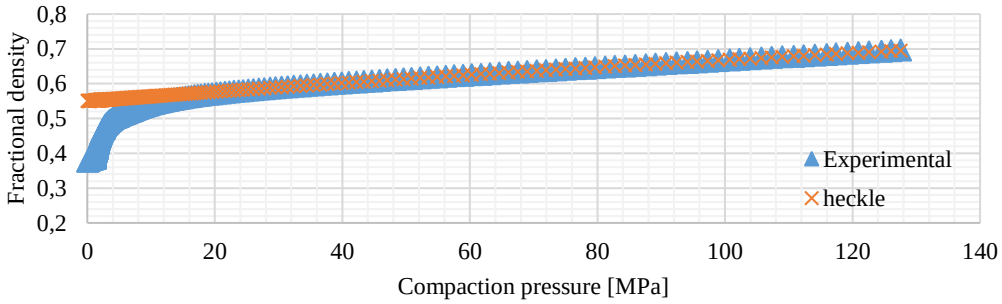

Figure D.11: Silica S400_3 compaction curve with superimposed Heckel equation

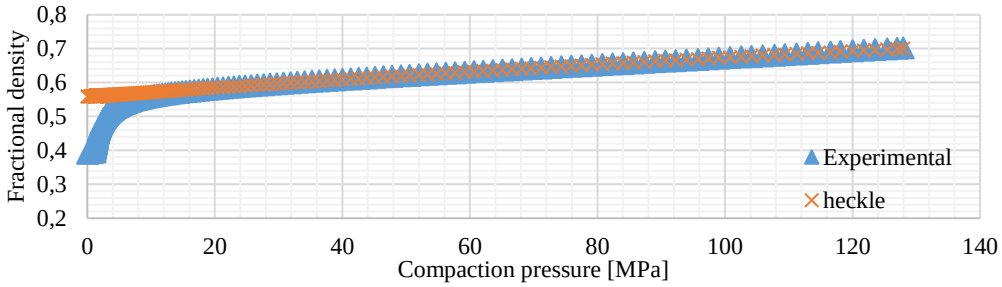

Figure D.12: Silica S400_4 compaction curve with superimposed Heckel equation

D.2. CVD Solid and HCNSs

Nine tests were completed for the CVD solid and HCNS compaction. The deformation stage Heckel linear trendline fitting equations and calculated Heckel parameters are summarised in Table D.2.

Table D.2: Heckel fitting parameter summary and yield pressure calculation for CVD solid and HCNSs

Run	Linear trendline	$\ln\left(\frac{1}{\epsilon_0}\right)$	K	$P_y = 1/K$ [MPa]
CVD02_1	Y = 0.2291 + 5.99E-6 (X)	0.2291	5.99E-6	166.94
CVD02_2	Y = 0.2720 + 5.77E-6 (X)	0.2720	5.77E-6	173.31
CVD02_3	Y = 0.2150 + 5.92E-6 (X)	0.2150	5.92E-6	168.92
CVD03_1	Y = 0.3019 + 9.02E-6 (X)	0.3019	9.02E-6	108.70
CVD03_2	Y = 0.1977 + 8.10E-6 (X)	0.1977	8.10E-6	123.46
CVD03_3	Y = 0.2900 + 8.26E-6 (X)	0.2900	8.26E-6	121.07
SCS01_1	Y = 0.3539 + 7.36E-6 (X)	0.3539	7.36E-6	135.87
SCS01_2	Y = 0.3687 + 9.94E-6 (X)	0.3687	9.94E-6	100.60
SCS01_3	Y = 0.2953 + 5.96E-6 (X)	0.2953	5.96E-6	167.79

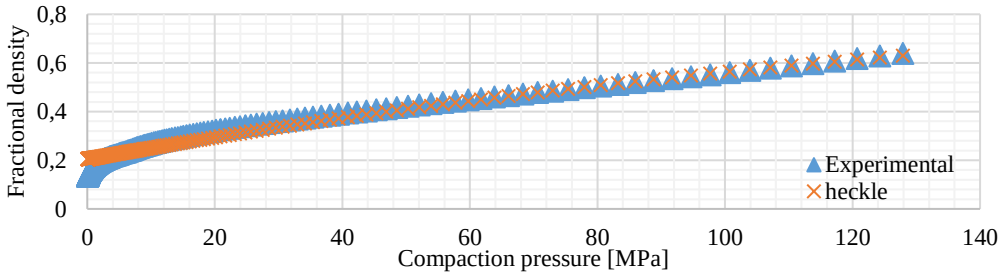

Figure D.13: CVD02_1 (partial spheres) compaction curve with superimposed Heckel equation

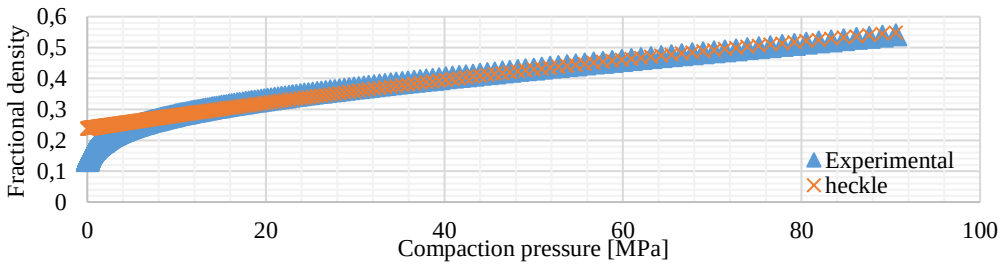

Figure D.14: CVD02_2 (partial spheres) compaction curve with superimposed Heckel equation

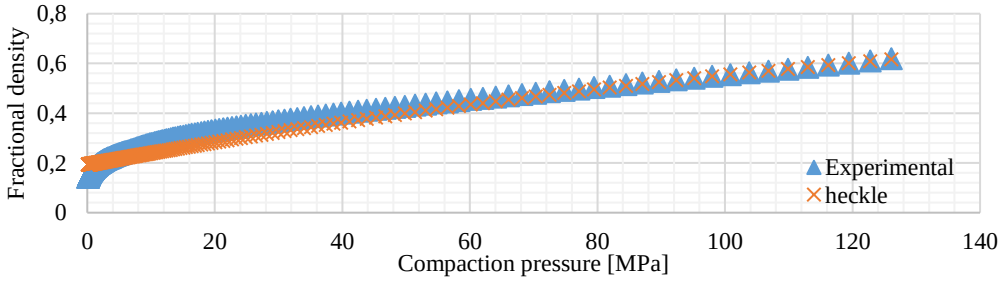

Figure D.15: CVD02_3 (partial spheres) compaction curve with superimposed Heckel equation

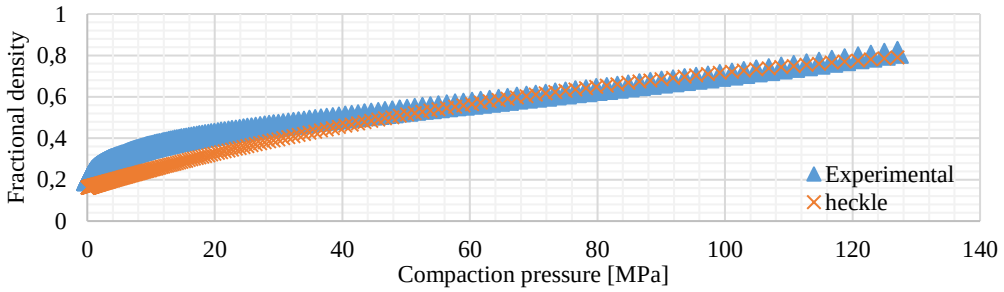

Figure D.16: CVD03_1 (sphere flakes) compaction curve with superimposed Heckel equation

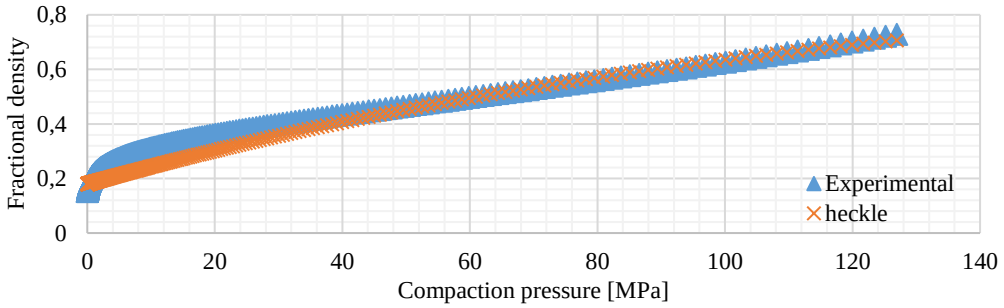

Figure D.17: CVD03_2 (sphere flakes) compaction curve with superimposed Heckel equation

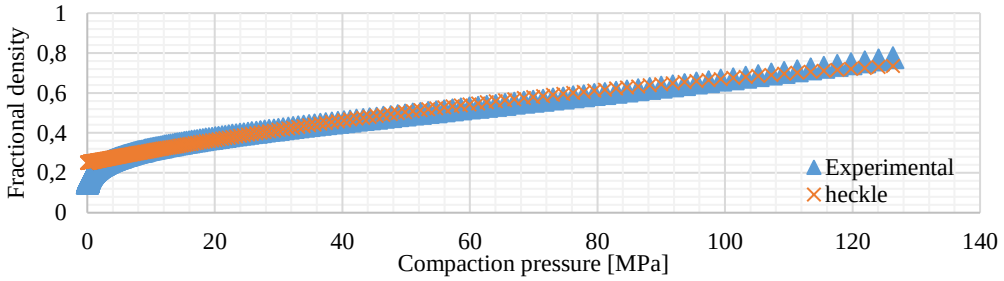

Figure D.18: CVD03_3 (sphere flakes) compaction curve with superimposed Heckel equation

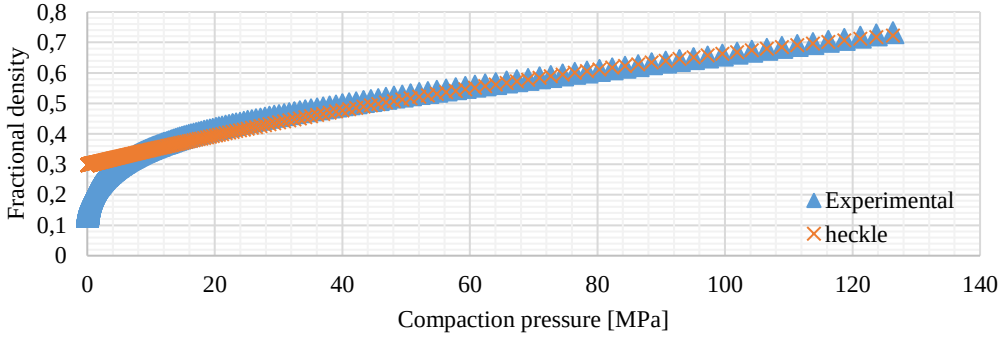

Figure D.19: SCS01_1 (solid carbon spheres) compaction curve with superimposed Heckel equation

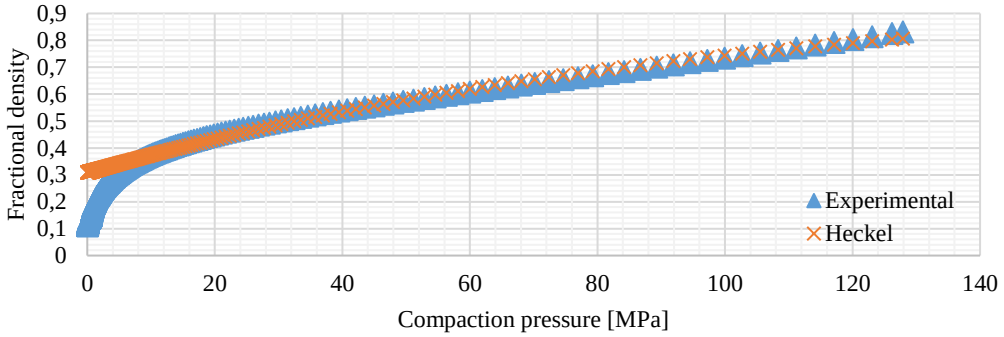

Figure D.20: SCS01_2 (solid carbon spheres) compaction curve with superimposed Heckel equation

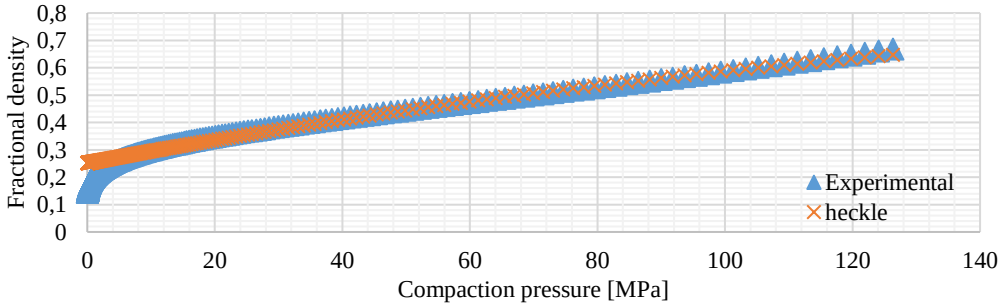

Figure D.21: SCS01_3 (solid carbon spheres) compaction curve with superimposed Heckel equation

D.3. RF HCNSs

Severn tests were completed for the RF HCNS compaction. The deformation stage Heckel linear trendline fitting equations and calculated Heckel parameters are summarised in Table D.3.

Table D.3: Heckel fitting parameter summary and yield pressure calculation for RF HCNSs

Run	Linear trendline	$\ln\left(\frac{1}{\epsilon_0}\right)$	K	$P_y = 1/K$ [MPa]
RF01_1	Y = 0.0279 + 3.75E-6 (X)	0.0279	3.75E-6	266.67
RF01_2	Y = 0.0239 + 3.83E-6 (X)	0.0239	3.83E-6	261.10
RF02_1	Y = 0.0720 + 1.06E-6 (X)	0.0720	1.06E-6	94.34
RF02_2	Y = 0.0781 + 1.1E-05 (X)	0.0781	1.1E-05	90.17
DRF01_1	Y = 0.1021 + 4.04E-6 (X)	0.1021	4.04E-6	242.52
DRF01_2	Y = 0.1009 + 3.95E-6 (X)	0.1009	3.95E-6	253.16
CRF01	Y = 0.1155 + 7.07E-6 (X)	0.1155	7.07E-6	141.44

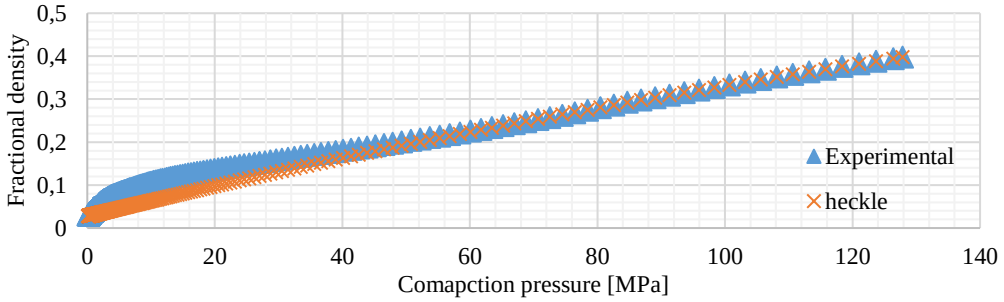

Figure D.22: RF01_1 (non-porous, whole) compaction curve with superimposed Heckel equation

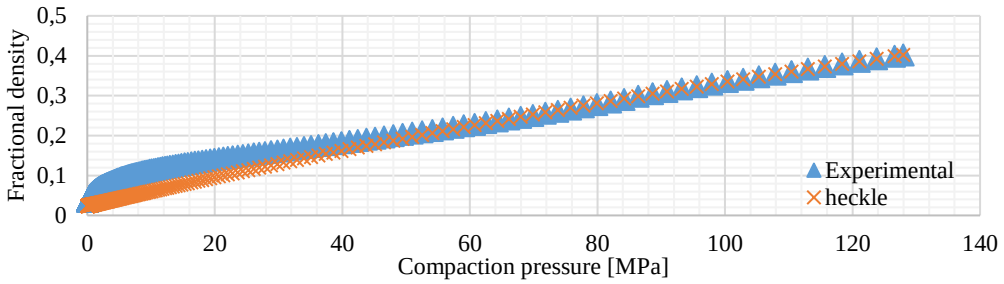

Figure D.23: RF01_2 (non-porous, whole) compaction curve with superimposed Heckel equation

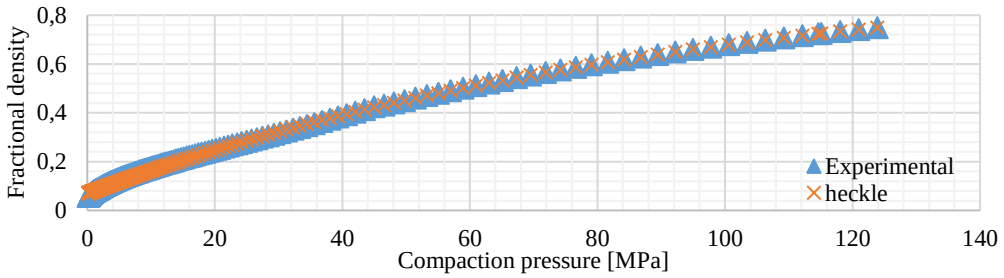

Figure D.24: RF02_1 (porous, impurities) compaction curve with superimposed Heckel equation

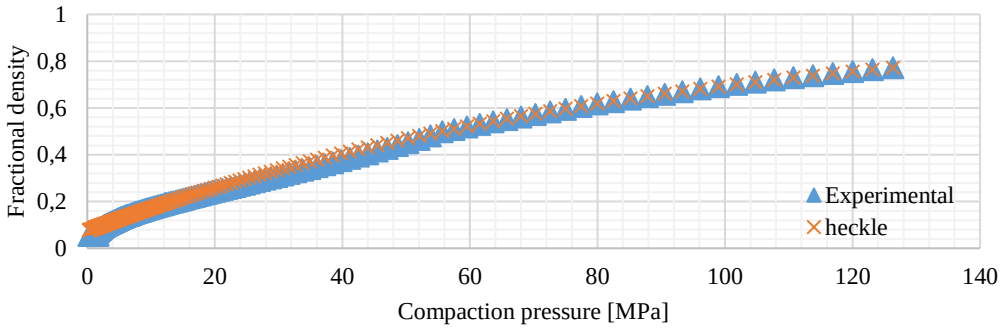

Figure D.25: RF02_2 (porous, impurities) compaction curve with superimposed Heckel equation

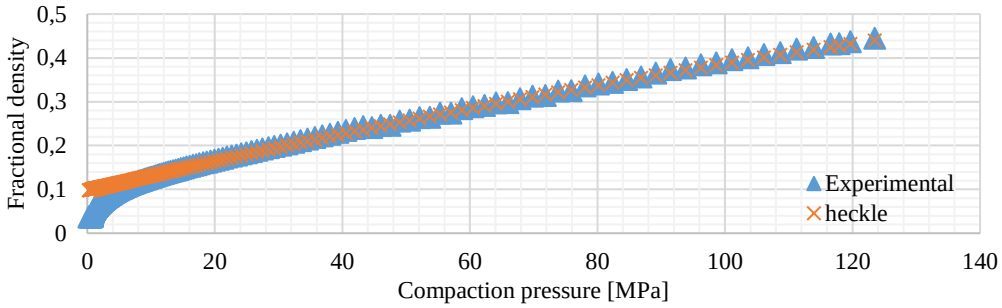

Figure D.26: DRF01_1 (N_2 doped RF01) compaction curve with superimposed Heckel equation

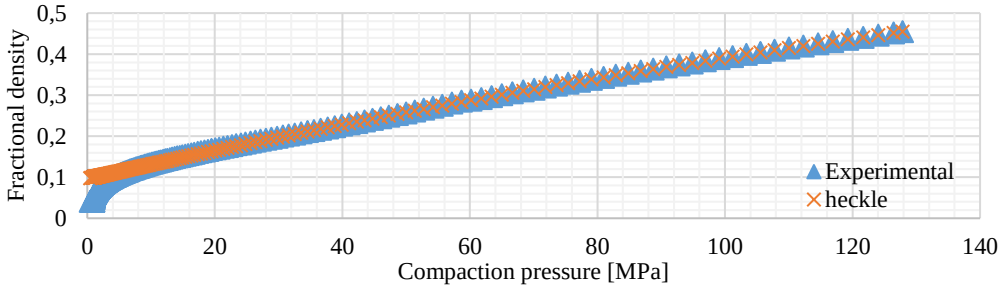

Figure D.27: DRF01_2 (N_2 doped RF01) compaction curve with superimposed Heckel equation

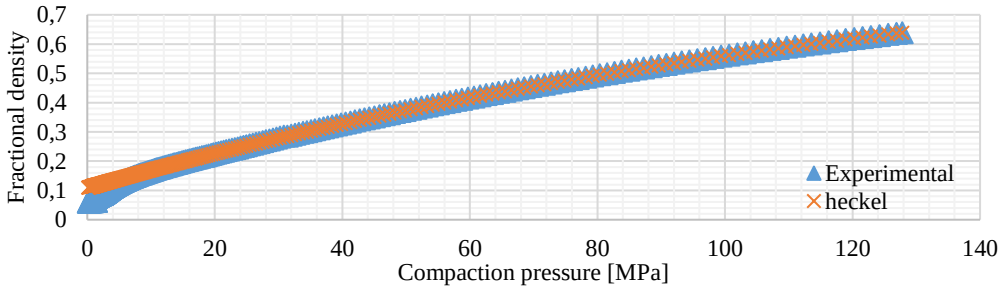

Figure D.28: CRF01 (Crushed RF01) compaction curve with superimposed Heckel equation

Appendix E: Additional SEM and TEM images

E.1. Silica Nanospheres

SEM images were taken before and after 200 MPa compaction to see if any fracturing or plastic deformation occurred. These images are presented in Figure E.1 - Figure E.3.

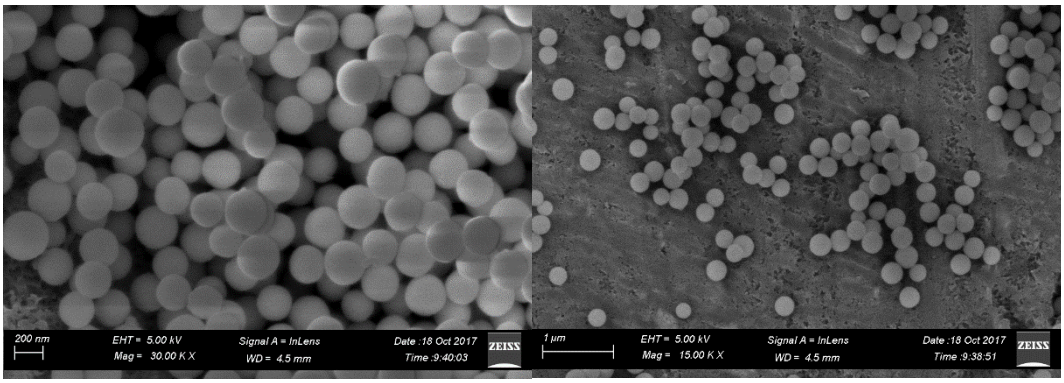

Figure E.1: SEM images of S200 before (left) and after (right) 300 MPa compaction

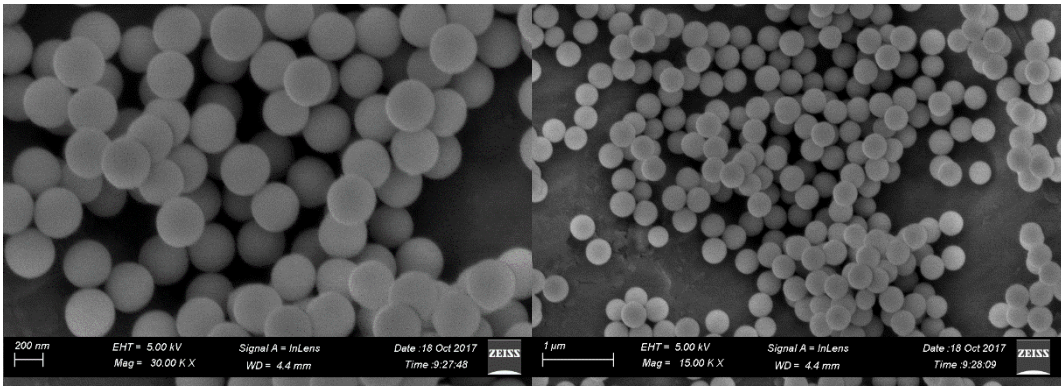

Figure E.2: SEM images of S300 before (left) and after (right) 300 MPa compaction

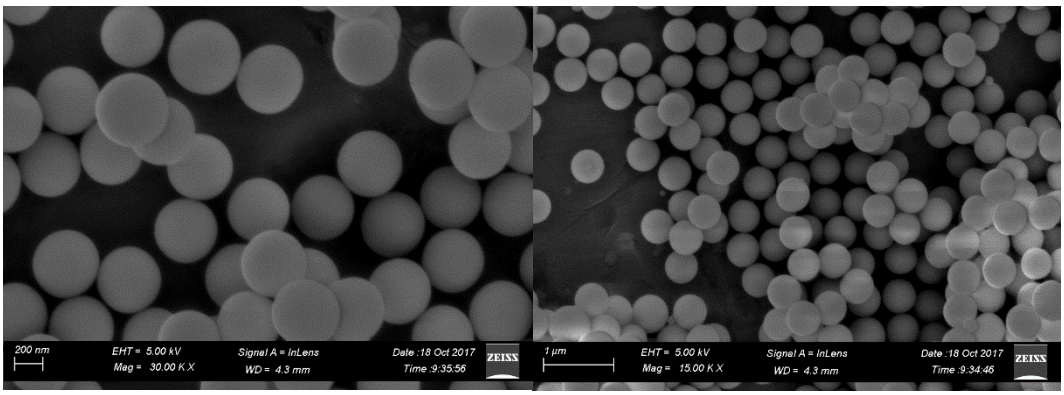

Figure E.3: SEM images of S400 before (left) and after (right) 300 MPa compaction

E.2. RF HCNSs

E.2.1. RF HCNS PSD

TEM images were used to determine the RF HCNSs PSD and shell thickness. This data was calculated directly from the TEM images using MATLAB. Three images for each sample was analysed and more than 50 particles were selected. The MATLAB code and particle selections are presented in this subsection.

```
close all% closes all open figures and windows
I=imread('RF01_1.tif'); % reads the tif file and saves the image
IR = imresize(I, 0.3);
IR_1=im2bw(IR,0.3);% converts the greyscale image to binary black
and white, thresholded
[c,r]=imfindcircles(IR_1,[35 60],'ObjectPolarity' ,'dark
','Sensitivity' ,0.93); % detects dark circles in the image
figure; % opens a figure window
imshow(I); % displays original figure
viscircles(c,r); % plots selected circles on original figure
```

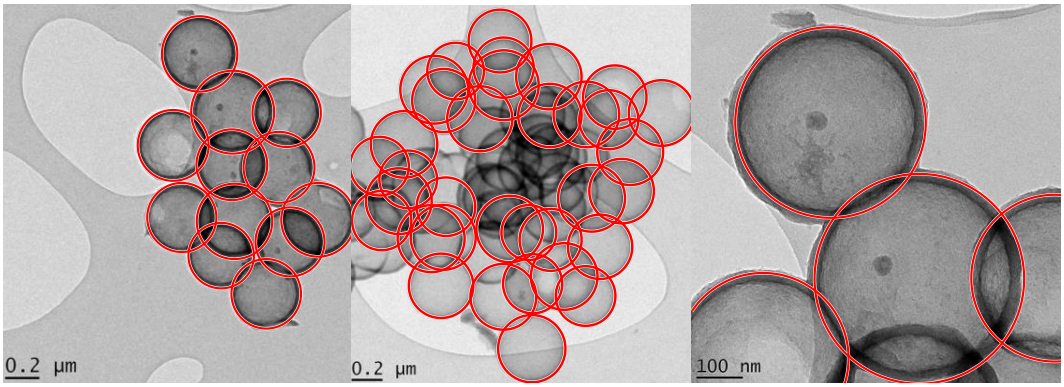

Figure E.4: PSD selections of the TEM images of RF01 HCNSs

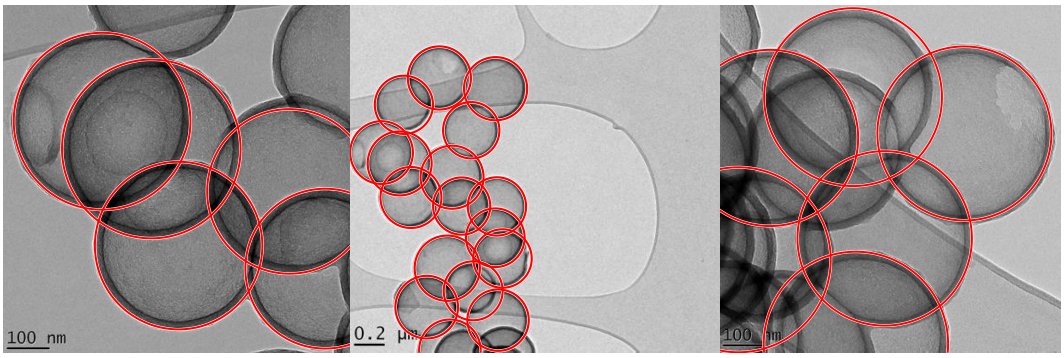

Figure E.5: PSD selections of the TEM images of DRF01 HCNSs

The PSD and shell thickness calculations for the RF02 (porous shells and impurities) were done by hand because of limited TEM images of the sample, presented in Figure E.6.

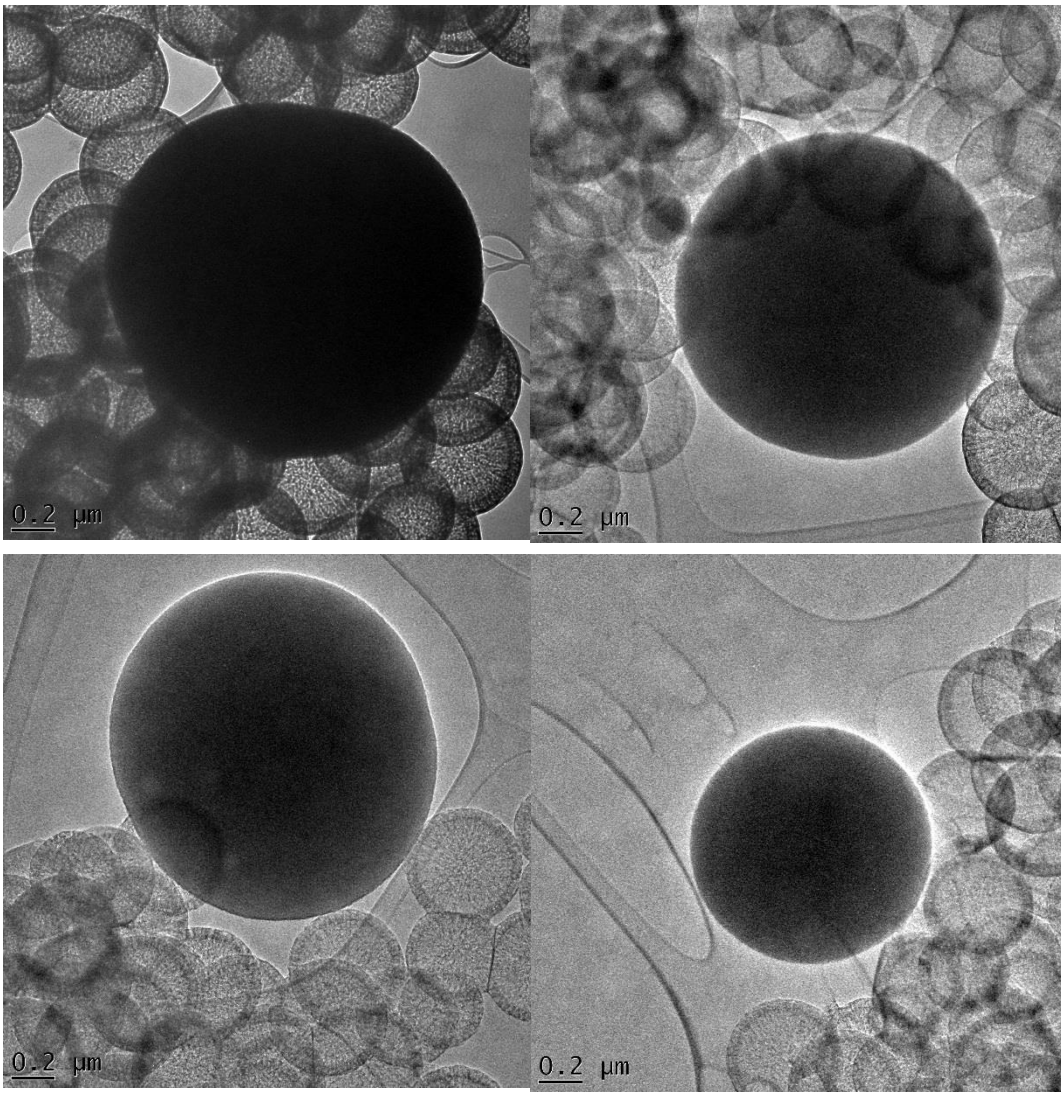

Figure E.6: TEM images of RF01 (porous shells and impurities)

E.2.2. RF HCNSs at Various Compaction Pressures

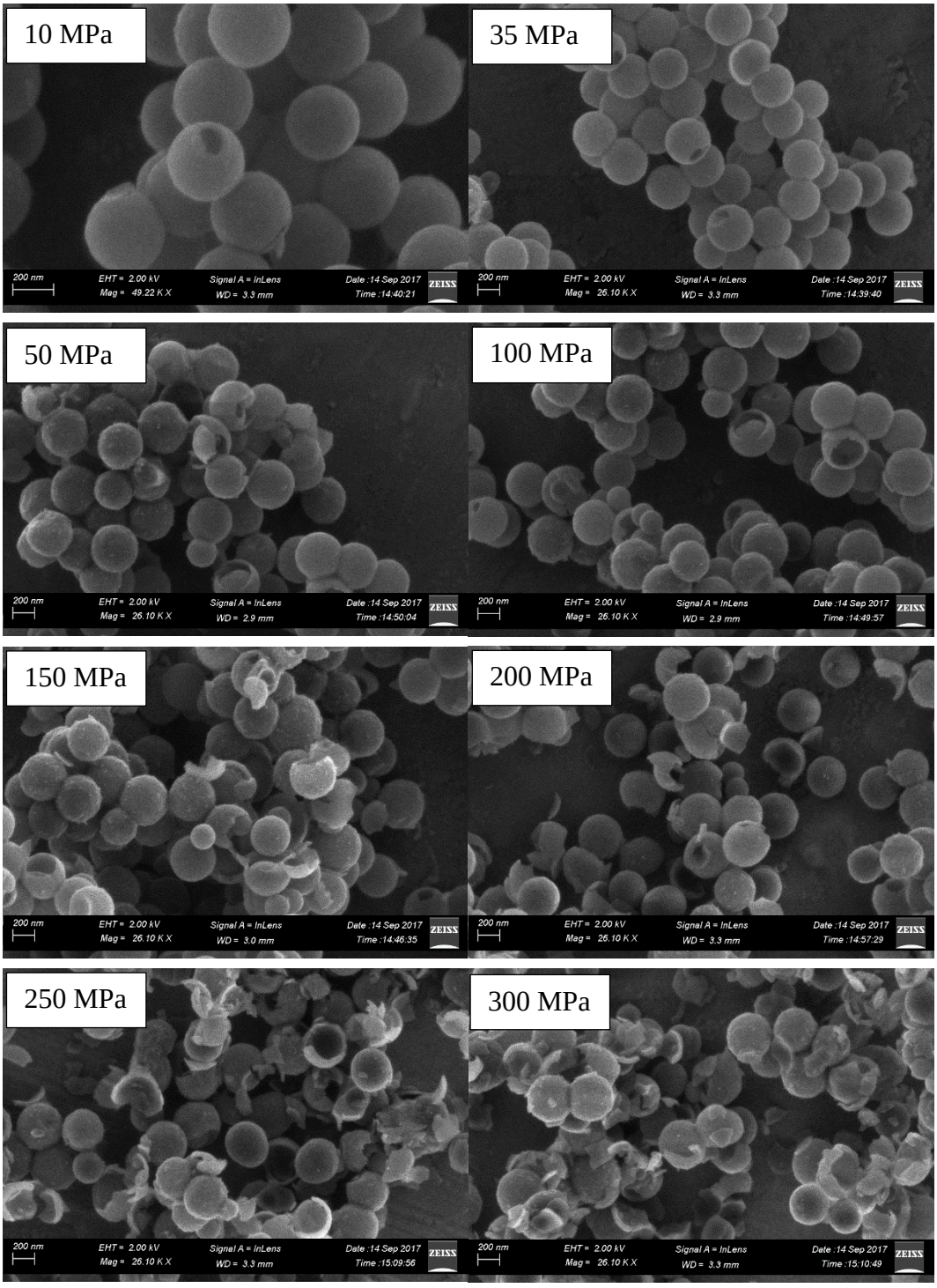

Figure E.7: SEM images of RF01 HCNSs at different compaction pressures